N 73-28591

NASA CONTRACTOR REPORT

NASA CR-2254

NASA CR-2254

CASE FILE
COPY

DEVELOPMENT OF A CLOSED PORE INSULATION MATERIAL

*by Albert Tobin, Carl Feldman, Michael Russak,
and Joseph Reichman*

Prepared by
GRUMMAN AEROSPACE CORPORATION
Bethpage, N.Y. 11714
for Langley Research Center

NATIONAL AERONAUTICS AND SPACE ADMINISTRATION • WASHINGTON, D. C. • JULY 1973

1. Report No.
NASA CR-2254

2. Government Accession No.

3. Recipient's Catalog No.

4. Title and Subtitle
DEVELOPMENT OF A CLOSED PORE INSULATION MATERIAL

5. Report Date
July 1973

6. Performing Organization Code

7. Author(s)
Albert Tobin, Carl Feldman, Michael Russak, and Joseph Reichman

8. Performing Organization Report No.

9. Performing Organization Name and Address
Grumman Aerospace Corporation
Bethpage, New York 11714

10. Work Unit No.
501-31-50-01

11. Contract or Grant No.
NAS1-10713

12. Sponsoring Agency Name and Address
National Aeronautics and Space Administration
Washington, D.C. 20546

13. Type of Report and Period Covered
Contractor Report

14. Sponsoring Agency Code

15. Supplementary Notes

16. Abstract

A closed pore ceramic foam insulation material (CPI) has been developed that offers possibilities for use as a reusable external heat shield for the NASA Manned Space Shuttle. The outstanding characteristics of CPI are: 1) negligible water absorption at densities of 450 kg/m^3 due to a noninterconnecting network of cells; 2) high emittance (ϵ_n = 0.8 built into the basic foam formulation) at room and elevated temperatures; 3) ability to survive at least 10 simulated reentry cycles to 1500 K using radiant heat lamps to simulate the reentry heat fluxes; 4) ability to survive, with no change in properties or appearance, at least 10 simulated plasma arc jet cycles to 1500 K (with the exception of some stress cracks induced either by the unduly severe nature of the initial arc "splash" heating pulse or by improper mechanical holding of the specimen in the test fixutre); 5) strength (flexure) of 55 x 10^5 N/m^2; and 6) a low thermal conductivity (0.18 - 0.40 W/m K) throughout the temperature range of interest for the Space Shuttle.

17. Key Words (Suggested by Author(s))
Closed Pore Insulation
Water Absorption
Heat Shield
Emittance
Reentry Cycles

18. Distribution Statement
Unclassified - Unlimited

19. Security Classif. (of this report)
Unclassified

20. Security Classif. (of this page)
Unclassified

21. No. of Pages
179

22. Price*
$3.00

*For sale by the National Technical Information Service, Springfield, Virginia 22151

DEVELOPMENT OF A CLOSED PORE INSULATION MATERIAL

By Albert Tobin, Carl Feldman
Michael Russak, and Joseph Reichman

Grumman Aerospace Corporation

SUMMARY

A closed pore ceramic foam insulation material (CPI) has been developed that offers possibilities for use as a reusable external heat shield for the NASA Manned Space Shuttle. The outstanding characteristics of CPI are: 1) negligible water absorption at densities of 450 kg/m^3 due to a noninterconnecting network of cells; 2) high emittance ($\epsilon_n = 0.8$ built into the basic foam formulation) at room and elevated temperatures; 3) ability to survive at least 10 simulated re-entry cycles to 1500 K using radiant heat lamps to simulate the re-entry heat fluxes; 4) ability to survive, with no change in properties or appearance, at least 10 simulated plasma arc jet cycles to 1500 K (with the exception of some stress cracks induced either by the unduly severe nature of the initial arc "splash" heating pulse or by improper mechanical holding of the specimen in the test fixture); 5) strength (flexure) of 55×10^5 N/m^2; and 6) a low thermal conductivity (0.18-0.40 W/m K) throughout the temperature range of interest for the Space Shuttle.

In addition, the low cost raw material (fly ash) from which the heat shield is made, and the simplicity of the fabrication procedure, make it a potentially low cost, high performance material. Major advantages of CPI are its closed pore (waterproof) structure and its inherently high emissivity, which eliminates the need for a very thin, brittle, protective water resistant coating. The high strength and modulus and ease of machinability of CPI have permitted the successful construction of composite heat shields that can be mechanically fastened to the primary structure of the vehicle.

Reproducibility of the thermophysical and mechanical properties of scaled-up CPI tiles (20 cm x 20 cm x 2 cm) has been successfully demonstrated in compositions containing up to 12 wt. % cobalt oxide as the high emittance additive. Some insight into the mechanism of formation of the foam has been generated.

Material improvements yet to be achieved include: 1) further reduction of foam density without sacrifice of other desirable properties; and 2) improved thermal shock resistance of the foam. Both problems are being attacked through changes in composition, and novel design and construction techniques. Regarding the latter, composite heat shield designs reduce weight and eliminate thermal shock problems in re-entry cycling, by reducing the required thickness of CPI.

TABLE OF CONTENTS

LIST OF SYMBOLS

a	moment arm, heating rate, absorption coefficient
b	width
c_p	heat capacity
E	elastic modulus
F_b	flexural strength
h_{hf}	heat flux enthalpy
I	current
k	thermal conductivity
K	absolute temperature in Kelvin
l	length
m	mass
n	index of refraction
p	applied load
p_s	stagnation pressure
q	heat flux
R	radius of cylinder, radius of nose, diffuse internal reflectance
s	scattering coefficient
t	thickness
T	length, correction factor, absolute temperature
u_H	upper half height frequency
u_L	lower half height frequency
u_R	resonance frequency

V_s	radiometer output signal at temperature T_s
V_b	radiometer out signal from blackbody at temperature T_b
x	direction normal to load axis
y	direction along load axis
β	high temperature stable phase of spodumene
δ	damping capacity
Δ	increment
ϵ_N	total normal emittance
ϵ	strain
σ	tensile strength, Stephan-Boltzmann radiation constant
ρ	density
μ	Poisson's ratio

Special Note on Units

The units employes in this report are in accordance with the NASA directive for reporting all units in the International System (SI). In some instances, the U.S. Customary units have been included for the convenience of the reader. The principal measurements and calculations were made with the U.S.C. and CGS units. Some tables (i.e., arc jet tests) have been left in the original U.S. Customary Units where it was believed that changes would result in impairment of communication.

I. INTRODUCTION

One of the primary requirements of the NASA Manned Space Shuttle Program is the development of a fully reusable heat shield to protect the Orbiter prime structure from the high heat loads experienced during the re-entry maneuver. In addition, such an external shield must be able to survive all phases of ground, launch, and space operations to qualify for the Space Shuttle mission. Table 1 gives the basic material properties required for such a thermal protection material. Current efforts in the aerospace industry to build such a nonmetallic insulation have concentrated on the rigidization of refractory ceramic fibers such as silica or mullite, and the application of thin, dense, and brittle ceramic coatings to protect the fibers against rain, vibration, erosion, and handling damage. In addition, the coating must contain a high emittance component to re-radiate the incident heat flux on re-entry. The major difficulties with such an approach appear to be: 1) the incompatibility of the coating with the substrate fibers during thermal cycling due to the mismatch of thermal expansions and elastic moduli; 2) low failure strain in the coating (i.e., 0.00014); 3) water absorption through the coating, leading to unacceptable weight pickup in the fibrous substrate; 4) uniformity of coating application; and 5) coating reliability and NDT inspection. These problems become increasingly magnified when the large areas (1800 m^2) of the Orbiter that must be coated, the manned nature of the mission, and the total number of missions desired of each vehicle are considered.

In addition, the combination of the low strength of the rigidized fibers and the extreme brittleness of the coating makes mechanical attachment schemes to the primary structure very difficult. Attachment schemes require the use of a stiff subpanel and a "soft" adhesive bonding to the carrier panel. This is costly and adds considerable extra weight to the total thermal protection system. Also, inspection of the adhesive bondline after installation becomes a major problem.

In view of the aforementioned problems, it became clear that a new approach to building a heat shield material was needed. Our initial investigations into the possibility that uncoated ceramic fibers could fulfill this requirement through some geometric considerations led to the conclusion that no possible geometric arrangement of fibers could prevent the spreading of water through the open pore network. This is a result of the fact that the contact angle for water on refractory oxides is zero. (The duck feather has an open arrangement of fibers; however, water will not penetrate the feather even though water will "wet" the individual fiber. This is because the contact angle of water on the duck's feather equals 60 degrees, giving the duck an open pore fibrous waterproof raincoat.)

The only way, then, to eliminate water penetration into an insulating ceramic medium is to construct a material with a non-interconnecting network of pores (i.e., a closed cell ceramic foam). After a careful survey of the available literature on ceramic foams and of the various commercial suppliers of ceramic foams (i.e., Pittsburgh Corning, Dow Chemical, Ispen Industries), we concluded that no closed cell material was available that could satisfy the critical needs of the Space Shuttle environment.

The Research program thus had as its initial objective the creation of a refractory high emittance closed cell foam that would survive re-entry cycling to 1500 K.

The authors wish to acknowledge the valuable contributions of Mr. Guenter Baumann of the Grumman Materials and Processes Section for his preparation, heat treatment, and construction of the closed pore insulation heat shields. We are also indebted to Mr. William Corbett for his assistance to Mr. Baumann. Many thanks go to other Grumman personnel: Mr. Richard Truran and Mr. Paul Pittari of the Materials Test Laboratory for their measurements of the mechanical properties of CPI; to Mr. John Androulakis and Mr. William Fischer of the Thermal and Environmental Test Laboratory for their measurements of the thermal properties and performance of the re-entry simulation tests on CPI materials; and Mr. Jack Cusimano of Advanced Development for providing ultrasonic techniques for attaching CPI to honeycomb substrates.

Much appreciation is expressed also to Dr. Malcolm McLaren of the Rutgers University Ceramics Department for providing heat treatment facilities at a critical juncture in this research program.

II. DESCRIPTION OF EXPERIMENTAL APPROACHES

A. Beta-Spodumene Foams

1. Experimental Procedures

Because thermal shock resistance is a more critical problem in a ceramic foam than it is in a fibrous material (due to the monolithic nature of the foam), our initial attempts to produce a closed cell foam centered on beta-spodumene, a low expansion ($\alpha = 8 \times 10^{-7}/$ K) crystalline lithium alumino-silicate that is thermally stable to 1615 K and is commercially available at low cost.

Five approaches to forming a closed cell beta-spodumene foam were tried: 1) additions of organic fugitive porosifiers such as phenolic microballoons, styrofoam spheres, etc., to a beta-spodumene matrix followed by subsequent burnout at elevated temperatures; 2) additions of inorganic hollow microballoons such as FTD-202 (Emerson and Cuming, Inc.) glass microballoons and fly ash cenospheres (Cenoport, Inc.) to a beta-spodumene matrix and subsequent heat treatment; 3) additions of phosphoric acid to each of the above-mentioned mixtures with subsequent firing to elevated temperatures; 4) additions of a foaming agent such as aluminum powder to the phosphoric acid in combination with methods 1) and 2); and 5) additions of a commercial organic foaming agent [i.e., Arquad 16-50 (Armour Industrial Chemical Co.)] to powdered mixtures of cenospheres plus beta-spodumene using a Waring blender following by controlled drying and firing at elevated temperatures.

2. Results and Discussion

Of the five methods employed, only one method (the second) gave promising results. As a result of the burnout and firings, the following problems were encountered: 1) collapse of the foam; 2) extreme friability; 3) excess shrinkages on firing; 4) cracking either on heating or cooling from firing temperatures; liquefaction at the firing temperature (i.e., 1300 K); 6) surface migration of binder phase; 7) uncontrolled variation in pore sizes; and 8) color and texture variation within the same specimen.

The most promising results came from a combination of beta-spodumene/cenospheres in the ratio 30 v% beta-spodumene and 70 v% cenospheres. Small samples that were compression molded and fired to 1620 K formed a uniform closed cell foam at densities of 640 kg/m^3 (40 pcf). Significant problems were encountered in scaling up this composition into 10 cm x 15 cm x 2.5 cm (4" x 6" x 1") plates and further work on this composition was discontinued. It is believed that this composition still offers some promise for scale-up where better control of the furnace gradients and firing cycle is available. This entire investigation is covered in detail in Ref. 1.

B. Eccospheres and Cenospheres

1. Eccospheres

Eccospheres (FTD-202, Emerson and Cuming, Inc.) are hollow silicate glass spheres with bulk densities of 160-240 kg/m^3 (10-15 pcf). The initial experiments with these spheres to form a closed cell foam centered on two approaches: 1) sintering without a binder, and 2) addition of an inorganic binder.

Samples sintered without a binder did not form closed cell foams on heating in air to 1300 K. Water absorption was about 70 wt. %. Samples held at 1300 K for more than one hour showed severe degradation due to collapse of the hollow spheres. All self-bonded samples were quite weak and friable and did not show much promise for producing a closed cell foam.

Eccospheres were then bonded with the following inorganic binders: 1) Ludox (Type HS, AS, TM, LS, E. I. DuPont Industrial Biochemicals); 2) phosphoric acid; 3) chromic acid; 4) calcium aluminate; 5) Astroceram (Granite State Machine Corporation); and 6) Cerambond 502, 510 (Aremco Products, Inc.). All samples were cast into silica molds, dried, and then fired at various temperatures up to 1300 K for periods of up to five hours.

In all cases, it was not possible to produce a closed cell foam with any of the above-mentioned inorganic binders, although significant increases in strength and handleability were observed. As our initial objective was the production of a closed cell foam, all attempts using Eccospheres were abandoned.

2. Cenospheres

The most successful approach to producing closed cell foams during the initial survey work was the self-bonding of cenospheres, both with and without binder additions.

The same binder additions as used in the Eccospheres were employed. In all cases, it was observed that a closed cell foam was achieved at the expense of some reduction in the refractoriness of the spheres plus a significant increase in fired density. It was then decided to concentrate the effort on self-bonded cenospheres without binder additions other than those required to enhance the re-radiation properties of the foam.

The description of cenospheres, and the properties of bodies formed from them, are detailed in Section III.

III. SELECTION OF MOST PROMISING APPROACH

A. General Description of Cenospheres

Cenospheres are a pollution by-product of coal burning power plants. When the pulverized coal ash emanating from the exhaust stacks of these furnaces is allowed to settle in collection lagoons, a small constituent of the ash (0.1 to 4.0 wt. %) floats on the surface. This floating fraction of the fly ash (cenospheres) consists of hollow microspheres of an alumino-silicate glass with diameters in the range of 20-200 micrometers. The thickness of the nonporous shells ranges from 2-10 micrometers. The tap density of the cenospheres varies between 250-400 kg/m^3, depending on the source. The evolution of carbon dioxide and nitrogen gases inside the alumino-silicate particles during their stay in the stack (several milliseconds at 1700 K) results in their expansion to cenospheres. It is believed that the formation of the hollow sphere is due to the presence of Fe_2O_3 and unburned carbon in the fly ash particle. In this mechanism, the carbon dioxide produced by the reduction of Fe_2O_3 to FeO, combined with the reaction of the alumina and silica to form an alumino-silicate glass, expands the glassy particle into a hollow sphere against the viscous forces in the glass and atmospheric pressure. The rapid passage of the fly ash particles through the steep temperature gradients causes the glass to "freeze" into the range of particle sizes observed (Ref. 2).

Although cenospheres come from many different sources, their chemical compositions are quite similar; this may indicate that their formation occurs only under a rather stringent set of conditions, perhaps favoring some particular quasi-equilibrium state.

Cenospheres are obtained from a domestic source (West Virginia) and an imported source (England). Table 2 gives the chemical analysis of the major constituents of both grades of spheres.

An X-ray analysis of the as-received cenospheres indicates the presence of a primary silicate glass phase with a small amount of mullite. Heating the cenospheres above 1500 K results in a significant crystallization of the glass into the mullite phase with a subsequent reduction in the amount of glassy phase. Since the cenospheres contain a large amount of silica (60 wt. %), it was expected from the alumina-silica equilibrium diagram shown in Fig. 1 (Ref. 3) that crystallization of the glass would lead to the formation of some cristobalite (or possibly quartz). This would lead to serious problems with the thermal stability of the material as the phase inversions associated with cristobalite or quartz formation would lead to a destruction of the material on thermal cycling; however, none of the crystalline forms of silica were observed during any subsequent heat treatments; the alumino-silicate equilibrium reactions are sufficiently sluggish to make the appearance of these phases unlikely.

The as-received cenospheres are subjected to decrepitation and separation. Separation is accomplished by floating the as-received cenospheres on n-heptane. The floating fraction is collected and used, while the sinking fraction is discarded. This leads to a more uniform and lower density starting material. The processed material is observed to be almost completely transparent, spherical hollow glass particles with size ranges from 50-100 micrometers (Fig. 2). The bulk density of these spheres is 320 kg/m^3, compared to 400 kg/m^3 for the as-received spheres. In addition, the separation process eliminates a large proportion of nonuniform, cloudy, and discolored material.

B. Properties of Sintered Cenosphere Bodies

In the initial survey, the as-received cenospheres were used. They were lightly tamped into silica molds and then fired to temperatures between 1400 and 1700 K for periods of 30 to 960 minutes. In this procedure, samples were quench-heated to the firing temperature, soaked at the firing temperature, and then quench-cooled to room temperature. Table 3 shows the effect of firing temperature and time on water absorption. It was observed that bodies fired to densities in the range of 430-650 kg/m^3 were not waterproof, whereas bodies fired to bulk densities greater than 800 kg/m^3 had low water absorption.

As the initial screening efforts indicated that nonfriable, waterproof, refractory bodies could be made by the above-mentioned procedures, environmental, thermophysical, and mechanical property measurements were obtained on these materials.

Environmental tests consisted of a radiant heat lamp simulation using quartz lamp heaters, for re-entry heating (Appendix A). Figure 3 shows a typical re-entry profile used on the front face of a specimen. The back face of the specimen was initially uninsulated in these screening tests so that very severe temperature gradients (typical of a shuttle re-entry) across the material were established (ΔT = 1100 K across a 2.54 cm plate). In later tests, the back faces were appropriately insulated to maintain a better simulation of the finite heat sink of a primary structure that can operate at 530 K.

The nonwaterproof materials were initially evaluated for stability to re-entry cycling. These specimens were 10 cm x 10 cm x 2.5 c plates with bulk densities of 430 kg/m^3. Figure 4 shows a typical re-entry profile of a CPI specimen. With the peak front face temperatures at 1390 K, the maximum back face temperatures reached 610 K. These specimens survived 6 to 10 cycles before some thermal fatigue cracks were observed. One of the specimens was soaked with water and subjected immediately to the thermal cycle. It cracked on the first cycle.

The waterproof samples with densities of 720-800 kg/m^3 and thicknesses of 2.54 cm failed after two cycles, where the back faces reached 700 K. Thermal cycle tests on waterproof samples indicated that the number of cycles to failure was a function of specimen thickness and density; for example, with a front face temperature of 1500 K, specimens with thicknesses of 1.60 cm survived 5 to 6 cycles, whereas samples with thicknesses of 2.54 cm or greater survived 1 or 2 cycles. Finally, samples of thickness less than 1.00 cm survived 10 cycles without failure.

This thickness effect on the thermal shock resistance of ceramics is consistent with the result that smaller nonlinear thermal gradients occurring across a thinner sample lead to smaller thermal stresses, due to the finite expansion coefficient of the material. It should be pointed out that the thermal shock resistance of a ceramic is a complex function of the material properties, geometry, and the nature of the environmental heat transfer conditions (Refs. 4-23). Most empirical or theoretical expressions designed to predict thermal shock resistance of ceramics do not apply to thermal fatigue problems (i.e., the reuse capability of a material undergoing thermal cycling has not been successfully predicted).

In no instances did the thermal shock failures result in spalling, powdering, or disintegration of the material. Hairline cracks developed in the specimens after cycling and some discoloration occurred (i.e., from a light tan to a reddish brown). The discoloration is probably caused by the reoxidation of FeO dissolved in the glass to Fe_2O_3 (hematite); however, this could not be confirmed by X-ray analysis due to the small quantity of iron oxide in the material. Microscopic examination of the cycled specimens showed no degradation of the material.

The back face temperatures of the low density materials (430 kg/m^3) were lower than denser materials of the same thickness, indicating that the lighter materials have lower thermal conductivities. This again is to be expected because the solid component of the thermal conductivity for these former materials should be lower. The thermal conductivity of the 430 kg/m^3 material was measured at several temperatures in vacuum, using a guarded hot plate method. The results are shown in Table 4.

Several other preliminary measurements were made on these early cenosphere specimens. Some of the pertinent results are:

1) The thermal expansion of the material measured over the temperature range from 293 to 1473 K was 4.5×10^{-6}/ K;

2) In the area of mechanical testing, specimens 10 cm x 1.50 cm x 0.63 cm were tested to failure in three-point bending. Strength ranged from 3.23 to 17.5×10^6 N/m^2; mid-span deflections ranged from 7.62 to 14.5×10^{-5} m at failure; and flexural moduli ranged from 10.3 to 14.6×10^9 N/m^2;

3) Diffuse reflectance measurements at room temperature from 0.25 to 15 micrometers were made to estimate the total normal emittance values at 1500 K. In obtaining the spectral emissivity values, two different measuring techniques were used. In the 0.25 to 2.2-micrometer region, a solar source and integrating sphere were used; the accuracy of the measurements in this region is about 1.5 percent. In the 2 to 15 micrometer region, a heated cavity source was used. Because of the weak source used, the specimen was placed inside the heated cavity (in a water cooled sample holder) and optics were devised so that diffuse reflectance measurements could be made outside the cavity. The error due to geometrical factors is about 3 percent; however, the error introduced because the sample reaches temperatures as high as 473 K, within the heated cavity, could be as large as 10 to 15 percent (depending on the emissivity of the sample at this temperature). Consequently, there is some mismatching between the spectral emissivity values in the overlap region (2 to 2.2 micrometers). The

emissivity values as a function of wavelength for the short and long wavelength regions are presented separately in Figs. 5a and 5b with the shorter wavelength region being more accurate. The room temperature emissivity values when weighted with the Planck blackbody distribution function and integrated over the spectrum of wavelengths permit the calculation of the total normal emittance as a function of temperature. These values varied from 0.45 to 0.5 at 1500 K depending on specimen preparation. The higher emittance values occurred when the specimens were quenched from 1700 K to freeze in any defect structure (Figs. 6a and 6b). It is postulated that some of the Fe_2O_3 in the cenospheres was converted to Fe_3O_4, giving rise to the enhanced emittance; however, this reaction is not oxidation-stable at atmospheric pressures. From these studies, it was concluded that the alumino-silicate system with the iron oxide additive in the cenosphere does not have an emittance suitable for a re-radiative heat shield.

C. Selection of High Emittance Additives

To take advantage of localized absorption bands, rare earth and transition metal oxide additions to the cenospheres were considered. It was decided that the additives that could have the greatest effect on increasing the high temperature normal emittance of the cenosphere system were CoO and NiO. These oxides are oxidation resistant and chemically compatible with the cenospheres. To take advantage of the localized absorption bands of these oxides in the 1 to 2 micrometer range, it is necessary that the valence states of the Co and Ni remain as 2+. This should be the case when they are added to the cenospheres to form cobalt and nickel aluminate spinels, CoO or NiO, or dissolved into the glassy phase. In the glassy state, the Co^{2+} or Ni^{2+} can coordinate in several different ways and this should aid in broadening the absorption region.

Initially, nominally 4 wt. % CoO was added to the cenospheres to enhance the radiation absorption to scattering ratio above that of the pure material. Large amounts of CoO or NiO additives, while increasing the amounts of Co^{2+} and Ni^{2+} ions within the cenosphere system, could also result in different coordinations for the Co^{+2} or Ni^{+2} ions within the glass, giving rise to broader absorption bands. However, excessive additions of these absorbers could result in an enhancement of scattering as well as a significant reduction in the refractoriness of the starting material.

Samples containing 4 wt. % CoO and NiO were prepared and fired to 1620 K for 0.5 to 4.0 hours to form bodies with noninterconnected cells and with densities in the range 575 to 670 kg/m^3. Spectral emittance measurements were made and the total normal emittances calculated (Figs. 7 and 8). The calculated total normal emittances of the CoO and NiO specimens at 1500 K were 0.62 and 0.60, respectively. In the 1- to 2-micrometer region, the absorption of the specimens with the CoO addition was greater than that of the NiO. In the longer wavelength regions (4 to 15 micrometers), the reverse was true. Since the total normal emittance is the integral of the room temperature spectral emittance times the Planck blackbody distribution function, the various sum of contributions to the integral (at 1500 K) from the short and long wavelength regions gave similar results. Based on these emittance studies, no clear-cut advantage of CoO over NiO could be derived; however, the CoO additive yielded waterproof bodies of lower density. This additive was deemed therefore to be more promising for further study.

D. Properties of Cenosphere Bodies with Cobalt Oxide Additions

Small pellets containing varying amounts of CoO additives were fired for various times at temperatures from 1500 to 1700 K. Compositions ranged from 2 to 12 wt. % CoO additive. Firing times ranged from 15 minutes to 4 hours. From this study, the following results were obtained:

1) Materials with a noninterconnecting network of cells were obtained for all compositions in the density range of 435-450 kg/m^3 (Figs. 9 to 11).

2) Increasing the cobalt oxide concentration led to a reduction in the refractoriness of the cenospheres (i.e., 2 wt. % bodies remained undistorted at 1720 K, whereas vitrification and distortion appeared in 12 wt. % bodies at 1640 K).

3) The fired densities for each concentration studied went through a minimum versus temperature. The widths of the minima depended on the concentration and firing times. Figures 12 to 14 show the observed trends.

4) The lower cobalt oxide concentrations had smaller pore sizes than the more concentrated CoO additions for comparable densities. Figure 15 shows SEM micrographs of typical sintered bodies. Figures 16 and 17 show optical micrographs of 4 wt. % and 12 wt. % CoO CPI bodies fired at various temperatures.

5) If the materials were inserted into the furnace at too high a temperature, for too short a soak time, they would develop a large amount of open porosity, causing their water pickup to increase. In this situation, the pores would open beyond the point where the sintering effects, for these short times, could act effectively to close up the interconnected pore regions. An example of this type of behavior is observed for the 4 wt. % CoO containing specimens fired for half an hour above 1623 K. If the firing temperature were increased to 1723 K for this fixed time, then the materials undergo more vitrification, becoming more waterproof but also more dense.

6) Insertion of the higher CoO-containing materials into the furnace at too high a temperature resulted in these samples' having very large nonuniform interior gas pockets surrounded by waterproof vitrified regions. In this situation, the density and weight percent water absorbtion of the specimens decrease with increasing temperature. An example of this type of behavior is observed for the half-hour firings of the 12 wt. % CoO specimens above 1700 K. The higher CoO concentrations lowers the refractoriness of the material and when the temperature is high, the entrapped gas within the cenospheres gives rise to a combination of pores and gas pockets that are very large; liquefaction effects are now primarily responsible for sealing the interconnected regions and significant distortion of the

pellets is observed. A vertical bar on the plots indicates where deformation of the various materials became noticeable.

7) The specimens having very small water pickup probably have lower weight percent gains than those given. These samples are small and residual water remaining within the pores of their surfaces could cause error in these measurements.

From these results it was deduced that the final fired bodies have structures and properties that arise from two predominant competing processes: 1) the high temperature produces the normal shrinkage (i.e., vitrification) effect due to a reduction in the internal surface area as observed in the pure material; and 2) the addition of the CoO acts as a fluxing agent in the glassy phase, lowering the glass viscosity. The entrapped gas within the cenospheres, acting against the forces of viscous flow and atmospheric pressure, causes the cell walls to expand and coalesce (depending on temperature and time), accounting for the variation of cell size with heat treatment. These results are analogous to the original experiments with pure cenosphere bodies. Recent studies have shown that pure cenosphere bodies with noninterconnecting cell networks can be produced in the density range of 610 kg/m^3 if appropriate controls are maintained.

E. Initial Scale-Up Efforts

1. Preliminary Considerations

Initial scale-up efforts were concentrated on the production of 7.6 cm (3") diameter plugs and 10 cm x 15 cm x 2.5 cm (4" x 6" x 1") tiles. Recognizing that the uniformity of the hot zone is important to the homogeneity of the finished fired product, two air-fired electric furnaces (Lindberg and Harrop) were chosen. These furnaces have internal dimensions of 30 cm x 30 cm x 30 cm (12" x 12" x 12") and 11 cm x 20 cm x 13 cm (4" x 8" x 5"), respectively. Both furnaces are front loading and can be opened after the selected firing cycle for faster cool-down.

Two types of firing schedules were adopted for this series of runs: 1) a step firing procedure; and 2) a continuous firing procedure. In the step firing procedure, the specimens were placed in a silica muffle and the furnace was slowly raised to a preselected temperature for periods of up to 1 hour to burn off the organics and to decompose the high emittance containing additive.

At the end of the heat treatment, the furnace level was raised to the maximum preselected temperature and held for a fixed time. The furnace was shut off and the specimen was allowed either to furnace cool or to cool more rapidly, by "cracking" the door slightly. In the continuous firing procedure, the specimens were placed in a silica muffle and a cam was cut out to change the rate of heating. In most firings, a smooth continuous firing cycle was chosen; however, some firings were chosen to simulate the step firings through appropriate cutting of the cam and by suitable changes in the power settings during the firing.

Three compositions were selected for these initial firings: 1) cenospheres with no additives; 2) cenospheres with 4 wt. % CoO additives; and 3) cenospheres with 12 wt. % CoO additives.

2. Specimen Preparation Procedures

The cenospheres and the cobalt additive were combined with an organic binder. The blended batch was pressed into various shapes and dried. The dried parts were then finish fired using the results of the smaller pellets as a guide. Table 5 summarizes the densities and water absorption of the fired parts.

3. Thermophysical Properties

a. Thermal Expansion. Measurements with a fused quartz dilatometer were made on small CPI samples. Expansion coefficients varied from 5 to 6 x 10^{-6}/ K over the temperature range 300 to 1500 K, depending on the amount of CoO additive; the higher the CoO additive the greater the expansion coefficient.

b. Differential Thermal Analysis. CPI samples containing no additives, and 4 wt. % CoO additives were run in the DTA to 1900 K. No obvious changes were observed other than a heat effect due to the glass transition temperature (see Figs. 18-20).

c. Thermal Conductivity. The thermal conductivity of CPI samples was measured using a radial heat flow method. Tables 6 to 8 give the measured values. These values are consistent with measured values for scaled-up tiles of CPI.

d. Emittance. Diffuse reflectance measurements are reported in Section III.C. Total normal emittance measurements on sintered cenosphere samples were measured to 1140 K (Ref. 24). Table 9 gives the measured values. These measurements led to the investigation of high emittance additives, as the total normal emittance had an unacceptably low value for a Space Shuttle application. The total normal emittance of cenospheres with 4 wt. % and 12 wt. % additives are presented in Tables 10 and 11. It should be noted that slightly higher emittances were observed in some of the scaled up tiles; however, the dramatic effect of CoO on the total normal emittance is clearly demonstrated.

4. Mechanical Properties

Three-point bend tests were performed on pure self-bonded cenospheres. Fired densities were 640 to 800 kg/m^3. Maximum values of 17.5×10^6 N/m^2 (2800 psi) were observed. Results of three-point bend tests performed on CPI with 12 wt. % CoO are shown in Table 12. The compressive strength of a self-bonded cenosphere body of density 800 kg/m^3 was 58×10^6 N/m^2 (9300 psi). Sonic elastic modulus measurements of a CPI tile (ρ = 656 kg/m^3) containing 12 wt. % CoO were performed at NASA Langley (Ref. 25) at temperatures up to 1255 K. Results are shown in Fig. 21. No significant fall-off in the modulus is seen until 1030 K.

5. Environmental Tests

The environmental test setup, utilizing the radiant heat lamp facility, is discussed in Appendix A. Our initial evaluations were made on 2.6 cm diameter and 10 cm x 10 cm plates of varying thicknesses. Two test configurations were used for the initial evaluations: 1) the sample was not insulated on the back face and was allowed to "free radiate" to the surrounding air; 2) the sample was insulated on the back face with microquartz insulation that was supported by a 0.02 cm titanium plate to simulate the finite heat sink of the Space Shuttle. In the first configuration, the sample experiences more severe thermal gradients; this was used as an initial screening to find the maximum thermal gradients that the sample could sustain without failure. Results indicated that CPI can sustain thermal gradients of about 922-1061 K through its thickness without thermal stress failure. Thermal stress failures consisted of fine hairline cracks. No spalling of materials was observed under thermal cycling. Figure 22 illustrates a typical thermal profile and maximum temperature gradients of a CPI sample that is uninsulated.

For insulated samples, Fig. 23 illustrates the thermal gradients that are more characteristic of the re-entry condition, for samples that are 1 cm-thick The thermal gradients do not exceed the gradients necessary to cause thermal stress failure.

F. Final Scale-Up of CPI Tiles

After the initial scale-up was completed, it was decided that CPI should be scaled up to larger size tiles to facilitate design considerations. Arrangements were made with Rutgers University to use its gas fired kilns. These kilns are capable of a greater firing range than the electric furnaces used for the initial scale-up operation. Emphasis was placed on the production of 20 cm x 20 cm x 2.5 cm (8" x 8" x 1") tiles with reproducible properties from firing to firing. Processing procedures similar to those used in the preparation of small prefired tiles were adopted. Firing cycles were optimized to minimize the final fired density consistent with a closed pore structure.

1. Property Measurements of Scaled-Up CPI Tiles

After the firing of scaled-up CPI tiles was optimized, emphasis was placed on ensuring the reproducibility of thermophysical, mechanical, and environmental properties. This subsection is divided into three parts covering these categories. For this testing program, a total of six scaled-up CPI tiles, three of the 12 wt. % cobalt composition and three of the 8 wt. % cobalt compositions, were used. The 12 percent cobalt tiles were denoted as the R series and the 8 percent cobalt tiles were denoted as the S series.

a. Thermophysical Properties

1. Density and Physical Dimensions. Table 13 shows the dimensions and densities of the fired scaled-up CPI tiles used for the subsequent testing program. The S series tiles were not quite as uniform in appearance and pore structure as the R series tiles. The S tiles were thicker than the R tiles and the nonuniformity of the hot zone in the gas fired kiln had a greater effect on the fired properties. However, by firing thinner tiles (2.5 cm to 1.9 cm), complete uniformity was achieved.

2. Microstructure. The fired tiles had a foam-like appearance and were closed pore (i.e., the pores were not interconnected). Figure 24 shows scanning electron micrographs of typical 8 and 12 wt. % cobalt containing bodies. The average pore size of the S

samples was 170 micrometers and that of the R samples was 309 micrometers. These values are averages of measurements made on 10 micrographs for each series. The difference in pore size between the R and S materials is consistent with the effect of cobalt additions in this system. As mentioned, (Section III), the general microstructure of fired CPI depends on the action of the expanding gas entrapped in the cenospheres and the viscosity of the glassy cenosphere shell at the firing temperature. By adding cobalt oxide to the cenospheres, the viscosity of the glassy shell is decreased at the firing temperature. Thus, larger pore sizes are encountered with increasing cobalt oxide content due to the fluxing action of the cobalt. It should be noted that the average pore size of the fired CPI without cobalt additions is about 75 micrometers. The decrease of viscosity with increasing cobalt is also shown in the softening point data that are discussed later in this report.

The X-ray diffractograms of these blocks indicate the presence of mullite ($3Al_2O_3 \cdot 2SiO_2$), cobalt aluminate ($CoAl_2O_4$) and a glass phase. Table 14 compares the d-spacings recorded for the R and S tiles with the ASTM card file values. In general, as the cobalt addition increased, the amount of cobalt aluminate present increased while the amount of mullite decreased. Preliminary X-ray results indicate that the solubility of the cobalt oxide in the cenospheres is about 4 wt. %. At higher cobalt oxide additions, crystallization of cobalt aluminate occurs.

3. Water Absorbtion. Measurements were made by a simple immersion test. Samples (nominally 1 cm x 1 cm x 1 cm) were weighed and then immersed in a beaker of water at room temperature. A 5 cm head of water was maintained over the submerged piece and the piece remained submerged for 96 hours. The samples were removed from the beaker, dipped in alcohol to remove any water just held into the surface pores, and were then reweighed. The change in weight was recorded and the water absorbtion was calculated according to the following formula:

$$\% \text{ WA} = \text{Wt gained/Dry Wt of Block} \times 100 \qquad (1)$$

Table 15 summarizes the water absorbtion data. The low values of water absorption are consistent with a closed cell foam.

4. Thermal Expansion. Linear thermal expansion measurements were made on the R and S series samples. A fused quartz dilatometer was used and the slope of the percent linear expansion versus

temperature curve in the temperature region of 298 K (room temperature) to 1073 K was taken as the average linear coefficient of thermal expansion. It should be noted that all traces were linear in this temperature region so the slope approximation is valid. A heating rate of 473 K per hour was used on all runs. No phase changes were observed during the runs. Softening points of the glassy phase in the CPI samples were also extrapolated from the curves. Table 16 shows the results of this study. It can be seen from these data that as the cobalt content is increased in this system, the thermal expansion increases and the softening point decreases. Figure 25 shows the normalized expansion of the R and S series versus temperature.

5. Differential Thermal Analysis. DTA runs were made on the R and S series materials to verify their thermodynamic stability. The equipment used is described in Appendix B. Powdered samples were used in all runs and the reference material was alumina. Two typical DTA traces are shown in Fig. 26. It can be seen from these traces that there were no phase change or crystallization heat effects evident from room temperature to about 1500 K. The broad endothermic peaks at about 1700 and 1673 K for the S and R materials, respectively, are associated with the melting of the crystalline phases in the CPI with the aid of the fluid glassy phase. X-ray diffractograms of CPI powdered samples quenched from 2073 K showed no evidence of crystalline phases, i.e., the quenched material formed a stable glass.

6. Heat Capacity. These values were measured on the R and S series materials from room temperature to 723 K using a differential scanning calorimeter, which is described fully in Appendix B. The individual sample data, with series averages, are presented in Table 17 and the series averages are plotted in Fig. 27. The values recorded within each series were consistent; however, there was a statistical difference between the R and S series average values. This indicates that there is a real difference in the heat capacity of the R and S series materials and the difference is not a random variation effect. It appears that as the amount of cobalt additive is increased, the heat capacity decreases. The values for mullite, obtained from the literature (Ref. 23), are plotted for comparison in Fig. 27. As mentioned previously, as the cobalt content is increased in the CPI, more cobalt aluminate is formed at the expense of mullite. Because heat capacity is generally considered an additive function, it was expected that as the amount of mullite present decreased, the heat capacity should decrease, which was the observed effect.

7. Total Normal Emittance Measurement. The total normal emittance, in the temperature range 750-1533 K, was measured in a universal high temperature emissometer (Ref. 26). The experimental setup and measurement procedures are presented in Appendix C. Emittance measurements were made to verify the projected use of these CPI tiles in a re-radiative-type heat shield. Total normal emittances greater than 0.75 are necessary to allow CPI to be considered as a candidate heat shield material. Figure 28 is a plot of the emittance data. The straight lines drawn on this graph are a least squares fit of the data and are an indication of the trend. This tendency indicates that the emittance decreases slightly with increasing temperature for both the R and S materials. This is possible because the CoO additive may not sufficiently enhance the short wavelength absorbtion region (1 to [illegible] micrometers) so that even at 1470 K, the total normal emittance, which is the weighted integral over the wavelength of the spectral emissions times the Planck blackbody distribution function, may continue to drop. As the temperature continues to be increased above 1470 K, however, one would expect the shorter wavelength region to contribute more strongly, causing a reversal in this downward emittance trend. It is not clear from these experimental results whether the emittance-temperature behavior shown is indeed real; the maximum experimental error for a particular emittance value is 7 percent which is larger than the percent differences between the emittance values obtained. Future work, wherein the temperature dependence of the spectral emissivity is measured, should help resolve this point.

8. Thermal Conductivity Measurements. These measurements were made on the R and S series materials from 368 to 1478 K. The measuring system employed a radial heat flow across a hollow cylindrical sample. The experimental setup and measurement procedures are described in detail in Appendix D. The thermal conductivity at elevated temperatures is a measure of the heat transfer by solid conduction and radiation. All of the samples tested had approximately the same density, so that the contribution of the solid heat conduction was fairly constant. Due to the smaller pore size of the S series materials, it was expected that these samples would scatter the radiation component of the heat transfer to a greater extent resulting in a lower over-all thermal conductivity. However, because of this smaller pore size (at the same density as the R series samples), the walls between pores were thinner. This fact, combined with the lower cobalt content of the S series materials, accounted for a lower absorption capability. The R series materials, having a larger pore size, making them

less efficient scatters, have thicker walls between pores and a higher cobalt content causing their absorbtion to be greater (as can be seen in the emissivity data of Section III.F.1.a.7 as a result of the compensating effects of the competing scattering and absorption mechanisms described above, the thermal conductivity values of the R and S series materials were similar. These data are presented in Table 18.

b. Mechanical Properties

One of the major advantages of CPI is its superior mechanical properties. To characterize these properties, a comprehensive mechanical testing program was carried out. The program consisted of determining the flexural, tensile, and compressive properties of the CPI, with associated moduli, at room temperature (Refs. 27-29). Flexural properties were investigated using either single center point loading or quarter point loading. Tensile property measurements were made by a diametral compressive load application. Compressive properties employed an edgewise loading configuration. A full description of all test procedures, sample configurations, and calculation formulae is presented in Appendix E. The results of this investigation are presented in Tables 19 through 24.

A summary of the average mechanical properties of the R and S series materials is presented in Table 25. Figures 29 and 30 graphically depict the stress-strain (or deflection) behavior of the R and S series materials for flexural (center point) and edgewise compressive properties.

It should be noted that mechanical properties of the R and S series samples were fairly consistent. However, sample S-3 gave anomalously low breaking strengths and flexural moduli in both three and four point loading. This may have been due to nonhomogeneities encountered in this sample after firing. Additional fired scaled-up tiles were tested to see if the lower values recorded for sample S-3 were reproducible. The samples showed higher strengths and lower data scatter. These data are presented in Tables 26-28.

c. Environmental Testing of Final Scaled-Up CPI Tiles

1. Radiant Heat Lamp. The radiant heat lamp facility (Appendix A) was used for the testing of the CPI tiles. Of the six 20 cm x 20 cm x 2.5 cm (8" x 8" x 1") tiles, one section was cut out of each [10 cm x 10 cm x 1 cm (4" x 4" x 0.375")].

Each sample was subjected to 10 simulated re-entry cycles as shown in Figs. 31 and 32. In both cases, the back faces were insulated with microquartz fibrous insulation to simulate the heat transfer rates to the primary structure. All samples survived the cycling without obvious failures (cracks), change in appearance, or loss of closed pore nature. As samples containing 12 wt. % CoO showed a slight tendency to buckle at 1500 K (2200°F), it was decided to cycle this composition up to a maximum temperature of 1370 K (2000°F). Current indications are that the CPI with 12 wt. % CoO is dimensionally stable to 1370 K and the CPI with 8 wt. % CoO is stable to 1500 K. Table 29 summarizes the cyclic testing data on the two compositions tested.

2. Plasma Arc Jet Tests. Ten cyclic tests were performed in the Aerotherm arc plasma facility (the facility and experimental parameters are described fully in Appendix F) on two CPI specimems, each with different amounts of cobalt oxide emittance additive (8 wt. % and 12 wt. %). The test environment simulated entry heating conditions for external insulation on the Space Shuttle vehicle (Ref. 30).

The test specimens were two 180-degree sections, 1 cm thick fabricated by Aerotherm from two Grumman-supplied 7.6 cm x 12.7 cm slabs. Test conditions and model response were defined by measurements of heat flux (centerline) enthalpy, energy balance (bulk) enthalpy, static pressure (essentially stagnation pressure), stagnation point heat flux, surface temperature history, and back wall temperature history as defined by six thermocouples. Specimen response was also defined by surface recession, mass loss, and radius change measurements.

The sequence of testing, shown diagramatically below, consisted of first inserting the calibration model at the lowest conveniently achievable arc condition consistent with the attainment of the nominal 1477 K maximum surface temperature, and then inserting the model at this low condition. The lowest condition was held for

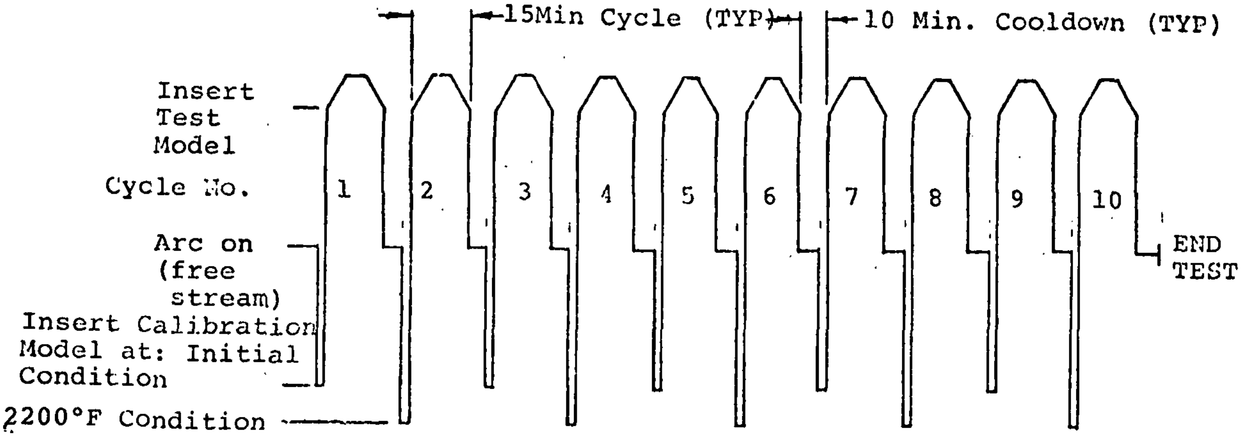

1 minute; then the arc heater current increased at a rate of about 366 K/minute for the next 4 minutes. After then holding constant arc heater current for 5 minutes, a 5-minute cool down was imposed that was simply the reverse of the 5-minute warmup. The second calibration model insertion was accomplished at the condition that yielded 1477 K on the 8 wt. % CoO CPI specimen.

Prior to the cyclic tests, calibration tests were performed to define the 1477 K condition and the greatest possible range of conditions below this maximum temperature. These operating conditions were then set for the subsequent cyclic model tests. Figure 33 shows a typical time temperature response of the CPI front and back faces during exposure.

The calibration test results are summarized in Table 30 and the model test results are summarized in Table 31. A discussion of these results follows, using the tables as an outline.

The calibration test results (Table 30) show the initial conditions set for the cyclic tests and two other typical higher conditions. The heat fluxes shown for the two higher conditions were not required to achieve the 1477 K surface temperature but indicate the trend of heat flux and pressure. The off-centerline pressures indicated are within 5 percent of the centerline (stagnation) pressure based on past experience with the 4 1/2-inch diameter calibration model. The cold wall heat flux shown is the stagnation point calorimeter output for the calibration model.

The calibration model was inserted alternately at either the initial model insertion condition or the 1477 K model condition to check arc heater performance at the beginning of each cycle. Also, the arc operating data at the halfway mark during each cycle is shown (steady 1477 K). The static pressure indicated is that measured at the test model pressure tap whereas no static pressure is available for the calibration model due to its brief insertion into the test stream for the stagnation point heat flux measurement.

Surface and back wall temperature histories are combined for a single typical cycle in Fig. 33. No result is shown for the thermocouple at Station 3 (see key, Fig. 33) due to an open circuit condition. Note that linear heating from, and cooling to, ambient temperature was not possible since the minimum arc operating condition yielded a surface temperature of about 1154 K. This rapid splash occurred during the first 1 minute of each cycle while the arc condition was held at the initial, minimum condition. An approximately linear warmup from this point to 1477 K was achieved during the next 4 minutes of cycle time.

During cycle 4, a radial crack was observed on the 8 wt. % CoO CPI specimen with another crack being noticed during cycle 7. A crack was first noticed in the 12 wt. % CoO CPI model during cycle 8. The initial temperature rise from ambient to 1154 K over about a 1-minute period is significantly more severe than that for an actual re-entry trajectory. The cool down from 1154 K to near ambient after each cycle also represented a more severe temperature-time variation. The tests were, therefore, more severe than desired with respect to thermal shock response. [During a typical Space Shuttle re-entry maneuver, the surface temperatures would not exceed 340 K (150°F) during the first 60 seconds as compared to 1154 K (1600°F) in the arc jet. The length of time required to achieve surface temperature of 1154 K (1600°F) is 375 seconds.]

Although each specimen broke into five pieces, as discovered during the removal from the specimen holder, it is believed that the mass loss data are reasonable since the breaks were very clean and no significant chips were lost. The radius change measurements may be somewhat in question due to the necessity of reconstructing the specimens for the post test check. The surface recession (negative value for specimen growth) range for each specimen was found by locating the thick and thin spots with a flat anvil micrometer.

Post test examination of the cycled specimens after they were returned to Grumman yielded the following observations:

1) Both 8 wt.% and 12 wt. % CoO specimens showed a slight color change from a dark blue-black to bluish-white. These color changes have also been observed with specimens subjected to high temperature vacuum environments in the total normal emittance and thermal conductivity measurements. These measurements indicated no effect of the color change on emittance or thermal conductivity and are consistent with the reproducibility between runs in the Aerotherm Data (See Table 31).

2) The cracks observed in both of the cycled specimens may have been due to "stress raisers" inadvertently introduced into the machined specimen's periphery at the location of the 12 stainless steel pins used to support the specimen (see Appendix G). This is confirmed by the fact that many of the cracks observed appeared to have been initiated at the location of the pins and were radial

in nature. This would not be expected for randomly formed cracks due to thermal stresses on cycling.

Another possibility may have been artificially induced stresses generated due to the thermal expansion mismatch between the stainless steel support pins and the CPI specimen during the cycling. These points have not been resolved.

3) The pore size distribution on the surface exposed to the arc jet was not changed after exposure.

G. NDT Inspection of CPI After Re-entry Exposure

For any candidate heat shield material to be considered for use on the Space Shuttle, it is necessary to have a rapid, reliable, nondestructive technique for determining the uniformity of the material. It is also desirable to nondestructively record the degradation, if any, of a heat shield material after multiple re-entry cycling. When a ceramic material is stressed, as in thermal cycling, deformation and changes in the microstructure can occur. When the stress is removed, the deformation ceases, but the material seldom regains its original shape, retaining some finite deformation and microstructural change. For this reason, a plot of stress versus strain is not a straight line, but a hysteresis loop. The area within this loop represents the energy dissipation or mechanical damping of the material. This "lost" energy can be dissipated in viscous flow, vibration and friction between molecules, and at macroscopic faults such as pores and cracks. A measurement of mechanical damping can thus indicate if a material has poor internal bonding or cracking, both of which may affect its performance. In this particular case, by measuring the mechanical damping capacity of CPI before simulated re-entry and then after repeated cycling, an indication of the adverse effects of the cycling on the material can be determined.

The mechanical damping capacity was determined by a sonic method. The test sample was a rod of CPI about 10 cm long with a rectangular cross section approximately 1 cm by 0.625 cm with small metal disks glued on each end. The sample was supported at its nodal points (0.224 and 0.776 times the length). A sine wave generator had its output amplified, and this signal was applied to a driving coil. The resulting varying magnetic field in the vicinity of the coil affected the metal spot glued on one end of the sample. The bar vibrated and the metal spot at the other end of the rod moved within the magnetic field of a second coil, inducing an a.c. voltage. This voltage was amplified and displayed on an oscilloscope as a sine wave. A frequency counter indicated the exact frequency. The fundamental resonance frequency and the sine wave half height frequencies were taken directly from the oscilloscope screen and frequency counter. The following formula was used to determine the mechanical damping capacity (Ref. 31):

$$\tan \delta = \frac{U_H - U_L}{\sqrt{3}\, U_R} \tag{2}$$

where

U_H = the upper half height frequency

U_L = the lower half height frequency

U_R = the resonance frequency

Once the resonance frequency was found, Young's modulus could be calculated from the following formula (Ref. 31):

$$E = 0.94642 \frac{\rho \ell^4 U_R^2}{t^2} T \tag{3}$$

where

E = Young's modulus

ℓ = sample length

t = sample thickness

U_R = resonance frequency

T = correction factor

ρ = density of sample

In this way, any changes in Young's modulus due to cycling could be determined and the modulus data recorded from destructive techniques was cross checked. This testing technique is presently in its initial stages and only one 8 wt. % cobalt tile and one 12 wt. % cobalt tile were characterized. The results of this investigation are presented in Table 32. There were no strong trends in the data with cycling. It should be noted that there was no drastic drop-off in Young's modulus or increase in tan δ with increased re-entry cycling, indicating that the CPI was not degraded by repeated re-entry cycling. However, it is difficult to draw any firm conclusions from this limited data. The apparent increase of Young's modulus in the 8 wt. % cobalt sample cycled five times is not fully understood at this time. The Young's modulus values obtained by this sonic technique for the uncycled samples were consistent with the values calculated from the breaking strength data (Section III.F.1.b).

IV. THEORETICAL CONSIDERATIONS

We have shown that in order to calculate accurately the temperature distribution in a ceramic heat shield, it is necessary to use a radiative transfer model that uses the radiation parameters of absorption and scattering coefficients (Ref. 32). The usual heat transfer model that is used to calculate temperature distributions in heat shields at re-entry conditions can give significantly lower estimates of surface temperatures and gradients than predictions based on a more rigorous radiative transfer model. This result is due to two assumptions that are used in the usual model. The first is that the radiation emitted from the heat shield can be described by the Stefan-Boltzmann equation $q_{rad} = \sigma \epsilon T^4$. This law is only valid for an isothermal case or is a good approximation for an opaque material where emission occurs in a sufficiently thin surface layer such that there are no significant temperature gradients. In a ceramic, the absorption coefficients are not high enough to make the material sufficiently opaque such that the Stefan-Boltzmann equation can be used at re-entry conditions where the high heat fluxes and low thermal conductivity give large temperature gradients. As a result, emission occurs from volume elements at different temperatures and the concept of emissivity loses its significance. The other assumption that is made is to use the measured temperature dependent thermal conductivity in the heat conduction equation to determine the temperature distribution. This assumption implies that solid conduction and radiation transfer can be treated simultaneously as a diffusion process with the driving force proportional to the local temperature gradient. This assumption, however, is not valid near the surface of the material where the diffusion approximation cannot be made due to surface losses of radiation.

The radiation transfer model treats the process of thermal conduction and radiation transfer simultaneously and does not contain the above assumptions. The parameters of absorption and scattering coefficients replace the parameters of emittance and the radiative component of the thermal conductivity.

The best way to obtain the absorption and scattering coefficients is through measurements of the diffuse reflectance and transmittance of a thin sample at various wavelengths and temperatures; however, a rough estimate of the scattering and absorption coefficients can be obtained from measurements of the isothermal emittance and thermal conductivity. The ratio of absorption to scattering coefficient can be obtained from the emittance measurement by using the following equation (Ref. 32) for the emittance:

$$\epsilon_N = \frac{4n^2}{3\left(1 + \frac{s}{a}\right)^{\frac{1}{2}} + \frac{2(1 + R)}{1 - R}} \tag{4}$$

where s, a, and n are the scattering coefficient, absorption coefficient, and index of refraction, respectively. R is the diffuse internal reflectance that can be obtained from the index of refraction, which is estimated to be 1.1 based on knowledge of the material composition and the use of well-known mixture rules (Ref. 5). Using a measured value of 0.8 ± 7 percent for ϵ_N (i.e., $\epsilon_N = 0.856$ and $\epsilon_N = 0.744$), the ratio s/a of scattering to absorption is estimated to vary from 1.3 to 3.2 (i.e., relatively large changes in the s/a ratio produce small changes in the measured emittance). We also note that absorption and scattering are comparable in magnitude.

The sum of absorption and scattering coefficients can be obtained from a knowledge of the radiative component of thermal conductivity, which is given by the following equation:

$$k_{rad} = \frac{16n^2\sigma T^3}{3(a + s)} , \tag{5}$$

where $\sigma \equiv$ Stefan-Boltzmann constant.

This equation indicates that increasing the absorption and scattering coefficient reduces the thermal conductivity. This may be achieved through reduction in the pore size or through additions of a radiation absorber. The radiative component of conductivity can be obtained from measurements of the total conductivity by subtracting out the solid conduction component, which is assumed not to vary with temperature. At room temperature, the radiative conductivity is assumed negligible and, therefore, the value of radiative conductivity can be obtained by subtracting the measured room temperature value from the total conductivity measured at elevated temperature. The results for the 12 wt. % CoO-doped sample is shown in Fig. 34 where the radiative conductivity is shown as a function of temperature. Also shown is the sum of absorption and scattering coefficients as obtained from Eq. (5). The results show that the sum of the coefficients increase significantly with temperature from a value of 10 cm^{-1} to 50 cm^{-1}. The relatively low (for a ceramic) scattering coefficient is consistent with the microstructure of the material, which consists of cells 200-300 micrometers in diameter. The cell walls act as scatterers, with a mean free path of about a cell diameter. The increase in the scattering and absorption with temperature can be attributed to increased scattering within the cell walls at shorter wavelengths due to inhomogeneities in the material. In addition, at higher temperatures the high localized absorption in the Co^{2+} ion at 2 micrometers becomes more significant since these coefficients are weighted average values with the weighting function related to the blackbody distribution function that peaks at shorter wavelengths as the temperature increases.

In summary then, the measured values of isothermal emittance and thermal conductivity give us rough estimates of the absorption and scattering coefficients. These are of the same order in the range between $10\ cm^{-1}$ and $50\ cm^{-1}$ and increase with temperature. To obtain better estimates of these parameters for thermal analysis, higher accuracy spectral measurements of the optical properties would be required.

V. DESIGN OF CPI HEAT SHIELDS

Although our major efforts have concentrated on the production, scale-up, and reproducibility of CPI heat shields, we have investigated some preliminary heat shield configurations that will allow the designer to take advantage of the CPI properties and to "design out" the inherent problems associated with CPI. Table 33 describes the characteristics of a CPI heat shield.

The two problems associated with CPI are: 1) a high fabricated density (500 kg); and 2) inability of the material to survive without development of hairline thermal stress cracks (due to the steep thermal gradients during re-entry cycling) in thicknesses necessary to bring the back face into the 400-590K range of the primary structure of the Space Shuttle Orbiter.

Because our experience has shown that thicknesses up to 1,25 cm can survive a typical re-entry thermal cycle to 1500 K, we have examined three composite heat shield designs that can overcome the two problems discussed above. The features of each are discussed below.

A. Shell Structure

In this configuration, we reduce heat shield weight by backing it with a layer of lightweight (48 kg/m^3) fibers such as microquartz or Dynaflex, etc. The higher density of the CPI is partially offset by the low density fibers. Figure 23 shows a typical re-entry cycle in which the CPI is backed with 2.5 - 5.0 cm of microquartz fibers that are supported on a titanium plate 2 x 10^{-3}m. It is seen that such a configuration is effective in reducing the titaniu back face temperature to acceptable levels. In practice, the microquartz fibers would be "bagged" in a thin metallic foil to protect them against damage and moisture. The CPI plate is supported on its sides by a thin vertical plate of CPI (or a honeycomb) that is bonded to the top plate with either mechanical fasteners, a high temperature adhesive, or a combination of both for increased reliability. Such a configuration is shown in Fig. 35 in which four CPI heat shields 15 cm x 15 cm x 5 cm have been assembled onto a primary substructure and have been fastened into the primary structure using a Dzus-type mechanical fastener. The ease of machinability of the CPI is apparent in the "interlocking" of the joints between each heat shield and in the placement of a replaceable plug from which front access to the back face fastener of the heat shield with a screwdriver is possible.

B. Metallic Honeycomb Substrate

In this configuration, we support a face sheet of CPI (up to 1.2 cm thick) on a lightweight metallic honeycomb constructed of titanium, Inconel, Hastelloy, Haynes 188, or an appropriate alloy for the temperature range of interest (see Fig. 36). The cells of the honeycomb are filled with lightweight refractory fibers (i.e., microquartz). This technique has been made possible by the discovery that it is possible to embed (attach) the CPI and a lightweight fiber blanket into a metallic honeycomb using ultrasonic waves coupled to the metal as the "drill" (see Appendix G for details).

Using this procedure, we have developed a strong mechanical interlock between the honeycomb core and the CPI.

The characteristics of such a composite heat shield are:

1) The CPI face plate can act as the primary reradiative re-entry heat shield.

2) The oxidation resistant metallic honeycomb adds ruggedness, reliability, and support for the CPI plate.

3) The lightweight fibers are now protected from damage and water absorption in each cell by the walls of the cell, the metallic back face sheet, and the CPI front "face sheet."

4) The strong mechanical interlock between the CPI and the honeycomb core provides a "fail safe" feature if there were a localized failure in the CPI (i.e., the heat shield would "hold together" during launch, or re-entry until a replacement was installed).

5) The brittle CPI is "strain isolated" from the support through the ductile honeycomb core material.

6) The back face of the heat shield is metallic, facilitating mechanical attachment schemes to the prime structure.

Although a considerable amount of testing of CPI heat shield configurations is necessary to establish the shield's re-use capability, a preliminary analytical study was done to evaluate the thermal performance of the system, consisting of a CPI face sheet embedded into an Inconel 718 and titanium core with microquartz insulation in the honeycomb cells and a back face sheet of the respective core material. In addition, a layer of 0.089m bagged microquartz insulation was placed between the honeycomb panel and the primary structure. Figures 37-40 show the thermal response required to achieve a 450 K back face temperature of an aluminum structure. Table 34 gives the weights of the various configurations studied. Although this study is only preliminary, the weights computed are competitive with the coated RSI heat shields (i.e., 14.5 kg/m^2). Further work will be done to optimize this system.

Although the re-entry heating profile used in this calculation was slightly different than the profile used with the heat lamps, the maximum backface temperatures calculated agreed with experimentally measured values during the steady state portion of the cycle.

VI. DISCUSSION OF RESULTS AND CONCLUSIONS

The ultimate use of this material as a component of a TPS will require a materials-design interaction investigation such that the properties of CPI are fully utilized, and that the problems associated with the material are accommodated through design approaches that seek to minimize them. Several suggestions for future effort have been made (Section VII); however, other approaches are sure to be envisioned.

In summary, we state the following conclusions:

1) Glass-ceramic foams with noninterconnecting porosity can be produced using fly ash cenospheres as the raw material (i.e., water absorption $\sim$ 1 percent).

2) The emittance of the foam can be enhanced significantly (i.e., $\epsilon_N = 0.8$) with additions of cobalt and nickel oxides without an adverse change in the noninterconnecting pore network.

3) Densities of 450-560 kg/m^3 may be attained in scaled-up components of CPI.

4) Thermal conductivity of CPI is comparable to the rigidized fibrous insulations at elevated temperatures.

5) Strength of CPI components is significantly greater than rigidized fibrous insulations.

6) Scaled-up components of CPI (20 cm x 20 cm x 2.5 cm) have been made.

7) Reproducibility of thermal and mechanical properties of CPI components in scaled-up components has been demonstrated.

8) CPI (10 cm x 10 cm x 1 cm) tiles have successfully undergone at least 10 simulated re-entry cycles to 1500 K in a radiant heat lamp facility and in a plasma arc jet facility without significant degradation.

9) NDT inspection of CPI tiles using a sonic modulus technique after re-entry cycling has shown no significant degradation of the material.

10) Full size prototype heat shields have been fabricated that demonstrate the ease of machinability of CPI.

11) Mechanical attachment of composite CPI heat shields to the primary structure has been demonstrated.

12) Techniques for embedding CPI into metallic honeycomb substrates to facilitate mechanical attachments to the prime structure have been demonstrated.

13) Theoretical models correlating radiation absorption and scattering in CPI foams with thermal conductivity and emissivity have been investigated.

VII. RECOMMENDATIONS FOR FUTURE WORK

A. Current Materials

Future work with the currently scaled-up components of CPI should be directed toward further characterization of the thermal, mechanical, and environmental properties of the CPI with 8 wt. % CoO and CPI with 12 wt. % CoO. In addition, considerable design work with CPI heat shields is essential.

Because a detailed knowledge of the mechanical properties of CPI is an important part of a design effort as well as the materials characterization effort, we propose the following areas for future investigation:

1) Determination of the mechanical properties of fired CPI tiles at elevated temperatures (i.e., to 1500 K). This would include tensile strength, compressive strength, bend strength, shear strength, strain to failure, and elastic modulus. In addition, some creep data of the strength of CPI under simulated re-entry loading should be determined. Finally, the room temperature strengths of CPI samples that have been subjected to re-entry cycling should be determined to assess the effects of cyclic usage on properties.

2) Future work on thermal properties should be directed toward a determination of the effects of thermal cycling on the thermal conductivity and total normal emittance of CPI, both in a radiant heat lamp facility and in the plasma arc-jet facility.

3) Future work on environmental properties should be directed toward several areas:

    a) Upper use temperatures for CPI tiles should be established by recycling to higher and higher temperatures until failure.

    b) The thermal overshoot capability of CPI should be established.

    c) Extension of the number of cycles beyond the 10 chosen is essential to assess the maximum amount of cyclic usage of CPI.

d) The thermal shock resistance of CPI should be characterized further by establishing its dependence on heating rates and plate thickness.

e) Salt spray tests and their effects on degradation of CPI after thermal cycling should be assessed.

f) Rain erosion tests should be performed.

g) Acoustic and vibrational tests should be performed.

h) To identify failure modes of CPI materials, basic work should be undertaken to measure fracture energies and to relate these to thermal shock parameters in the material.

B. Development of New CPI Compositions

In addition to the above work on further characterization of current CPI materials, an effort is needed to improve the properties of the current materials.

Because the thermal expansion coefficient plays a major role in determining the thermal shock characteristics of ceramic materials, we recommend that additions to the cenosphere should be pursued that will have a dramatic effect on the expansion coefficient. To this end, additions of lithium- or magnesium-based compounds should be tried to move the over-all compositions of the cenosphere (which are primarily an alumino-silicate) toward the beta-spodumine, petalite, or cordierite compounds. At such time when a low expansion CPI material is developed, emittance additions such as cobalt or nickel oxides should be incorporated into the foam structure. As with other CPI compositions that have already been developed, a complete evaluation of the material properties should be made.

Because a higher temperature capability of the current materials is being sought, we recommend that a search be made for high emittance additions that will not compromise the refractoriness of the as-received cenospheres but that will enhance the emittance of the current material. Since we know that cobalt and nickel oxides tend to flux the glassy phase in CPI, one approach we suggest is to cut back on the cobalt and nickel oxide additions and investigate the effect of additions such as refractory nickel or cobalt compounds that will enhance the emittance without fluxing the glass.

By combining refractory high emittance additives with the low expansion foam, a refractory low expansion material that will eliminate two major design constraints on CPI materials might be developed.

Finally, complete characterization of, and scale-up procedures for, the new material should be developed as with CPI-12 and CPI-8.

C. Shuttle Simulated Environmental Testing

As our CPI development proceeded under the present contract, it became quite clear that there are no present facilities for properly testing the material in an environment that closely simulates the shuttle re-entry. Recently, we have carried out an extensive survey of facilities across the country that might conceivably be used to this end. At the same time, we have considered how the Grumman in-house arc jet might be modified to simulate more closely the shuttle re-entry environment. By operating the arc jet in air (rather than in vacuum), allowing the CPI test specimen to enter the jet quite far downstream, and then carefully programming 1) the movement of the test specimen toward the nozzle and 2) the energy of the stream, it appears from preliminary calculations that we can match re-entry heating conditions quite closely.

Aerotherm Corporation, which ran the arc jet tests on the CPI material, has three more approaches for improving the simulation while using an arc jet. These are:

- Arc heater operation at similar minimum conditions as achieved in this program, but with the addition of cold gas downstream of the arc heater to lower the test stream enthalpy and model heat flux.

- Auxiliary radiation heat source to bring the sample up to the temperature of the minimum arc heater operating condition.

- Perform the tests in a wedge configuration for which a much lower initial flux level can be achieved.

In the first technique, flux levels as low as about 2.5 Btu/ft^2-sec, yielding a surface temperature rise to about 1000°F in 1 to 1.5 minutes, can be achieved. The second technique can be implemented by employing an auxiliary radiation heat source that provides a flux capability from zero on up. The third technique of employing a wedge test configuration provides minimum flux levels of about 1 Btu/ft^2-sec, which yields a surface temperature rise to about 750°F in 1.5 to 2 minutes.

Any one or all of these modifications to arc jet testing should be pursued to develop a better shuttle simulated environment test.

APPENDIX A

RADIANT HEAT LAMP RE-ENTRY THERMAL SCREENING TESTS

Test Setup

To simulate re-entry temperatures, a quartz lamp array was assembled that is capable of sustained high temperature operation. This array provides the 1500 K-temperature-time profile shown in Figs. 31 and 32. The heating array consisted of a series of six high density radiant heater modules. Each module is designed to accommodate six 3200w quartz lamps side by side. The module reflector and body is water-cooled and the lamps and end seals are air-cooled to prolong their useful life. A clear quartz window encloses the lamps to prevent the test panel surface from being convection-cooled. The six lamp modules are assembled side by side to give an effective heated area of 40 cm x 40 cm. Since the specimens we have been testing are approximately 10 cm x 10 cm, only one-half of the array was used. This setup is shown in Figs. 61 and 62.

The quartz array was powered by a Thermac-A power supply and the time temperature profile was programmed on the Thermac data track that took the input from the thermocouple on the front face and automatically followed preprogrammed time temperature profile.

The test specimen is placed on 5.0 cm of microquartz insulation and insulation is built up around the sides of the specimen. Below the insulation is a 0.26 cm-thick titanium plate with 1.25 cm insulation behind it. This acts as a heat sink that represents interior vehicle heat losses. This assembly is centered under the quartz array as shown in Fig. 63. Typical instrumented samples are shown in Figs. 64 and 65.

Error

In the initial stages of the test program, thermocouples were installed using astroceram. Analysis of test results showed a possible error of approximately 366 K. Therefore, the present method of thermocouple installation evolved. Thermocouples are installed in a small groove made in the specimen. The groove is then covered over using a mixture of the powder from the specimen and a silica binder so that the surface thermal properties are uniform. Test results of surface temperatures are lower than analytical results due to thermocouple installation. The surface thermocouples are slightly below the surface.

APPENDIX B

DIFFERENTIAL THERMAL ANALYSIS AND CALORIMETRIC MEASUREMENTS

The differential thermal analysis (DTA) and differential scanning calorimetric (DSC) measurements were made on the DuPont 900 Thermal Analysis System, using the high temperature (1873 K) DTA module and the standard DSC cell (773 K). The high temperature DTA cell consists of a base assembly, furnace and furnace tube, sample-reference thermocouple assembly, and sample cups. The ceramic part and thermocouple setup is shown in Fig. 58a. The furnace elements are a platinum, 5 percent rhodium, alloy. The control thermocouple is a platinum-platinum 13 percent rhodium, as are the reference and sample thermocouples. The reference material was alumina, and the heating rate was 15 K per minute.

The DSC cell (Fig. 58b) is unique in that it makes use of a constantan disk as the primary means of heat transfer to the sample and reference positions. As one element of the temperature measuring thermoelectric junctions, the cell temperature is controlled by using a silver heating block, a resistive wound heater, and a closely coupled Chromel-Alumel control thermocouple. The block temperature is monitored by the control thermocouple and the appropriate amount of power is supplied to the heater by the programmer. Heat from the block then flows radially through the constantan disk toward the sample and reference platforms.

The temperature at the sample and reference platforms is monitored by the chromel-constantan thermocouple formed by the junction of the constantan disk with a chromel wire at each platform position. The difference signal between these two thermocouple junctions is monitored on the y axis of the x-y recorder. The sample temperature is recorded on the x axis.

The heat capacity (C_p) at temperature T can be calculated with the following formula:

$$(C_p)_T \frac{\text{(millijoules)}}{\text{mg - K}} = \frac{(\Delta T_x)E_T}{Ma}$$

where

$(C_p)_T$ = heat capacity at temperature T

ΔT_x = absolute differential temperature for sample (K)

E_T = calibration coefficient at temperature T (mjoules / K-min)

M = sample mass (mg)

a = heating rate (K/min)

For these measurements the CPI was run against an empty pan at a heating rate of 10 K/minute.

APPENDIX C

TOTAL NORMAL EMITTANCE MEASUREMENT

Total normal emittance in the temperature range of 755-1530 K was measured with a universal high temperature emissometer (Ref. 26). The hollow cylinder specimen is held coaxially inside the isothermal section of a resistance-heated metal tube. This tube is inserted between the two water-cooled high current electrodes; this provides for furnace heating of the sample.

A schematic of the cross section through the rotating specimen furnace is shown in Fig. 41, and the entire emissometer is shown in Fig. 42. The radiation detector views the specimen through a water-cooled viewing-port, extending almost to the specimen surface, through a small opening in the furnace wall.

Two kinds of measurements are made:

1) Below 1366 K. The hollow cylinder-shaped specimen is cut in such a way that blackbody radiation, from the interior of the sample (opening "B" exposed), passes through the viewing-port to the detector for a certain angular position of the specimen, while at the other position (point "A" exposed), radiation from the specimen surface passes through the viewing-port to the detector.

2) The specimen rotates at high speed, and the radiant flux from the specimen surface is measured by the radiometer that is calibrated under similar conditions for blackbody radiation.

The radiometer is a Honeywell miniature radiomatic thermopile detector that has 10 iron-constantan elements and is equipped with a calcium-fluoride lens that passes energy between 0.2 and 9.6 micrometers. The furnace is made of tantalum tubing 3.18 cm o.d. by 30 cm long by 0.03 x 36 cm thick. The specimen is approximately 2.8 cm o.d. by 1.9 cm i.d., by 1.9 cm long. It is inserted between the two disks of a tantalum rotary holder. The efficiency of the blackbody sample cavity was calculated to be better than 0.98.

In both methods, the radiometer is calibrated by reading the total energy radiated from the sample cavity at the temperature shown by the inner surface thermocouple (at point "C"). In the first method, the temperature of the specimen surface is measured by the thermocouple at point "A." In the second method, no thermocouples are attached on the sample surface and the temperature is measured by a two-color pyrometer. Also, a thermocouple probe at point "D" reads the sample cavity temperature.

The total normal emittance is determined from

$$\epsilon_N = \frac{V_S}{V_B}$$

where

V_S = radiometer output signal when viewing the sample surface at temperature T_S

V_B = radiometer output signal from the blackbody calibration curve at temperature T_S

A maximum possible value of the experimental error was evaluated to be ± 7 percent.

APPENDIX D

THERMAL CONDUCTIVITY MEASUREMENT

The system used to measure the thermal conductivity is based on a radial heat flow technique, using a hollow cylindrical sample, with resistance-heated metal heating elements. With this technique,[†] the sample is held vertically (see Fig. 43) between two concentric thin metal tubes and heat energy produced by resistance heating of the inner tube is conducted in a radial-outward direction through the sample, the outer tube being resistance-heated to a lower temperature than that of the inner tube. At steady state, an axially isothermal section is established at the mid-length for each metal tube and sample. Within that section, the longitudinal heat flow is insignificant in relation to the radial heat flow. Thus, the thermal conductivity is determined from measurements of the electric current and voltage drop across an isothermal length at the center portion of the inner tube and the temperature measurement at two known radial distances in the center cross section of the sample.

For the test of sintered cenosphere material, up to 1500 K, the inner tube is of 304 stainless steel, 6.24 cm o.d. by 57.3 cm long by 4.04×10^{-4}m thick. The outer tube is of tantalum, 2.54 cm o.d. by 30 cm long by 0.02×8 cm thick.

The sample consists of a 2.54 cm long hollow cylinder having a 0.6×25 cm i.d. and 2.28 cm o.d., supported by two 14 cm long end pieces of the same inner and outer diameters bonded to the center piece.

The equation used to determine the thermal conductivity from the measured values is

$$K_I = \frac{EI}{(T_1 - T_2)} \ell n \frac{(R_2/R_1)}{2\pi L}$$

at the average temperature $T_{avg} = (T_1 + T_2)/2$ where

E = voltage drop across a distance L in the inner tube

I = current in the inner tube

T_1 and T_2 = the sample temperature at the radial distances R_1 and R_2, respectively

A maximum possible value of the experimental error was evaluated to be ± 6 percent.

[†] Details of this new system will soon be published.

APPENDIX E

MECHANICAL PROPERTY MEASUREMENTS

Figures 44-57 illustrate the equipment, fixtures, and test samples used in this investigation. Each test is described in detail below.

Single Center Point Loading

The simplest type of loading and moment distribution for bend test employs single, center point loading as shown in Fig. 44a. The specimen consists of a straight prismatic beam having an overall length of 15 cm with a nominal thickness and width of 0.63 cm and 1.25 cm, respectively (see Fig. 44b).

The test specimens were individually installed in a universal testing machine and supported as a simple center loaded beam having a span-to-depth ratio of 16:1. Each specimen was flexurally loaded at a constant crosshead rate of 5.08×10^{-2} cm per minute until ultimate failure occurred. Concurrent with load application, specimen deflection, at the midpoint of the span, was autographically recorded by means of a deflectometer-recorder system.

Calculations

The ultimate flexural strength (modulus of rupture) is

$$F_{b_{(ult)}} = \frac{3PL}{2bt^2} (N/m^2)$$

and the flexural modulus of elasticity is

$$E_b = \frac{L^3 \Delta P/\Delta y}{4bt^3} (N/m^2)$$

where

P = total applied load (newtons)

L = test span (meters)

b = measured width of specimen (meters)

t = measured thickness of specimen (meters)

$\Delta P/\Delta y$ = slope of the initial portion of load-deflection curve (newtons/meter)

The major areas of error are:

- localized compression under loading points
- friction forces developed under reaction points
- parallelism of the loading nose and supports with respect to the axis of the specimen

Quarter Point Loading

The quarter point bending test provides a constant maximum moment over a greater length of specimen in comparison to single center point loading. Since a constant stress is applied to a greater portion of the specimen, the procedure increases the statistical probability of failure occurring in accordance with the weakest link theory.

Specimen configuration was similar to that used in the single center point loading test except the over-all length was increased to 20 cm to accommodate the additional loading point (Figs. 45a and b).

The submitted specimens were individually installed in a universal testing machine and supported as a simple beam (15 cm primary span) having a 3.8 cm moment arm. Each specimen was loaded at a constant rate of 7.68 x 10^{-2}cm per minute until failure occurred. Concurrent with load application, specimen deflection at the midpoint of the span was autographically recorded.

Calculations

The ultimate flexural strength is

$$F_b = \frac{3Pa}{bt^2} (N/m^2)$$

and the flexural modulus of elasticity is

$$E_b = \frac{a\Delta P/\Delta y}{4bt^3} (3L^2 - 4a^2) (N/m^2)$$

where

P = total applied load (newtons)
L = primary test span (meters)
b = measured width of specimen (meters)
t = measured thickness of specimen (meters)
$\Delta P/\Delta y$ = slope of the initial portion of load-deflection curve moment arm (meters)

The major areas of error are:

- localized compression at loading points
- unequal load distribution
- failure mode occurring under loading point, due to brittle nature of material

Diametral Compression of a Solid Cylinder

The diametral compression procedure for determining the tensile properties of a ceramic was selected because of its inherent geometric simplicity and the elimination of axial misalignment that is attendant with standard in-line tension tests. This test utilizes the tensile stress incurred in a solid cylinder when subjected to a diametral compressive load (Fig. 46a). The tensile stresses are developed by the application of a vertical compressive force on the specimen, which results in a wedging force component in the horizontal direction.

Each specimen was machined into a disk with a nominal thickness of 1.25 cm and a diameter of 3.24 cm (Fig. 45b). The submitted specimens were installed in a universal testing machine and were subjected to edgewise compressive loading. Each specimen was loaded between two flat and parallel platens. To avoid high shear stresses and to ensure more uniform load distribution, brass pads (5×10^{-3}cm thick) were placed under the points of load introduction. Although not herein determined, Young's modulus and Poisson's ratio can be ascertained by centrally bonding strain gauges along the principal longitudinal and transverse axes.

Calculations

The ultimate tensile strength is

$$\sigma_{max} = \frac{2P}{\pi Dt}(N/m^2)$$

Poisson's ratio is

$$\mu = \frac{3\epsilon_x + \epsilon_y}{\epsilon_x + 3\epsilon_y} = \frac{3 + \epsilon_y/\epsilon_x}{1 + 3\epsilon_y/\epsilon_x}$$

and the tensile modulus of elasticity is

$$E_T = \frac{2}{\pi Dt}\left(\frac{P}{\epsilon_x}\right)(1 + 3\mu) = -\frac{2}{\pi Dt}\left(\frac{P}{\epsilon_y}\right)(3 + \mu)$$

where

P = total applied load (newtons)
D = specimen diameter (meters)
t = specimen thickness (meters)
ϵ_x = strain normal to loaded diameter (tensile)
ϵ_y = strain along loaded diameter
μ = Poisson's ratio
(P/ϵ_x) and (P/ϵ_y) = slope of load versus strain curve

The major areas of error are:

- specimens must be ground smooth and parallel to ensure proper modes of failure
- load pad material and thickness are critical for proper load distribution and can only be determined by experimentation
- only purely tensile fracture modes are acceptable

Edgewise Compression Specimen

Each specimen was cut and machine-ground into a uniform bar of rectangular cross section, having square flat and parallel ($\pm 1.27 \times 10^{-3}$ cm) ends, free of localized defects. The specimens had a nominal thickness and width of 0.6 x 25 cm and 1.6 cm respectively, with an over-all length of 6.7 cm (Fig. 47).

To avoid premature buckling at low stress levels, the sides of each specimen were laterally supported with side plates, incorporating friction and reducing needle bearing.

All the specimens were edgewise compression loaded in a universal testing machine, at a constant crosshead rate of 5×10^{-4} m/minute. Concurrent with load application, longitudinal specimen strain was autographically recorded using a compressometer centrally located within the test section.

Calculations

The ultimate compression strength is

$$F_c = \frac{P}{bt}(\mathrm{N/m^2})$$

and the compression modulus of elasticity is

$$E_c = \frac{\Delta P/\Delta\epsilon}{bt}(\mathrm{N/m^2})$$

where

P = load (newtons)

b = measured width (meters)

t = measured thickness (meters)

$\Delta P/\Delta\epsilon$ = initial slope of load-strain curve

The major areas of error are:

- nonaxial loading of specimen
- premature failures occurring from buckling and local brooming
- specimen fabrication — each specimen must be smooth, flat and parallel with 1.27×10^{-3} cm

APPENDIX F

PLASMA ARC JET TESTS

The two specimens that were arc jet tested were 180-degree circular sections, 1 cm-thick, with an outer radius of 5.4 cm and an inner radius of 1.4 cm. Each specimen was machined by Aerotherm from a Grumman-supplied 7.6 cm x 13 cm x 0.95 cm-thick slab. Figure 66 shows the machined specimen. Figure 67 shows the model configuration in which the specimens were mounted for test. Each specimen was backed up to a 1.9 cm-thick Silfrax insulator of the same diameter (11 cm) and held peripherally by 12 stainless steel pins through the copper retaining ring. The retaining ring was mounted to a water-cooled copper ring that also provided a back wall for the Silfrax insulator. A Gardon-type calorimeter was mounted on the model centerline in a thick wall copper support ring with outside diameter of 2.5 cm. The support ring also contained a 0.16 cm-diameter pressure tap (Fig. 67). Six Aerotherm-built Platinel spring-loaded thermocouples provided the back wall temperature response for the CPI specimens. The thermocouples utilized 1.27×10^{-2}cm-diameter wires through 1.59×10^{-1}cm-diameter two-hole alumina ceramic tubes. The assembly provided a 11 cm-diameter flat face model with 0.32 cm-edge radius for exposure to stagnation point heating in an 20cm-supersonic stream as shown in Fig. 68.

The model was located at a distance of half the exit diameter from the nozzle exit (Fig. 69). The 20cm-nozzle exit diameter provided a test stream Mach number of about 5.0. The model was inserted into the test stream with a pneumatically actuated sting mechanism.

The hyperthermal test stream was generated by the Aerotherm 1-megawatt constrictor arc heater shown schematically in Fig. 69. The configuration shown is especially modified to achieve stable low power operation at stagnation pressures of less than about 0.010 atmosphere as required for the test program. In the arc unit, the energy is added to the primary test gas via a steady electric arc discharge, the arc striking from the tungsten cathode to the downstream diverging copper anode. The primary test gas was high purity nitrogen and was introduced at the downstream end of the cathode module. The secondary gas was high purity oxygen, in the proper amount to yield the composition of air, and was introduced in the plenum and mixing chamber. The arc heater and associated hardware were water-cooled with high pressure deionized water. Power was supplied by a 1-megawatt saturable reactor controlled, d.c. rectifier.

The arc heater, plenum, and nozzle assembly were mounted on the vacuum test chamber to which the nozzle exhausted. This chamber also contained the model sting mechanisms and other necessary support equipment. The vacuum chamber pressure during test was about 0.3 mm Hg for the 20 cm nozzle, which closely matched the nozzle exit pressure. The continuous vacuum pumping capability was provided by all stages of a five-stage steam ejector vacuum pumping system.

A 11 cm-body diameter water-cooled calibration model with six Gardon-type steady state calorimeters and six pressure taps was used to define base line test conditions to which the CPI specimens were exposed. Figure 70 shows the calibration model. Pressure measurements on taps 1 and 2 (Fig. 70) and measurements on all six calorimeters on the calibration model were made at either the minimum or the maximum test condition just prior to initiation of each cyclic model insertion. Three pyrometers, an Infrared Industries TD-9CH and TD-7B, and a Thermogage miniature pyrometer, were used to establish and verify the required 1477 K surface temperature.

The measurements made to characterize the test conditions and the material response were:

- Test conditions
    - Heat flux (centerline) enthalpy
    - Energy balance (bulk) enthalpy
    - Stagnation pressure
    - Stagnation point total heat flux
- Material response
    - Surface temperature history
    - Backwall temperature history
    - Surface recession
    - Mass loss
    - Diameter change
    - Pre- and post-test color slides

Heat flux enthalpy was determined from centerline measurements of heat flux and stagnation pressure through the equation

$$h_{hf} = 23.8 \frac{q_c \sqrt{R_{eff}}}{\sqrt{p_s}}$$

where

h_{hf} = heat flux enthalpy (Btu/lb)

q = cold wall calorimeter heat flux (Btu/ft^2-sec)

p_s = stagnation pressure (atm)

R_{eff} = effective calorimeter nose radius (ft)

Reference 30 discusses the basis for using this equation. Since this centerline enthalpy is that seen by the test model, it was the baseline enthalpy for defining the test conditions

Energy balance enthalpy was defined by an energy balance on the arc heater, including the plenum chamber and nozzle section in which

$$h_{eb} = \frac{\text{Power In} - \text{Cooling Water Losses}}{\text{Total Gas Flow Rate}}$$

$$= \frac{0.948 \times 10^{-3}\, EI - \dot{m}_c \Delta T_c}{\dot{m}}$$

Voltage E and current I were recorded every 30 seconds on a Vidar 5403/643 Digital Data Acquisition System (D-DAS); panel meter indications were observed as a check. Water flow rate was measured with a sharp-edge orifice every 30 seconds during each test cycle. The temperature rise, ΔT_c, of the cooling water was measured every 30 seconds with a differential thermopile.

The total gas flow rate, $\dot{m}$, is the sum of the nitrogen and oxygen flow rates and was measured with precision bore rotameters. The float positions were monitored continuously through each test.

The static pressures at taps 1 and 2 on the calibration model (see Fig. 70) were measured with variable reluctance differential pressure transducers, the outputs of which were recorded on the D-DAS during each insertion. The static pressure on the model (see Fig. 68) was similarly measured every 30 seconds. Test chamber pressure was measured with a thermocouple gauge and monitored continuously during each test cycle.

The stagnation point heat flux and the heat flux at five other radial stations for the calibration model was measured with six Gardon-type steady state calorimeters, the outputs of which were recorded on the D-DAS during each insertion. The stagnation point heat flux on the model was similarly measured every 30 seconds.

Three optical pyrometers were used to measure surface temperature:

- Primary: Infrared Industries TD-9CH sensing at 0.8 microns. View through quartz window with output adjusted for the transmissivity of quartz (0.89 for the above wavelength). Adjustable for surface emissivity.
- Secondary: Infrared Industries TD-7B sensing in the range 1.7-2.7 microns. View same as primary pyrometer. Adjustable for surface emissivity.
- Secondary: Thermogage miniature pyrometer sensing at a peak of 0.9 microns. Surface emissivity corrected in data reduction.

The reference pyrometer (TD-9CH) was mounted on an indexing mechanism that shifted the optical head in a circular pattern to one of six points on the model face in sequence every 1 minute. Each view point was opposite a Platinel spring-loaded thermocouple and at the same radius of 1 11/32 inch. During test, the TD-9CH pyrometer output was adjusted for the emittance of the 8 wt. % cobalt oxide CPI specimen where $\epsilon = 0.75$. In the reduction of the data to temperature, surface temperature measurements on the 12 wt. % cobalt oxide CPI specimen were corrected to $\epsilon = 0.80$.

The Thermogage miniature and the TD-7B backup pyrometers measured the 12 wt. % cobalt oxide CPI specimen temperature at one point on the surface for all 10 cycles. Their outputs were adjusted for $\epsilon = 0.80$. The outputs of the Platinel spring-loaded backwall thermocouples were recorded every 30 seconds on the D-DAS through each cyclic test. Surface recession and radius change measurements were made with a 1-inch micrometer and a 12-inch vernier caliper, respectively. Mass loss was measured with a Mettler Model H20 semimicro analytic balance. Pre- and post-test 35 mm color slides were taken of the exposed surface of each model.

APPENDIX G

ULTRASONIC ATTACHMENT METHODS

Description of Apparatus

A low density heat resistant ceramic, an insulation pad, and a titanium honeycomb panel were successfully fastened together with ultrasonic equipment (see Fig. 35). Currently, ultrasonics is the only technique that exists to fasten together this type of heat shield configuration.

An experimental 6.26 cm diameter ultrasonic transducer/Horn assembly (Fig. 60a and b), vibrating at 20 kHZ, with a peak to peak amplitude of approximately 1.52×10^{-3} cm and a static force of approximately 280 Newtons (applied to the honeycomb/ceramic structures) was used to sink the titanium honeycomb webbing through the insulation blanket and into the ceramic to a depth of 0.3 - 0.4 cm. A good mechanical lock was obtained between the embedded honeycomb webbing and the ceramic. Assemblies up to approximately 10 cm square have been assembled with the available experimental equipment.

A 15 cm x 15 cm square ultrasonic horn is being designed and fabricated to assemble heat shield structures up to 15 cm square.

Ultrasonic Principle

Figure 59 mechanically illustrates how a simplified sandwich-type transducer operates. A disk of piezoelectric material of high electromechanical conversion efficiency is sandwiched between two masses of metal. The whole assembly is resonant at some frequency, F_o, or in acoustical terms equal to a half wavelength. The action of this type transducer can be explained by the use of its lumped mass approximation. The two coupled wheels with cranks connected to the two springs represent the piezoelectric disk that receives electrical energy and converts it to mechanical motion. The springs, with their masses, represent the metal parts of the transducer. Each spring and its mass has a certain natural period of oscillation that determines the natural resonant vibration frequency of the transducer. When the reciprocating action of the cranks occurs at the natural resonant frequency of the springs and masses, the amplitude of excursion of the two masses about their mid-positions is largest. The amplitude of oscillation of the two masses at resonance would, in fact, be constantly increasing if there were no friction in the system. Frictional resistance to the motion of the two masses is indicated by the presence of the two friction channels in which the masses move.

APPENDIX H

DIELECTRIC PROPERTIES OF CPI

To assess the potential of CPI materials for radome applications for the Space Shuttle, a series of measurements of the dielectric constant and dielectric loss in CPI were undertaken at NASA/Langley Research Center. Samples were provided by Grumman Aerospace Corporation.

Sample CPI-55 contained no additives and had a density of 8.8×10^2 kg/m^3 (55 pcf). The measured values at room temperature were

dielectric constant	2.44	at	9.55 GHz
	2.41	at	6.40 GHz
loss tangent	0.0108	at	9.55 GHz
	0.0130	at	6.40 GHz

Sample CPI-35 contained 12 wt. % CoO additive and had a density of 5.6×10^2 kg/m^3 (35 pcf). The measured values were

dielectric constant	1.77	at	11.2 GHz
	1.77	at	7.46 GHz
loss tangent	0.0080	at	11.2 GHz
	0.0086	at	7.46 GHz

At 10 GHz and 1273 K, the dielectric constant was 2.16, and the dielectric loss was 0.04.

These test results showed that the cobalt oxide additive apparently did not degrade the material's dielectric properties. The lower dielectric constant and loss tangent values for CPI-35 are most likely due to the material's lower density. These results indicate that CPI has potential radome applications for the Space Shuttle. This can be seen by comparison with a typical high temperature radome material (i.e., polyimide-glass fabric laminate that has a dielectric constant of 4.2 and a loss tangent of 0.015).

REFERENCES

1. Stanislaw, T. S.: Development of Beta-Spodumene Closed Pore Insulation (CPI). RM-517, Research Department, Grumman Aerospace Corporation, 1971.

2. Raask, E.: Cenospheres in Pulverized Fuel Ash. Jour. Inst. Fuel, Vol. 9, 1968.

3. Levin, E.; Robbins, C.; and McMurdie, H.: Phase Diagrams for Ceramists, American Ceramic Society, Columbus, Ohio, 1964.

4. Bache, H. H.: Model for the Strength of Brittle Materials Built of Particle Joined at Points of Contact. J. Am. Cer. Soc., Vol. 53, 1970, p. 654.

5. Hasselman, D. P. H.; and Fulrath, R. M.: Micromechanical Stress Concentrations in Two Phase Brittle Matrix Ceramic Composites. ibid., Vol. 50, 1967, p. 399.

6. Kingery, W. D.: Introduction to Ceramics. J. Wiley and Sons, New York, 1960.

7. Wachtman, J. B., Jr.: Mechanical and Thermal Properties of Ceramics. NBS Special Publication 303, 1968.

8. Brown, S. D. et al.: A Strength-Porosity Relation Involving Different Pore Geometry and Orientation. J. Am. Cer. Soc., Vol. 47, 1964, p. 320.

9. Davidge, R. W.; and Tappin, G.: Internal Strain Energy and the Strength of Brittle Materials. J. Mat. Sci., Vol. 3, 1968, p. 297.

10. Schwartz, B.: Thermal Stress Failure of Pure Refractory Oxides. J. Am. Cer. Soc., Vol. 35, 1952, p. 325.

11. Hasselman, D. P. H.: Thermal Stress Resistance Parameter for Brittle Refractory Ceramics: A Compendium. Cer. Bull., Vol. 49, 1970.

12. Kingery, W. D.: Factors Affecting the Thermal Stress Resistance of Ceramic Materials. J. Am. Cer. Soc., Vol. 38, 1955, p. 3.

13. Buessem, W. R.: Thermal Shock Testing. ibid., Vol. 38, 1955, p. 15.

14. Manson, S. S.; and Smith, R. W.: Theory of the Thermal Shock Resistance of Brittle Materials Based on Weibull's Statistical Theory of Strength. ibid., Vol. 38, 1955, p. 18.

15. Coble, R. L.: Effect of Porosity on Thermal Stress Fracture. ibid., Vol. 38, 1955, p. 33.

16. Baroody, E. M. et al.: Effect of Shape on Thermal Fracture. ibid, Vol. 38, 1955, p. 38.

17. Hasselman, D. P. H.: Unified Theory of Thermal Shock Fracture Initiation and Crack Propagation in Brittle Ceramics. ibid., Vol. 52, 1969, p. 600.

18. Hasselman, D. P. H.: Thermal Shock by Radiation Heating. J. Am. Cer. Soc., Vol. 46, 1963, p. 229.

19. Hasselman, D. P. H.: Theory of Thermal Stress Resistance of Semitransparent Ceramics under Radiation Heating. ibid., Vol. 49, 1966, p. 103.

20. Kingery, W. D.: Factors Affecting the Thermal Shock Resistance of Ceramic Materials. ibid., Vol. 38, 1955, p. 3.

21. Coble, R. L.; and Kingery, W. D.: Effect of Porosity on Thermal Stress Fracture. ibid., Vol. 38, 1955, p. 33.

22. Hasselman, D. P. H.: Elastic Energy at Fracture and Surface Energy as Design Criteria for Thermal Shock. ibid., Vol. 46, 1963, p. 535.

23. Campbell, I. E.; and Sherwood, E. M.: High Temperature Materials and Technology. John Wiley & Sons, Inc., New York, 1967.

24. Androulakis, J. G.: A Guarded Disk-Type Sample Emissometer. J. Space. and Rockets, Vol. 7, 1970, p. 493.

25. Howells, J.: NASA/Langley Research Center (private communication).

26. Androulakis, J. G.: The Universal High Temperature Emissometer. Grumman Aerospace Corporation Report ADR 04-02-71.2, 1971.

27. Anon.: The Evaluation and Interpretation of the Mechanical Properties of Brittle Materials. Report 68-3, DCIC, AFML-TR-67-316, April 1968.

28. Anon.: Test for Compressive Properties of Rigid Plastics. Standards D695-63T, ASTM, November 1963.

29. Anon.: Flexural Properties of Plastics. Standards D790-66, ASTM, May 1966.

30. Schaefer, J. W.; and Flood, D. T.: High-Enthalpy Re-entry Simulation for Planetary Return Missions. J. Space and Rockets, September 1968.

31. Pickett, G.: Equations for Computing Elastic Constants from Flexural and Torsional Resonant Frequencies of Vibrations of Prisms and Cylinders. Proc. ASTM, Vol. 45, 1945, p. 846.

32. Reichman, J.: Radiation Heat Transfer in Ceramic Re-entry Heat Shields. RE-419J, Research Department, Grumman Aerospace Corporation, 1972.

Table 1

REQUIREMENTS OF EXTERNAL INSULATION MATERIAL

- Low Density
- *Low Thermal Conductivity*
- Multiple Re-use Under Shuttle Launch & Re-entry Cycling
- Thermal, Chemical & Mechanical Stability at Hi Temps
- Good Thermal Overshoot for Off-Nominal Trajectories
- High Emittance Surface
- Resistance to Water Pickup During Launch & Ground Ops (Rain & Moisture Humidity Cycling)
- Resistance to High Velocity Gas Erosion
- Good Handling Characteristics
- Resistance to Vibration & Acoustic Noise
- Resistance to Aero & g-loads
- Sufficient Mechanical Strength for Direct Attachment to Primary Structure
- Ease of NDT Inspection, Removal & Replacement
- Ease of Scale-up & Fabrication
- Design Flexibility
- Good Reliability & Predictability

Table 2

CHEMICAL ANALYSIS OF CENOSPHERES (WT %)

Constituent	English	Domestic
Al_2O_3	31.97	33.25
SiO_2	60.75	61.60
Fe_2O_3	4.18	3.16
K_2O	1.91	1.44
Na_2O	0.81	0.59

Table 3

EFFECT OF FIRING TIME AND TEMPERATURE ON WATER ABSORPTION IN SELF-BONDED CENOSPHERE BODIES

	English Cenospheres					Domestic Cenospheres		
Specimen #	1	2	3	4	5	1	2	3
Heat Treatment	as-received	1400 K 16 hr	1560 K 16 hr	1590 K 6 hr	1700 K 2 hr	as-received	1400 K 16 hr	1700 K 2 hr
Density (kg/m^3)	336	472	624	648	800	472	560	1120
Wt% Water Absorption		67	15.3	15	1		67	1

Table 4

TEMPERATURE DEPENDENCE OF THE THERMAL CONDUCTIVITY OF A SELF-BONDED CENOSPHERE BODY USING GUARDED HOT PLATE METHOD (DENSITY = 430 kg/m^3)

T (K)	530	810	1090
k (W/m-K)	0.13	0.14	0.17
k (BTU/hr.-ft-°F)	0.078	0.085	0.10

Table 5
PHYSICAL DIMENSIONS AND PROPERTIES OF SINTERED CPI TILES

Specimen Description (See Footnote)	Physical Dimension centimeters (inches)	Density kg/m^3 (pcf)	Water Abs. Wt%
WV-0	10 x 15 x 2 (4 x 6 x 1)	610 (38)	1%
E-12	10 x 15 x 2 (4 x 6 x 1)	603 (37.6)	1%
LWE-12	7.6 x 4 (PLUG) (3 x 2)	615 (38.5)	1%
LWE-0	10 x 15 x 2 (4 x 6 x 1)	601 (37.5)	1%
LWE-0	10 x 15 x 2 (4 x 6 x 1)	610 (38.0)	1%
LWE-0	7.6 x 4 (3 x 2)	545 (34)	1%
WV-12	10 x 15 x 2 (4 x 6 x 1)	577 (36)	1%
WV-12	7.6 x 4 (3 x 2)	610 (38)	1%
E-12	7.6 x 4 (3 x 2)	594 (37)	1%
E-12	10 x 15 x 2 (4 x 6 x 1)	560 (35)	1%
E-12	10 x 15 x 2 (4 x 6 x 1)	560 (35)	1%
WV-12	20 x 21 x 2 (8 x 8 x 1)	705 (44)	1%
E-12	10 x 15 x 2 (4 x 6 x 1)	530 (33)	10%
E-12	10 x 15 x 2 (4 x 6 x 1)	513 (32)	10%
E-4	10 x 15 x 2 (4 x 6 x 1)	577 (36)	1%
E-12	10 x 15 x 2	625 (39)	1%
WV-12	10 x 15 x 2 (4 x 6 x 1)	577 (36)	1%

E = English cenospheres
LWE = low density English cenospheres
WV = West Virginia Cenospheres
0 = no cobalt additives
4 = 4 wt % cobalt oxide additive
12 = 12 wt% cobalt oxide additives

Table 6

THERMAL CONDUCTIVITY OF PURE SINTERED CENOSPHERES
FIRED TO 1723 K (DENSITY = 608 kg/m^3)

T (°F)	k (BTU/ft-hr-°F)	k (W/m - K)	T(K)
710	0.174	0.301	650
1023	0.180	0.319	822
1263	0.194	0.336	956
1438	0.207	0.358	1055
1606	0.226	0.391	1146
1823	0.252	0.436	1267
1994	0.272	0.470	1363

Table 7

THERMAL CONDUCTIVITY OF SINTERED CENOSPHERES,
WITH FOUR-WEIGHT-PERCENT CoO ADDITIVE, FIRED TO 1477K
(DENSITY = 430 kg/m^3)

T (°F)	k (BTU/ft-hr-°F)	k (W/m - K)	T(K)
1118	0.0945	0.163	873
1248	0.104	0.180	948
1379	0.1167	0.202	1023
1443	0.1210	0.210	1058
1660	0.1301	0.227	1178
1914	0.177	0.306	1318
2086	0.203	0.352	1413

Table 8

THERMAL CONDUCITIVITY OF SINTERED CENOSPHERES WITH TWELVE-WEIGHT-PERCENT CoO ADDITIVE

(DENSITY = 608 kg/m^3)

T (° F)	k (BTU/ft-hr-° F)	k (W/m -K)	T (K)
216	.076	0.132	376
523	.107	0.185	547
875	.154	0.266	743
1133	.555	0.268	883
1258	.170	0.294	953
1399	.180	0.312	1033
1670	.204	0.354	1183
1910	.225	0.390	1318
2096	.234	0.405	1418
2209	.242	0.419	1483

Table 9

TOTAL NORMAL EMITTANCE OF PURE SINTERED CENOSPHERES

(DENSITY = 608kg/m^3)

T(K)	T(°F)	E
733	1040	0.62
1072	1470	0.58
1202	1703	0.52
1300	1880	0.47
1505	2250	0.42

Table 10

TOTAL NORMAL EMITTANCE OF SINTERED CENOSPHERES WITH FOUR-WEIGHT-PERCENT CoO ADDITIVE (DENSITY = 430kg/m^3)

T(K)	T(^{o}F)	E
746	1065	0.75
963	1276	0.74
1000	1525	0.78
1240	1771	0.79
1300	1884	0.79

Table 11

TOTAL NORMAL EMITTANCE OF SINTERED CENOSPHERES WITH TWELVE-WEIGHT-PERCENT CoO ADDITIVE (DENSITY = 592 kg/m^3)

T(K)	T(^{o}F)	E
746	1062	0.85
964	1280	0.87
1223	1744	0.87
1372	2010	0.86

Table 12

THREE POINT BEND STRENGTH AND MODULUS OF CPI WITH TWELVE-WEIGHT-PERCENT CoO ADDITIVE

L/T = 15:1

Specimen	Bend Strength (psi)	Bend Strength (N/m^2)	Bend Modulus psi	Bend Modulus (N/m^2)
1	9.68×10^2	6.66×10^6	1.04×10^6	7.16×10^9
2	7.71	5.31	0.81	5.58
3	8.12	6.60	0.817	5.63
4	7.95	5.48	1.00	6.89
5	8.04	5.54	1.02	7.03
6	8.90	6.13	1.02	7.03
7	8.40	5.78	1.17	8.05
	Avg = 8.54	Avg = 5.89	Avg = 0.98	Avg = 6.76

Table 13

DENSITY COMPARISONS OF FIRED AND UNFIRED CPI TILES

Designation	L (cm)	W (cm)	H (cm)	Unfired Density		Fired Density	
				(kg/m^3)	(pcf)	(kg/m^3)	(pcf)
R-1	20.1	20.4	2.0	410.0	25.6	560.7	35.2
R-3	20.2	20.0	2.1	419.7	26.2	541.3	33.8
R-4	20.1	19.8	2.0	397.3	24.8	549.5	34.3
S-3	20.3	20.0	3.5	402.1	25.1	578.3	36.1
S-4	20.3	19.9	3.6	389.3	24.3	539.8	33.7
S-5	20.4	20.1	3.6	414.9	25.9	559.1	34.9

R = 12% Co 0 Additive

S = 8% Co 0 Additive

Table 14

EXPERIMENTAL AND ASTM X-RAY d-SPACINGS FOR R- AND S-SERIES CPI TILES

ASTM Card # 15-776 Mullite	ASTM Card # 10-458 Cobalt Aluminate	R Series 12% Cobalt	S Series 8% Cobalt
5.39		5.412	5.386
3.428		3.434	3.429
3.390		3.386	3.401
2.886		2.891	2.900
	2.864	2.870	2.860
2.694		2.701	2.630
2.542		2.520	2.535
	2.443	2.430	2.440
2.206		2.195	2.211
2.120		2.124	2.090
	2.026	2.016	2.029
	1.645	1.647	1.640
	1.560	1.551	1.548
	1.432	1.402	1.425

Table 15

WATER ABSORPTION IN SCALED-UP R- AND S-SERIES CPI TILES

Sample	wt. % Water Absorption
R-Series	
R-1	1.59
R-3	1.60
R-4	1.40
S-Series	
S-3	1.07
S-4	1.42
S-5	1.54

Table 16

THERMAL EXPANSION COEFFICIENTS AND SOFTENING POINTS FOR SCALED-UP R- AND S-SERIES CPI TILES

	CPI Without Cobalt	R-1	R-3	R-4	$\bar{R}$	S-3	S-4	S-5	$\bar{S}$
		12% Cobalt				8% Cobalt			
Coefficient of Linear Thermal Expansion (x 10^{-6}/ K)	5.09	5.85	5.74	5.73	5.77	5.48	5.54	5.35	5.45
Softening Point (K)	1333	1183	1178	1193	1184	1253	1248	1263	1254

Table 17

HEAT CAPACITY VERSUS TEMPERATURE OF R- AND S-SERIES CPI TILES (Cal/gm - K)

K	R-1	R-3	R-4	$\bar{R}$	S-3	S-4	S-5	$\bar{S}$
323	.160	.148	.152	.153	.172	.169	.171	.170
373	.165	.153	.159	.159	.176	.173	.179	.176
423	.171	.159	.170	.166	.183	.179	.185	.182
473	.173	.163	.175	.170	.187	.184	.189	.187
523	.178	.169	.180	.175	.192	.189	.191	.191
573	.183	.173	.184	.180	.196	.197	.198	.197
623	.188	.177	.188	.184	.205	.206	.203	.204
673	.188	.181	.187	.185	.204	.214	.200	.206
723	.188	.184	.187	.186	.211	.217	.197	.208

Table 18a

THERMAL CONDUCITVITY VERSUS TEMPERATURE OF R- AND S-SERIES CPI TILES (W/m-K)

	R-1	R-3	R-4	$\overline{R}$	S-3	S-4	S-5	$\overline{S}$
T(K)								
400	.181	.171	.192	.181	-	-	-	-
500	-	-	-	-	-	-	-	-
600	.231	-	-	.231	-	-	.210	.210
700	.288	.299	-	.293	.265	.260	.245	.256
800	.310	.318	.359	.329	.300	.283	.279	.287
900	.350	.330	.379	.353	.324	.311	.305	.313
1000	.360	.352	.368	.360	.351	.332	.318	.337
1100	.368	.365	.385	.372	.362	.345	.328	.345
1200	.379	.375	.387	.380	.370	.361	.347	.360
1300	.382	.385	.390	.385	.384	.378	.363	.375
1400	.395	.390	.402	.395	.415	.392	.372	.393
1500	.401	.395	.413	.403	.430	.408	.382	.406

Table 18b

THERMAL CONDUCTIVITY VERSUS TEMPERATURE OF R AND S SERIES C.P.I. TILES (BTU/Ft °F hr)

T. (^{o}F)	R-1	R-3	R-4	$\bar{R}$	S-3	S-4	S-5	$\bar{S}$
200	.106	.099	.110	.105	-			
400	-	-	-	-	-	-	-	-
600	.133	-	-	.133	-	-	.121	.121
800	.166	.173	-	.169	.153	.150	.141	.147
1000	.179	.183	.207	.190	.173	.163	.161	.165
1200	.202	.190	.219	.204	.187	.179	.176	.181
1400	.208	.203	.212	.208	.202	.191	.183	.194
1600	.212	.211	.222	.215	.209	.199	.189	.199
1800	.219	.216	.223	.219	.213	.208	.200	.208
2000	.220	.222	.225	.222	.221	.218	.209	.216
2200	.228	.225	.232	.228	.239	.226	.215	.227

Table 19a

ROOM TEMPERATURE, FLEXURAL PROPERTIES (SINGLE CENTER POINT LOADING) OF CPI MATERIAL WITH EIGHT-WEIGHT-PERCENT CoO ADDITIVE

Spec. Ident.	Thickness (centimeters)	Width (centimeters)	Failure Load (Newtons)	Ultimate Stress (N/m^2)	Modulus (N/m^2)	Mode of Failure
	GROUP S3					
S3-1	6.50×10^{-1}	15.7	20.6	4.72×10^6	4.55×10^9	Flexure-center
S3-2	6.52	15.7	18.9	4.30	5.03	Flexure-center
S3-5	6.50	15.7	24.5	5.60	4.76	Flexure-off center
S3-6	6.58	15.7	21.8	4.86	4.20	Flexure-off center
			Avg =	4.87	4.61	
	GROUP S4					
S4-1	6.19	15.9	25.4	6.37	6.06	Flexure-center
S4-2	5.17	15.8	24.3	6.14	5.45	Flexure-center
S4-3	6.15	15.9	22.9	5.81	5.65	Flexure-center
S4-5	6.17	15.9	23.4	5.90	5.72	Flexure-off center
S4-6	6.17	15.9	20.9	5.27	5.86	Flexure-center
			Avg =	5.90	5.72	
	GROUP S5					
S5-1	6.15	15.9	19.8	5.00	5.45	Flexure-center
S5-4	6.17	15.9	24.1	6.07	5.79	Flexure-off center
S5-5	6.17	15.9	26.4	6.64	5.79	Flexure-center
			Avg =	5.90	5.66	

Table 19b

ROOM TEMPERATURE, FLEXURAL PROPERTIES (SINGLE, CENTER POINT LOADING) OF C.P.I. MATERIAL WITH 8% COBALT ADDITIVE

Spec. Ident.	Thick. (in.)	Width (in.)	Fail Load (lb.)	Ult. Stress (psi)	Modulus (psi)	Mode of Failure
	GROUP: S3-					
S3-1	.256	.620	4.64	6.85×10^2	$.66 \times 10^6$	Flexure - Center
-2	.257	.620	4.25	6.24	.73	Flexure - Center
-5	.256	.620	5.50	8.12	.69	Flexure - Off Center
-6	.259	.620	4.90	7.05	.61	Flexure - Center
			Avg. -	7.07	.67	
	GROUP: S4-					
S4-1	.244	.625	5.72	9.25	.88	Flexure - Center
-2	.243	.625	5.47	8.90	.79	Flexure - Center
-3	.242	.625	5.15	8.43	.82	Flexure - Center
-5	.243	.625	5.25	8.55	.83	Flexure - Off Center
-6	.243	.625	4.70	7.64	.85	Flexure - Center
			Avg. -	8.55	.83	
	GROUP: S5-					
S5-1	.242	.626	4.45	7.25	.79	Flexure - Center
-4	.243	.626	5.42	8.80	.84	Flexure - Off Center
-5	.243	.626	5.94	9.63	.84	Flexure - Center
			Avg.	8.56	.82	

Table 20a

ROOM TEMPERATURE, FLEXURAL PROPERTIES (SINGLE CENTER POINT LOADING) OF CPI MATERIAL WITH TWELVE-WEIGHT-PERCENT CoO ADDITIVE

Spec Ident.	Thickness (centimeters)	Width (centimeters)	Failure Load (Newtons)	Ultimate Stress (N/m^2)	Modulus (N/m^2)	Mode of Failure
	GROUP R1					
R1-1	7.98×10^{-1}	16.2×10^{-1}	37.1	6.16×10^{6}	7.23×10^{9}	Flexure-center
R1-2	6.86	16.4	22.9	5.09	5.38	Flexure-off center
R1-3	6.83	16.3	24.2	5.45	6.34	Flexure-center
R1-4	6.83	16.7	27.1	5.96	6.62	Flexure-center
R1-5	6.76	16.7	25.8	5.78	6.54	Flexure-center
R1-6	6.88	16.6	26.7	5.80	6.27	Flexure-center
			Avg =	5.72	6.41	
	GROUP R3					
R3-1	6.86	18.2	27.6	5.52	7.51	Flexure-center
R3-2	6.88	18.2	24.0	4.77	5.72	Flexure-off center
R3-3	7.75	18.2	38.3	6.01	8.06	Flexure-center
R3-4	6.81	18.4	27.6	5.54	6.27	Flexure-center
R3-5	6.78	18.2	27.1	5.57	7.44	Flexure-center
R3-6	6.70	18.4	27.1	5.63	5.65	Flexure-off center
			Avg =	5.52	6.78	
	GROUP R4					
R4-1	6.91	15.8	25.8	5.75	7.93	Flexure-center
R4-2	7.08	15.8	26.7	5.79	6.48	Flexure-center
R4-3	6.78	15.8	25.4	5.97	6.76	Flexure-center
R4-4	7.08	15.3	23.6	5.25	6.27	Flexure-center
R4-5	6.83	15.4	25.8	6.13	7.58	Flexure-center
R4-6	6.90	15.1	25.4	6.06	6.62	Flexure-off center
			Avg =	5.79	6.90	

Table 20b

ROOM TEMPERATURE, FLEXURAL PROPERTIES (SINGLE, CENTER-POINT LOADING) OF C.P.I. MATERIAL WITH 12% COBALT ADDITIVE.

Spec. Ident.	Thick. (in.)	Width (in.)	Fail Load (lb.)	Ult. Stress (psi)	Modulus (psi)	Mode of Failure
	GROUP: R1-					
R1-1	.314	.640	8.35	8.93×10^2	1.05×10^6	Flexure - Center
-2	.270	.645	5.15	7.39	.78	Flexure - Off Center
-3	.269	.643	5.45	7.90	.92	Flexure - Center
-4	.269	.657	6.10	8.65	.96	Flexure - Center
-5	.266	.659	5.80	8.39	.95	Flexure - Center
-6	.271	.655	6.00	8.42	.91	Flexure - Center
			Avg. -	8.30	.93	
	GROUP: R3-					
R3-1	.270	.717	6.20	8.00	1.09	Flexure - Center
-2	.271	.718	5.40	6.92	.83	Flexure - Off Center
-3	.305	.716	8.60	8.72	1.17	Flexure - Center
-4	.268	.726	6.20	8.03	.91	Flexure - Center
-5	.267	.715	6.10	8.08	1.08	Flexure - Center
-6	.264	.723	6.10	8.17	.82	Flexure - Off Center
			Avg. -	8.00	.98	
	GROUP: R4-					
R4-1	.274	.624	5.80	8.35	1.15	Flexure - Center
-2	.279	.622	6.00	8.40	.94	Flexure - Center
-3	.267	.623	5.70	8.66	.99	Flexure - Center
-4	.279	.604	5.30	7.61	.91	Flexure - Center
-5	.269	.608	5.80	8.89	1.10	Flexure - Center
-6	.272	.595	5.70	8.79	.96	Flexure - Off Center
			Avg. -	8.40	1.00	

Table 21a

ROOM TEMPERATURE, FLEXURAL PROPERTIES (QUARTER POINT LOADING) OF CPI MATERIAL WITH EIGHT-WEIGHT-PERCENT CoO ADDITIVE

Spec. Ident	Thick (centimeters)	Width (centimeters)	Fail Load (Newtons)	Ult. Stress (N/m^2)	Strain(1) at Failure	Mode at Failure
	GROUP: S3					
S3-1	6.50×10^{-1}	15.8×10^{-1}	2.63×10^{5}	4.52×10^{6}	-	Under Load Point
S3-2	6.53	15.8	2.85	4.85		Under Load Point
S3-3	6.27	15.7	2.67	4.93	7.1×10^{-4}	Under Load Point
				4.77	7.1	
	GROUP: S4					
S4-1	6.20	15.9	3.00	5.61	-	Under Load Point
S4-2	6.17	15.9	2.83	5.32	-	Under Load Point
S4-3	6.15	15.9	2.70	5.15	-	Under Load Point
				5.36	-	
	GROUP: S5					
S5-1	5.15	15.9	2.70	5.12	-	Center
S5-2	6.17	15.9	2.72	5.14	7.0	Under Load Point
				5.13	7.0	

(1) - Strain at Failure Calculated from One Longitudinal Paper Strain Gage, Bond in the Center, Tension Face, of the Specimen.

Table 21b

ROOM TEMPERATURE, FLEXURAL PROPERTIES (QUAR-POINT-LOADING) OF C.P.I. MATERIAL WITH 8% COBALT ADDITIVE.

Spec. Ident.	Thick. (in.)	Width (in.)	Fail Load (lb.)	Ult. Stress (psi)	Strain[1] at Failure	Mode of Failure
	GROUP: S3-					
S3-1	.256	.620	5.90	655	-	Under Load Point
-2	.257	.620	6.40	704	-	Under Load Point
-3	.247	.619	6.00	715	.00071	Under Load Point
			Avg. -	691	.00071	
	GROUP: S4-					
S4-1	.244	.626	6.74	813	-	Under Load Point
-2	.243	.625	6.35	772	-	Under Load Point
-3	.242	.624	6.06	747	-	Under Load Point
			Avg. -	778	-	
	GROUP: S5-					
S5-1	.242	.626	6.06	742	-	Center
-2	.243	.626	6.12	745	.00070	Under Load Point
			Avg. -	744	.00070	

(1) - Strain at failure calculated from one longitudinal paper strain gage, bond in the center, tension face, of the specimen.

Table 22a

ROOM TEMPERATURE, TENSILE PROPERTIES (DIAMETRAL COMPRESSION LOADED) CPI MATERIAL WITH TWELVE-WEIGHT-PERCENT CoO ADDITIVE

Spec Ident	Thick (centimeters)	Diameter (centimeters)	Fail. Load (Newtons)	Ult. Tensile (N/m^2)	Mode of Failure
1	1.26	3.25	2.38×10^5	3.72×10^6	Shear
2	1.43	3.25	2.45	3.37	Tensile-Triple Cleft
3	1.42	3.24	2.58	3.59	Tensile-Triple Cleft
4	1.45	3.25	2.56	3.47	Tensile-Triple Cleft
5	1.42	3.25	2.49	3.44	Tensile-Triple Cleft
6	1.37	3.25	2.45	3.50	Tensile
8	1.43	3.24	2.41	3.30	Tensile-Triple Cleft
9	1.48	3.25	2.63	3.47	Tensile-Triple Cleft
			Avg	3.48	

Table 22b

ROOM TEMPERATURE, TENSILE PROPERTIES (DIAMETRIAL COMPRESSION LOADED) OF C.P.I. MATERIAL WITH 12% COBALT ADDITIVE

Spec. Ident.	Thick. (in.)	Diameter (in.)	Fail Load (lb)	Ult. Tensile Stress (psi)	Mode of Failure
1	.495	1.278	535	539	Shear
2	.561	1.278	550	489	Tensile-Triple Cleft
3	.557	1.275	580	520	Tensile-Triple Cleft
4	.570	1.279	576	503	Tensile-Triple Cleft
5	.559	1.279	560	499	Tensile-Triple Cleft
6	.539	1.280	550	508	Tensile
8	.564	1.277	542	479	Tensile-Triple Cleft
9	.584	1.280	590	503	Tensile-Triple Cleft
			Avg. -	505	

Table 23a

ROOM TEMPERATURE, EDGEWISE COMPRESSION PROPERTIES OF CPI MATERIAL WITH EIGHT-WEIGHT-PERCENT CoO ADDITIVE

Spec. Ident	Width (centimeters)	Width (centimeters)	Fail. Load (Newtons)	Ult. Stress (N/m^2)	Mod. (N/m^2)	Strain at Failure	Mode of Failure
	GROUP S3						
S3-1	6.30 x 10^{-1}	3.91 x 10^{-1}	1.49 x 10^5	1.50 x 10^7	7.51 x 10^9	-	Edge Compression
S3-2	6.30	3.91	1.52	1.53	6.27	-	Catastrophic
S3-3	6.30	3.91	1.65	1.66	8.96	1.75 x 10^{-3}	Edge Compression
S3-4	6.30	3.91	1.50	1.50		-	Edge Compression
S3-5	6.30	3.91	1.10	1.11		-	Catastrophic
S3-6	6.30	3.91	1.34	1.34	8.96	-	Edge Compression
S3-7	6.30	3.91	1.58	1.59	8.27	2.05	Edge Compression
S3-8	6.30	3.91	1.52	1.53		-	Edge Compression
S3-9	6.30	3.91	1.56	1.57	6.76	2.32	Edge Compression
S3-10	6.30	3.91	1.58	1.59	8.27	1.77	Edge Compression
S3-11	6.27	3.89	1.71	1.73	6.00	2.70	Center
S3-12	6.30	3.91	1.77	1.78	6.21	-	Edge Compression
S3-13	6.30	3.91	1.19	1.20		-	Edge Compression
S3-14	6.33	3.91	1.59	1.60	7.58	2.12	Edge Compression
			Avg -	1.52	7.48	2.12	
	GROUP:	S4-					
S4-1	6.33	3.94	2.09	2.09	6.89	3.04	Catastrophic
S4-2	6.33	3.94	1.21	1.21	8.96	-	Center
S4-3	6.30	3.94	1.93	1.92	7.58	2.57	Edge Compression
S4-4	6.22	3.89	1.99	2.01	8.27	-	Edge Compression
S4-5	6.33	3.94	1.60	1.60	7.24	2.15	Edge Compression
S4-6	6.33	3.94	1.82	1.81	6.69	2.72	Edge Compression
S4-7	6.33	3.94	2.07	2.07	8.27	2.46	Catastrophic
S4-8	6.33	3.94	1.81	1.81	6.89	2.64	Catastrophic
S4-9	6.33	3.96	2.14	2.12	7.24	2.87	Edge Compression
S4-10	5.92	3.71	1.68	1.79	7.58	2.36	Edge Compression
S4-11	6.02	3.76	2.01	2.10	7.58	2.77	Edge Compression
S4-12	6.33	3.94	1.94	1.93	6.89	-	Center
S4-13	6.33	3.94	1.98	1.97	7.58	2.63	Edge Compression
S4-14	6.33	3.96	1.90	1.89	7.58	-	Edge Compression
			Avg -	1.88	7.52	2.62	
	GROUP:	S5-					
S5-1	6.33	3.96	1.88	1.86	6.21	-	Center
S5-2	6.33	3.96	1.91	1.90	6.89	2.70	Catastrophic
S5-3	6.33	3.96	1.67	1.66	6.07	2.70	Catastrophic
S5-4	6.33	3.96	1.56	1.54	7.31	-	Edge Compression
S5-5	6.33	3.96	1.16	1.15		-	Edge Compression
S5-6	6.33	3.96	1.49	1.48	7.58	2.02	Edge Compression
S5-7	6.30	3.94	1.78	1.78	6.89	2.62	Center
S5-8	6.30	3.94	1.59	1.59	6.07	2.60	Center
S5-9	6.33	3.96	1.70	1.69	6.27	-	Edge Compression
S5-10	6.35	3.96	1.78	1.77	6.27	2.84	Catastrophic
S5-11	6.33	3.96	2.00	1.99	6.69	3.16	Catastrophic
S5-12	6.33	3.96	1.94	1.93	6.34	3.05	Edge Compression
S5-13	6.30	3.94	1.99	1.99	6.69	2.95	Edge Compression
S5-14	6.33	3.96	1.74	1.72		-	Edge Compression
			Avg -	1.72	6.61	2.74	

Table 23b

ROOM TEMPERATURE EDGEWISE COMPRESSION PROPERTIES OF C.P.I. MATERIAL WITH 8% COBALT ADDITIVE

Spec. Ident.	Thick. (in.)	Width (in)	Fail Load (lb.)	Ult. Stress (psi)	Modulus (psi)	Strain at Failure	Mode of Failure
	GROUP: S3-						
S3-1	.248	.154	335	$2.17\text{x}10^3$	$1.09\text{x}10^6$	-	Edge Compression
-2	.248	.154	342	2.22	.91	-	Catastrophic
-3	.248	.154	370	2.40	1.30	.00175	Edge Compression
-4	.248	.154	336	2.18	-	-	Edge Compression
-5	.248	.154	248	1.61	-	-	Catastrophic
-6	.248	.154	300	1.95	1.30	-	Edge Compression
-7	.248	.154	355	2.30	1.20	.00205	Edge Compression
-8	.248	.154	342	2.22	-	-	Edge Compression
-9	.248	.154	350	2.27	.98	.00232	Edge Compression
-10	.248	.154	354	2.30	1.20	.00177	Edge Compression
-11	.247	.153	384	2.51	.87	.00270	Center
-12	.248	.154	398	2.58	.90	-	Edge Compression
-13	.248	.154	268	1.74	-	-	Edge Compression
-14	.249	.154	358	2.32	1.10	.00212	Edge Compression
			Avg. -	2.20	1.09	.00212	
	GROUP: S4-						
S4-1	.249	.155	470	3.03	1.00	.00304	Catastrophic
-2	.249	.155	272	1.75	1.30	-	Center
-3	.248	.153	433	2.79	1.10	.00257	Edge Compression
-4	.245	.155	446	2.92	1.20	-	Edge Compression
-5	.249	.155	360	2.32	1.05	.00215	Edge Compression
-6	.249	.155	408	2.63	.97	.00272	Edge Compression
-7	.249	.155	465	3.00	1.20	.00246	Catastrophic
-8	.249	.156	407	2.63	1.00	.00264	Catastrophic
-9	.249	.156	480	3.08	1.05	.00287	Edge Compression
-10	.233	.146	378	2.59	1.10	.00236	Edge Compression
-11	.237	.148	452	3.05	1.10	.00277	Edge Compression
-12	.249	.155	436	2.80	1.00	--	Center
-13	.249	.155	444	2.86	1.10	.00263	Edge Compression
-14	.249	.156	427	2.74	1.10	-	Edge Compression
			Avg. -	2.70	1.09	.00262	
	GROUP: S5-						
S5-1	.249	.156	422	2.70	.90	-	Center
-2	.249	.156	430	2.76	1.00	.00270	Catastrophic
-3	.249	.156	375	2.40	.88	.00270	Catastrophic
-4	.249	.156	350	2.24	1.06	-	Edge Compression
-5	.249	.156	260	1.67	-	-	Edge Compression
-6	.249	.156	335	2.15	1.10	.00202	Edge Compression
-7	.248	.155	400	2.58	1.00	.00262	Center
-8	.248	.155	358	2.30	.88	.00260	Center
-9	.249	.156	382	2.45	.91	-	Edge Compression
-10	.250	.156	400	2.56	.91	.00284	Catastrophic
-11	.249	.156	450	2.88	.97	.00316	Catastrophic
-12	.249	.156	436	2.80	.92	.00305	Edge Compression
-13	.248	.155	448	2.89	.97	.00295	Edge Compression
-14	.249	.156	390	2.50	-	-	Edge Compression
			Avg. -	2.50	.95	.00274	

Table 24a

ROOM TEMPERATURE, EDGEWISE COMPRESSION PROPERTIES OF CPI MATERIAL WITH TWELVE-WEIGHT-PERCENT CoO ADDITIVE

Spec Ident	Thick. (centimeters)	Width (centimeters)	Fail. Load (Newtons)	Ult. Stress (N/m^2)	Mod. (N/m^2)	Strain at Failure	Mode of Failure
	GROUP: R1						
R1-1	6.38×10^{-1}	17.1×10^{-1}	2.24×10^{5}	2.05×10^{7}	-	-	Catastrophic
R1-2	6.35	17.2	2.41	2.21	11.0×10^{9}	2.6×10^{-3}	Center
R1-3	6.33	17.0	2.14	1.98	11.4	-	Edge Compression
			Avg.	2.08	11.2	2.6	
	GROUP: R3						
R3-1	6.33	19.2	2.36	1.94	8.48	2.32	Center
R3-2	6.25	18.1	1.97	1.74	8.07	-	Edge Compression
R3-3	6.33	18.2	1.87	1.63	-	-	Edge Compression
			Avg.	1.77	8.28	2.32	
	GROUP: R4						
R4-1	6.33	15.9	1.69	1.68	8.96	-	Edge Compression
R4-2	6.33	15.6	1.83	1.86	7.79	2.63	Catastrophic
R4-3	6.35	15.5	1.36	1.38	7.86	-	Edge Compression
			Avg.	1.64	8.20	2.63	

Table 24b

ROOM TEMPERATURE EDGEWISE COMPRESSION PROPERTIES OF C.P.I. MATERIAL WITH 12% COBALT ADDITIVE

Spec. Ident.	Thick. (In.)	Width (In.)	Fail Load (Lbs.)	Ult. Stress (psi)	Modulus (psi)	Strain at Failure	Mode of Failure
	GROUP: R1-						
R1-1	.251	.673	503	2,980	-	-	Catastrophic
2	.250	.675	542	3,200	1.60×10^6	2.6×10^{-3}	Center
3	.249	.670	480	2,870	1.66	-	Edge Compression
			Avg.	3,000	1.63	2.6	
	GROUP: R3-						
R3-1	.249	.755	531	2,820	1.23	2.32	Center
-2	.246	.711	442	2,530	1.17	-	Edge Compression
-3	.249	.715	420	2,360	-	-	Edge Compression
			Avg.	2,750	1.20	2.32	
	GROUP: R4-						
R4-1	.249	.625	380	2,440	1.30	-	Edge Compression
-2	.249	.615	412	2,700	1.13	2.63	Catastrophic
-3	.250	.609	305	2,000	1.14	-	Edge Compression
			Avg.	2,400	1.20	2.63	

Table 25a
SUMMARY OF AVERAGE MECHANICAL PROPERTIES OF SCALED-UP CPI TILES

PROPERTY		8% Cobalt Additive			12% Cobalt Additive		
		Strength (N/m^2)	Modulus (N/m^2)	Failure Strain	Strength (N/m^2)	Modulus (N/m^2)	Failure Strain
FLEXURE	SINGLE POINT	5.56×10^6	5.31×10^9	N/A†	5.67×10^6	6.69×10^9	N/A†
	QUARTER POINT	5.09	N/A†		(*)	(*)	(*)
TENSILE (DIAMETRAL COMPRESSION)		(*)	(*)	(*)	3.48	N/A†	N/A†
EDGEWISE COMPRESSION		17.0	6.96	2.49×10^{-3}	18.3	9.24	2.52×10^{-3}

(*) Not Scheduled For Testing

† Data Not Available

Table 25b

SUMMARY OF AVERAGE MECHANICAL PROPERTIES OF C.P.I.

PROPERTY		8% Cobalt Additive			12% Cobalt Additive		
		Strength (psi)	Modulus (psi)	Failure Strain	Strength (psi)	Modulus (psi)	Failure Strain
Flexure	Single Point	806	$.77\times10^{6}$	N. A.	823	$.97\times10^{6}$	N. A.
	Quarter Point	738	N. A.	$.705\times10^{-3}$	*	*	*
Tensile (Diametral Compression)		*	*	*	505	N. A.	N. A.
Edgewise Compression		2470	1.01	2.49	2660	1.34	2.52×10^{-3}

*Not scheduled for testing.

Table 26a

FOUR-POINT FLEXURAL STRENGTH OF ADDITIONALLY FIRED R- AND S-SERIES CPI TILES

Spec No.	Thick (cm)	Width (cm)	Ult Stress (N/m^2)	Mod (N/m^2)	Strain At Failure	Mode of Failure
	GROUP: 8% - COBALT					
S8-1	6.33×10^{-1}	15.9×10^{-1}	1.97×10^{4}	7.58×10^{9}	2.64×10^{-3}	Catastrophic
S8-2	6.35	15.8	1.68	6.62	2.65	Catastrophic
S8-3	6.38	15.9	1.83	5.72	-	Edge Comp.
S8-4	6.38	15.8	1.88	6.48	2.84	Center
S8-5	6.33	15.9	2.01	7.24	2.72	Center
S8-6	6.33	15.9	1.80	7.72	2.62	Edge Comp.
S8-7	6.35	15.8	1.75	7.38	2.51	Catastrophic
			1.86	6.89	2.70	
	GROUP: 12% - COBALT					
R12-1	6.40	15.8	1.32	5.72	2.40	Edge Comp.
R12-2	6.40	15.8	1.08	6.55	-	Edge Comp.
R13-3	6.40	15.9	1.32	7.03	-	Edge Comp.
R12-4	6.40	15.8	1.60	5.93	2.71	Catastrophic
R12-5	6.35	15.9	1.18	7.80	1.51	EdgeComp.
R12-6	6.38	15.8	1.61	6.34	2.56	Center
R12-7	6.38	15.9	1.49	-	-	Edge Comp.
			1.38	6.55	2.30	

RATE = .02 IN/MIN (600 # RANGE)

Table 26b

EDGEWISE COMPRESSIVE STRENGTH OF ADDITIONALLY FIRED R AND S SERIES CPI TILES

Spec. Ident.	Thick. (in.)	Width (in.)	Ult Stress (psi)	Modulus (psi)	Strain at Failure	Mode
			Group 8% Cobalt			
S8-1	.246	.620	2.81×10^3	1.09×10^6	Same as Table 26	Same as Table 26
S8-2	.247	.616	2.43	.96		
S8-3	.248	.620	2.65	.84		
S8-4	.248	.616	2.73	.93		
S8-5	.246	.620	2.91	1.05		
S8-6	.247	.620	2.61	1.20		
S8-7	.247	.620	2.53	1.07		
		Avg.	2.69	.99		
			Group 12% Cobalt			
R12-1	.249	.616	1.92	.78		
R12-2	.249	.616	1.56	.94		
R12-3	.249	.620	1.91	1.01		
R12-4	.249	.616	2.32	.86		
R12-5	.247	.620	1.73	1.13		
R12-6	.248	.616	2.33	.92		
R12-7	.248	.620	2.16	-		
		Avg.	2.00	.94		

Table 27a

SINGLE POINT FLEXURAL STRENGTH OF ADDITIONALLY FIRED R- AND S-SERIES CPI TILES

Spec Ident	Thick. (cm)	Width (cm)	Ult. Stress (N/m^2)	Mod x 10 (N/m^2)	Mode of Failure
	GROUP:	8% COBALT			
8-4	6.35×10^{-1}	12.7×10^{-1}	5.67×10^{6}	7.17×10^{9}	Flex. -Center
8-5	6.35	12.7	6.13	6.55	Flex. -Center
8-6	6.35	12.7	5.52	6.89	Flex. -Center
8-7	6.35	12.7	6.665	7.10	Flex. -Center
8-8	6.35	12.7	6.08	7.86	Flex. -Center
8-9	6.35	12.7	6.06	7.86	Flex. -Center
8-10	6.35	12.7	4.61	7.31	Flex. -Center
		Avg.	5.82	7.25	
	GROUP:	12% COBALT			
12-3	6.35	12.7	5.90	6.76	Flex. -Center
12-4	6.33	12.8	4.79	6.00	Flex. -Center
12-5	6.35	12.8	5.56	6.62	Flex. -Center
12-6	6.35	12.8	5.21	6.21	Flex. -Center
12-7	6.35	12.8	4.57	7.24	Flex. -Center
12-8	6.35	12.8	5.03	6.34	Flex. -Center
		Avg.	5.18	6.53	

Table 27b

SINGLE POINT FLEXUAL STRENGTH OF ADDITIONALLY FIRED R AND S SERIES CPI TILES

Spec. Ident.	Thick. (in.)	Width (in.)	Ult. Stress (psi)	Modulus (psi)	Mode of Failure
		Group 8% Cobalt			
8-4	.247	.495	8.22x10^2	1.04x10^6	Same as Table 27
8-5	.247	.495	8.88	.94	
8-6	.247	.495	8.00	.99	
8-7	.247	.495	9.65	1.03	
8-8	.247	.495	8.81	1.13	
8-9	.247	.495	8.78	1.13	
8-10	.247	.495	6.75	1.06	
		AVG.	8.43	1.05	
		Group 12% Cobalt			
12-3	.247	.495	8.55	.98	
12-4	.246	.499	6.95	.87	
12-5	.247	.499	8.06	.96	
12-6	.247	.499	7.55	.90	
12-7	.247	.499	6.65	1.05	
12-8	.247	.499	7.29	.92	
		AVG.	7.51	.95	

Table 28a

FOUR-POINT FLEXURAL STRENGTH OF ADDITIONALLY FIRED R- AND S-SERIES CPI TILES

Specimen	Thickness (cm)	Width (cm)	Failure Stress (N/m^2)	Modulus (N/m^2)	Failure Strain	Failure Mode
S8-1	6.25×10^{-1}	12.5×10^{-1}	5.06×10^{6}	-	.00058	-
S8-2	6.25	12.5	4.74		.00056	Load Point
S8-3	6.25	12.5	5.09	5.58×10^{9}	-	Center
S8-4	6.25	12.5	5.21	6.41	-	Load Point
S8-5	6.25	12.5	4.92	6.41	-	Load Point
S8-6	6.25	12.5	5.20	6.76	-	Near Load Pt.
S8-7	6.25	12.5	5.28	7.38	-	Near Load Pt.
S8-8	6.25	12.5	5.22	6.96	-	Near Load Pt.
S8-9	6.25	12.5	4.80	6.69	-	Load Point
		Avg =	5.03	6.68		
R12-1	6.25	12.5	4.90	-	.00064	Load Point
R12-2	6.25	12.5	5.00	-	.00064	Load Point
R12-3	6.25	12.5	4.98	6.89	-	Load Point
R12-4	6.25	12.5	4.61	6.41	-	Load Point
R12-5	6.25	12.5	4.71	6.34	-	Load Point
R12-6	6.25	12.5	4.17	6.41	-	Load Point
R12-7	6.25	12.5	4.78	7.03	-	Center
R12-8	6.25	12.5	4.65	6.48	-	Load Point
		Avg =	4.76	6.61		

Table 28b

FOUR-POINT FLEXUAL STRENGTH OF ADDITIONALLY FIRED RAND S SERIES CPI TILES

Spec. Ident.	Thick. (in.)	Width (in.)	Failure Stress (psi)	Modulus (psi)	Failure Strain	Failure Mode
S 8-1	.243	.487	7.33x102	-	Same as Table 28	
S 8-2	.243	.487	6.87	-		
S 8-3	.243	.487	7.38	.81 x 10^6		
S 8-4	.243	.487	7.55	.93		
S 8-5	.243	.487	7.13	.93		
S 8-6	.243	.487	7.54	.98		
S 8-7	.243	.487	7.65	1.07		
S 8-8	.243	.487	7.57	1.01		
S 8-9	.243	.487	6.96	.97		
		AVG.	7.30	.97		
R12-1	.243	.487	7.10	-		
R12-2	.243	.487	7.25	-		
R12-3	.243	.487	7.22	.99		
R12-4	.243	.487	6.68	.93		
R12-5	.243	.487	6.82	.92		
R12-6	.243	.487	6.04	.93		
R12-7	.243	.487	6.93	1.02		
R12-8	.243	.487	6.75	.94		
		AVG.	6.93	.96		

Table 29

SUMMARY OF THERMAL CYCLING DATA

Specimen	Run	Specimen Dimensions	Max Temperature, K	
			Frontface	Backface
R1	1	10 cm x 10 cm x 0.625 cm	1477	1422
	2			
	3			
	4			
	5			
	6			
	7			
	8			
	9			
	10			
R3	1		1366	1322
	2			
	3			
	4			
	5			
	6			
	7			
	8			
	9			
	10			
R4	1	10 cm x 10 cm x 0.625 cm	1366	1322
	2			
	3			
	4			
	5			
	6			
	7			
	8			
	9			
	10			
S3	1		1422	1394
	2			
	3			
	4			
	5			
	6			
	7			
	8			
	9			
	10			

Table 30

CALIBRATION TEST RESULTS

Test No	Heat Flux Enthalpy h_{hf} (Btu/lb)	Energy Balance Enthalpy h_{eb} (Btu/lb)	Static Pressure[1] p_1 (atm)	p_2 (atm)	Arc Chamber Pressure p_c (atm)	Test Chamber Pressure p_e (mm Hg)	Cold Wall Heat Flux[2] q_s (Btu/ft^2-sec)	Nozzle Size d_e (inch)	Gas Mass Flow Rate m (lb/sec)	Gas Composition[3]	Comments
1955A	2640	1840	0.0052	0.0051	0.164	.29	9.25	8.0	0.0134	Air	Initial Condition
1995C	6390	3720	0.0074	0.0072	0.226	│	26.7	│	│	│	Typical higher conditions greater than the 2200° F condition.
1995B	8160	4580	0.0084	0.0082	0.242	│	36.3	│	│	│	

[1] Static pressure as measured at tape 1 and 2 on calibration model.

[2] Cold Wall Heat Flux as measured with Calorimeter No. 1 (C_L) on calibration model.

[3] Air expressed as 76.8 percent nitrogen and 23.2 percent oxygen by mass.

Table 31

MODEL TEST RESULTS

OPERATING CONDITIONS										DIMENSIONAL AND WEIGHT DATA FOR 10 CYCLES			
		Model Type											
Cycle	Selected Condition[1]	Calibration	Test	Heat Flux Enthalpy h_{hf} (Btu/lb)	Energy Balance Enthalpy h_{eb} (Btu/lb)	Static Pressure[2] p (atm)	Arc Chamber Pressure p_c (atm)	Test Chamber Pressure p_e (mm Hg)	Cold Wall Heat Flux[3] q_s (Btu/ft^2-sec)	Specimen Type	Mass Loss m (gm)	Radius Change R (mils)	Surface Recession s (mils)
1	I	√		-	1740	-	0.162	.290	9.04	8%	0.047	3	-1 to -3
	S		√	4650	2840	0.0067	0.209	|	18.50	12%	0.030	14	-1 to -4
2	|	√		-	3090	-	0.208	|	20.00				
	|		√	4580	3130	0.0066	|	|	18.20				
3	I	√		-	1790	-	0.166	|	9.47				
	S		√	4800	3130	0.0067	0.209	|	19.10				
4	|	√		-	3000	-	0.208	|	20.20				
	|		√	4530	3020	0.0067	0.206	|	18.00				
5	I	√		-	1720	-	0.163	|	9.10				
	S		√	4800	3140	0.0067	0.209	|	19.10				
6	|	√		-	2980	-	0.206	|	19.80				
	|		√	4730	3120	0.0067	0.208	|	18.80				
7	I	√		-	1790	-	0.162	|	8.81				
	S		√	4700	3080	0.0066	0.207	|	18.70				
8	|	√		-	3060	-	|	|	19.90				
	|		√	4780	|	0.0067	0.209	|	19.00				
9	I	√		-	1970	-	0.165	|	9.33				
	S		√	4680	3030	0.0066	0.207	|	18.60				
10	|	√		-	3170	-	0.208	|	20.00				
	|		√	4680	3050	0.0067	|	|	18.60				

[1] I = initial condition; S = steady state condition for 2200° F. For the test model the selected condition is that recorded 7.5 minutes after insertion.

[2] Static pressure as measured on test model.

[3] Heat flux as measured by centerline calorimeter on calibration model or test model as indicated.

Table 32

ELASTIC MODULUS AND DAMPING CAPACITY OF CPI TILES AFTER RE-ENTRY CYCLING

8% Tile	$E(N/m^2)$	Mech Damp
Number of Cycles		
0	6.07×10^9	6.45×10^4
1	5.65	6.40
5	8.28	6.15
12% Tile		
0	7.10	6.90
1	6.54	6.10
5	6.09	6.95
10	6.65	6.95

Table 33

CHARACTERISTICS OF CPI HEAT SHIELD

- Needs No Waterproof Coating
- High Emittance Additive Built Into Basic Heat Shield Formulation
- Needs No Special Erosion Protection Coating
- Minimal Handling Problems
- No Expansion Mismatch Problems Due to Coating on Thermal Cycling
- Easier NDT Testing & Inspection
- Much Higher Strength & Stiffness
- No Venting & Depressurization Problem Due to Coatings
- Can Be Machined Into Any Desired Shape & Size With Conventional Tooling
- Mechanical Attachment Schemes Possible
- Low Cost of Raw Materials
- Panels Easily Detachable
- Greater Design Flexibility
- Greater Overall Reliability

Table 34

WEIGHT ANALYSIS OF COMPOSITE CPI-HONEYCOMB HEAT SHIELD

I. MATERIAL DENSITIES

(1) CPI = 35.0 pcf
(2) MICROQUARTZ = 3.5 pcf
(3) TITANIUM = 282 pcf
(4) INCONEL 713 = 512 pcf
(5) BAGGING = 0.15 psf

II. 3/8" CPI INCONEL SYSTEM

0.375" CPI FACESHEET = 1.09 psf
2" INCO CORE (Pc = 8.17 pcf) = 1.36
2" CORE MICROQUARTZ = 0.58
0.008" INCO FACESHEET = 0.34
3.5" MICROQUARTZ = 1.02
BAGGING = 0.15

TOTAL WEIGHT* = 4.54 psf

III. 3/8" CPI TITANIUM SYSTEM

0.375" CPI FACESHEET = 1.09 psf
2" TI-3AL-2.5V CORE (Pc = 4.30 pcf = 0.72
2" CORE MICROQUARTZ = 0.58
0.08" TI-6AL-4V FACESHEET = 0.19
3.5" MICROQUARTZ = 1.02
BAGGING = 0.15

TOTAL WEIGHT* = 3.75 psf

*NOTE: DOES NOT INCLUDE WEIGHT OF SUPPORT

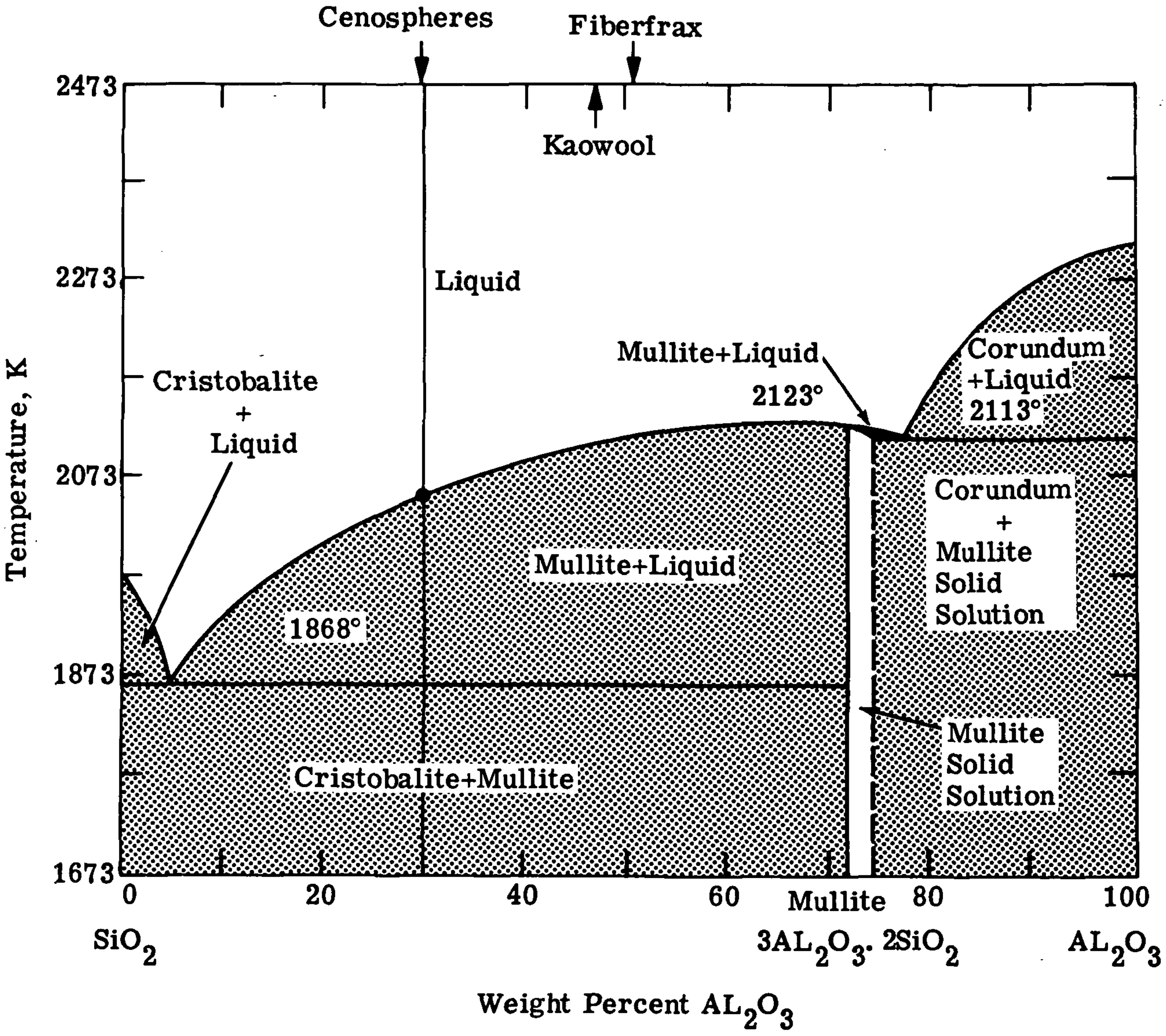

Fig. 1 Alumina-Silica Equilibrium Diagram [After Levin, Robbins, and McMurde (Ref. 3)]

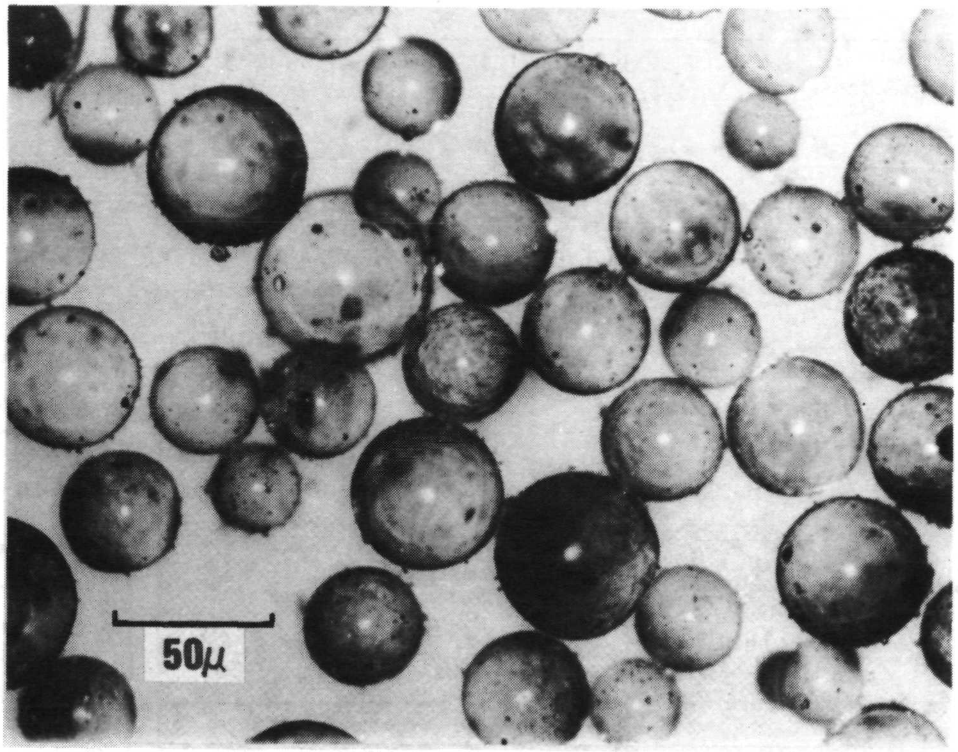

Fig. 2 Photomicrograph of Cenospheres

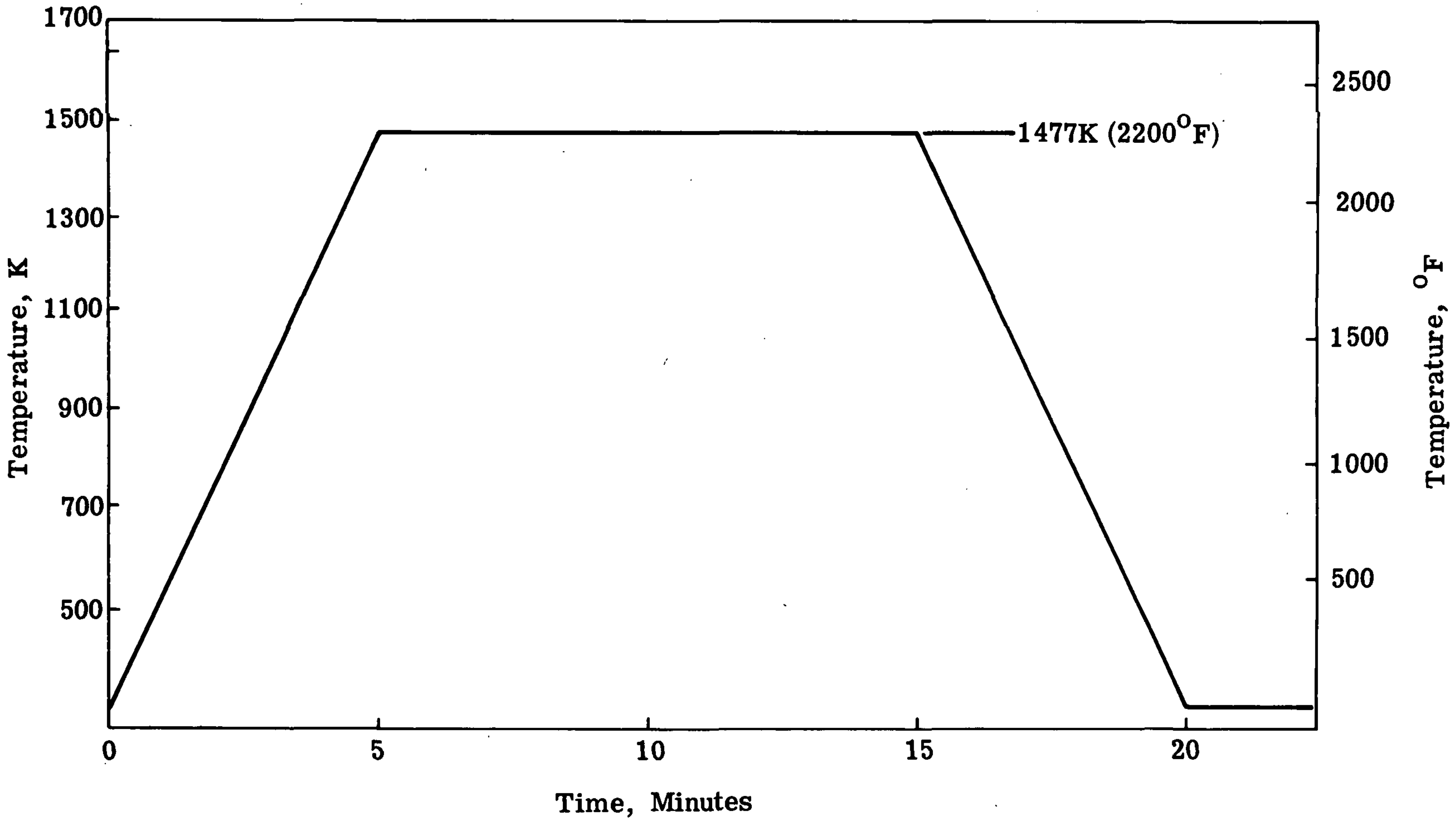

Fig. 3 Simulated Re-entry Time-Temperature Profile

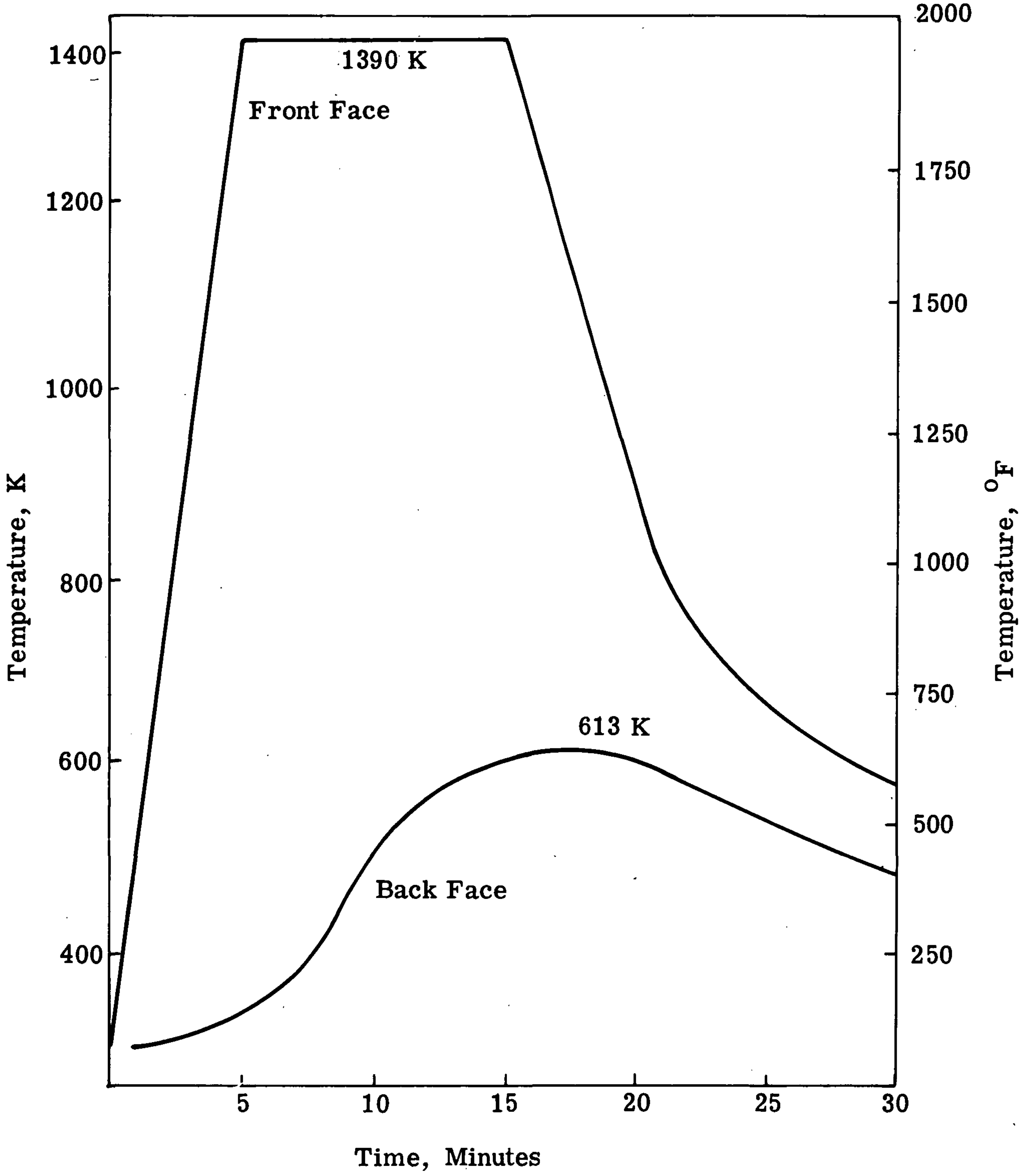

Fig. 4 Re-entry Test on Sintered Cenosphere Panel 2.54 cm Thick (Showing Back Face Response)

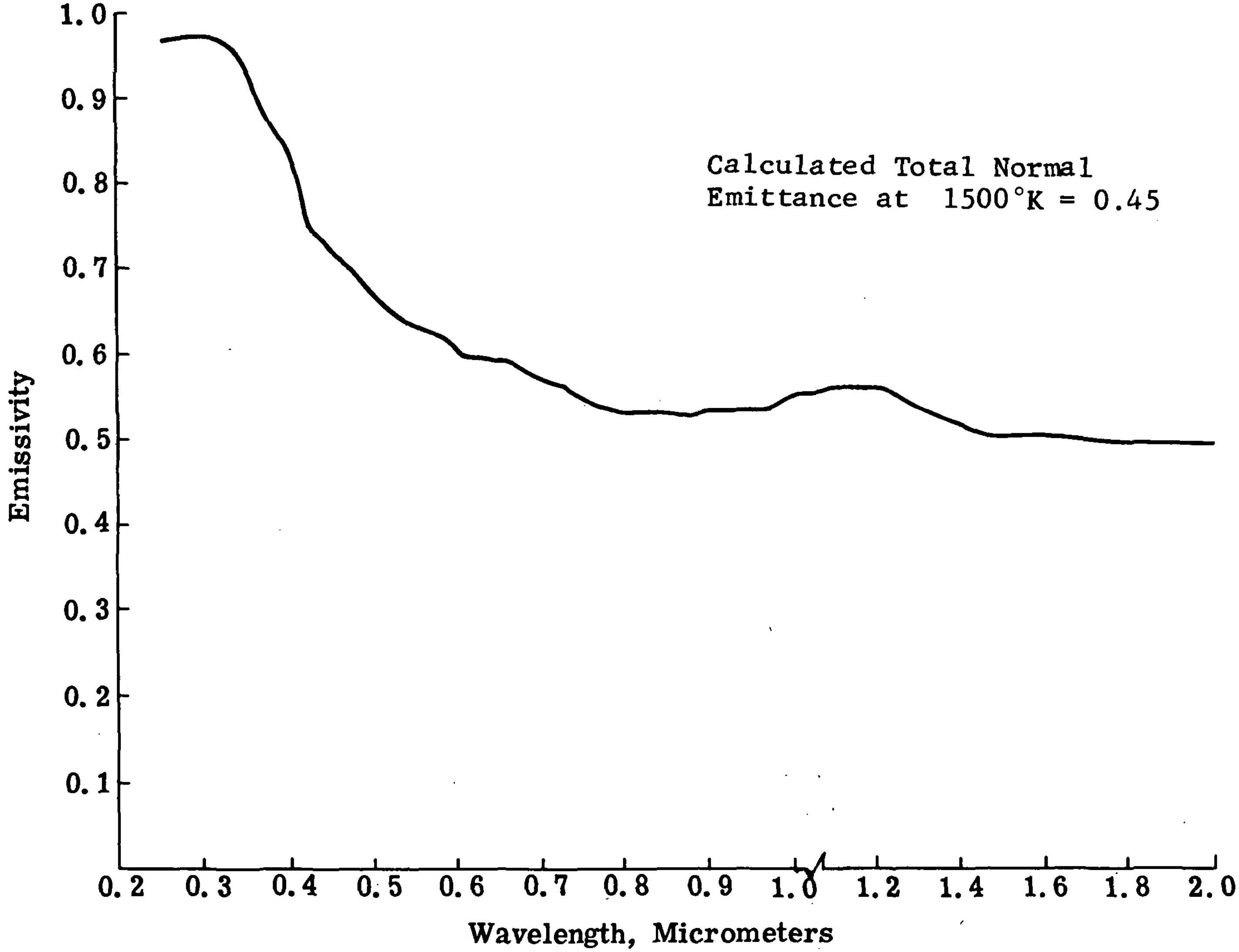

Fig. 5a Spectral Emissivity versus Wavelength of Furnace-Cooled Sintered Cenosphere (Integrating Sphere)

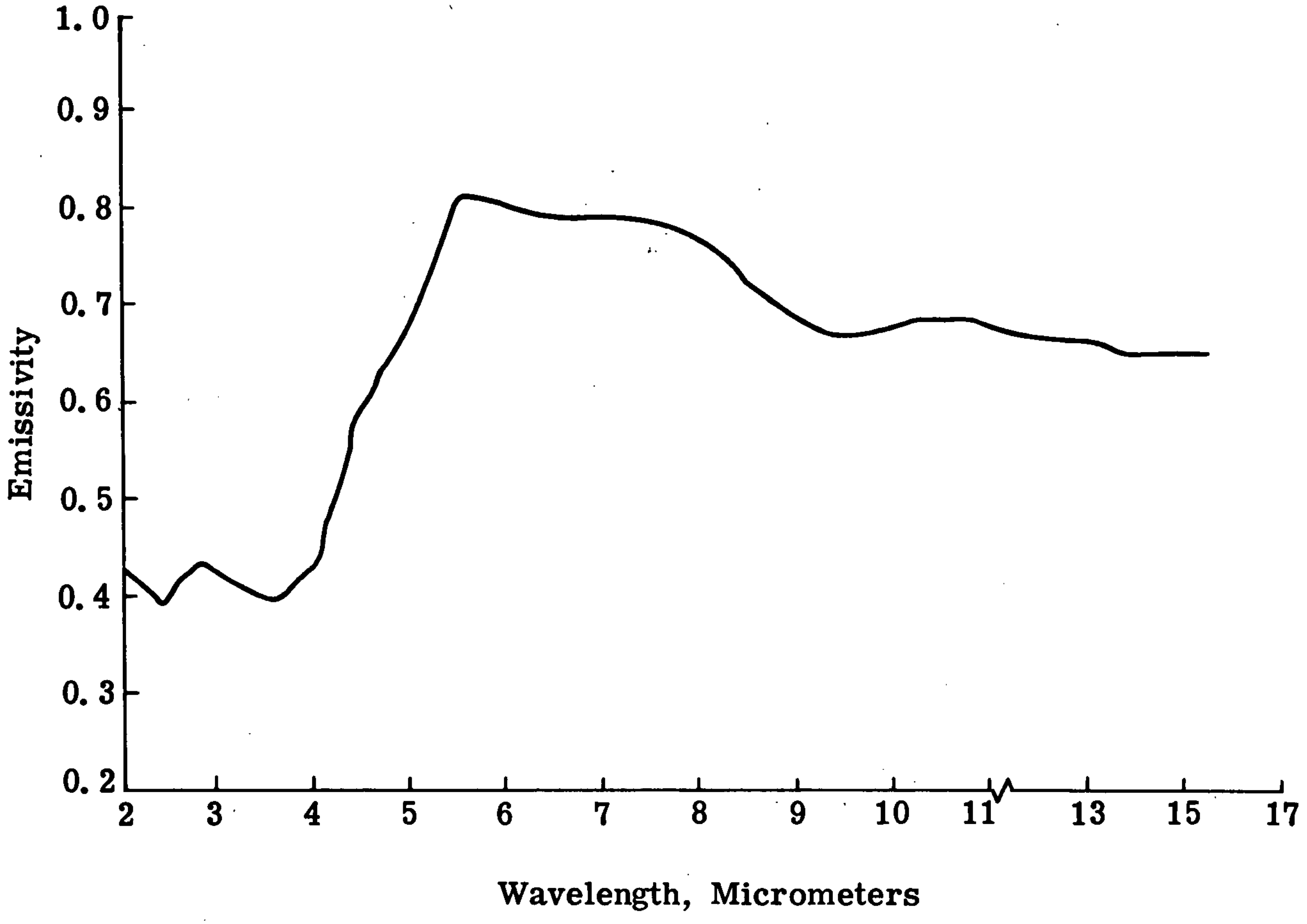

Fig. 5b Spectral Emissivity versus Wavelength of Furnace-Cooled Sintered Cenosphere (Heated Cavity)

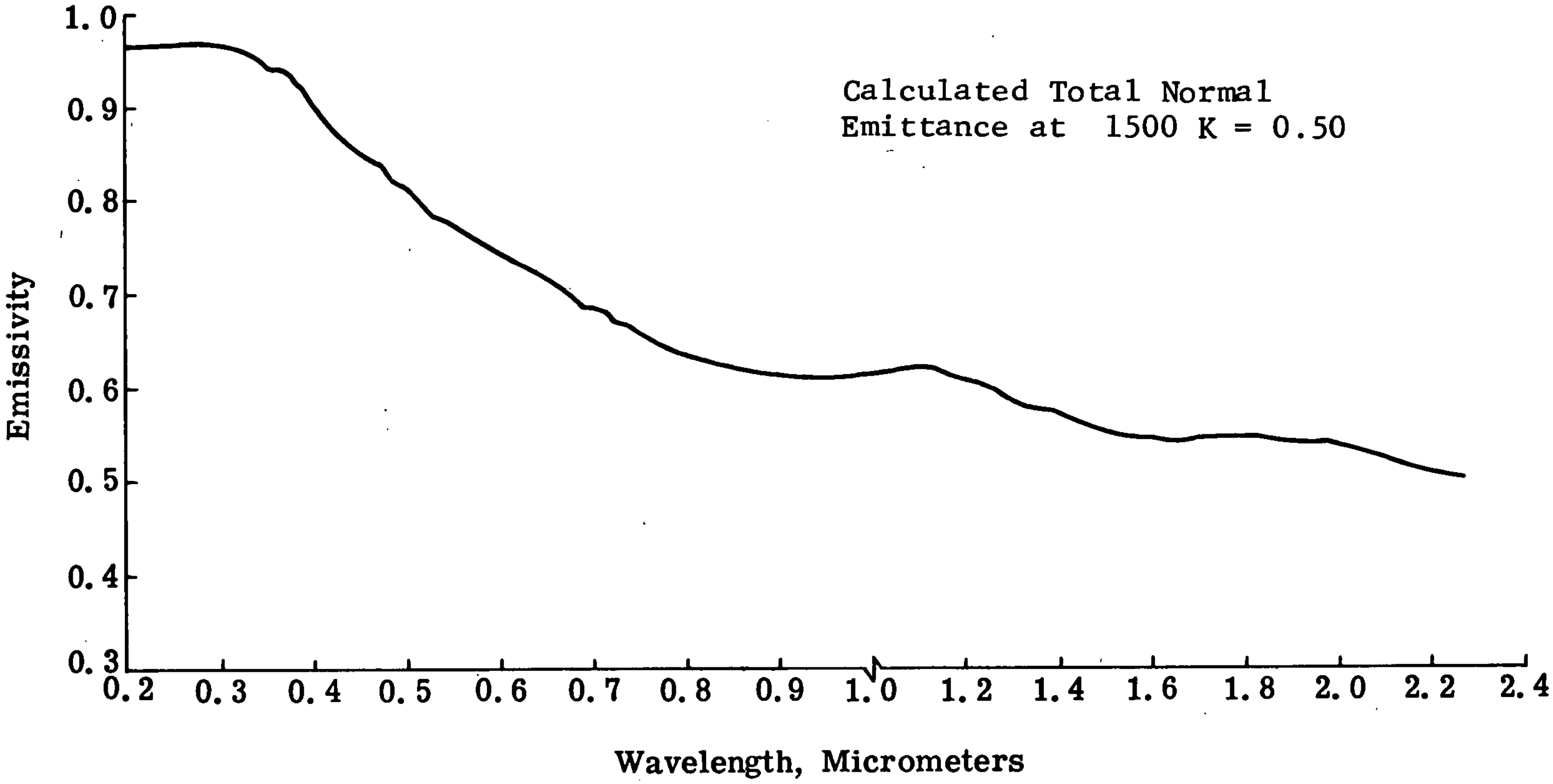

Fig. 6a Spectral Emissivity versus Wavelength of Sintered Cenosphere Body Quenched from 1700°K (Integrating Sphere)

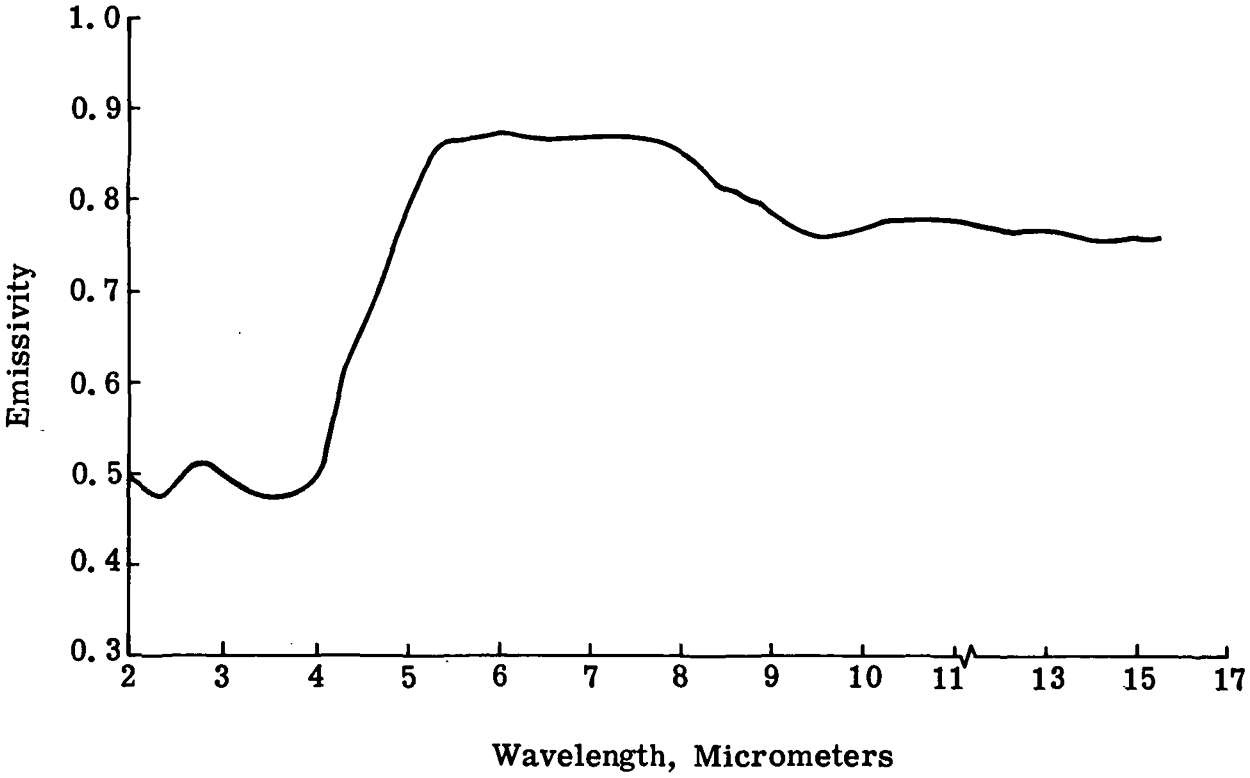

Fig. 6b Spectral Emissivity versus Wavelength of Sintered Cenosphere Body Quenched from 1700°K (Heated Cavity)

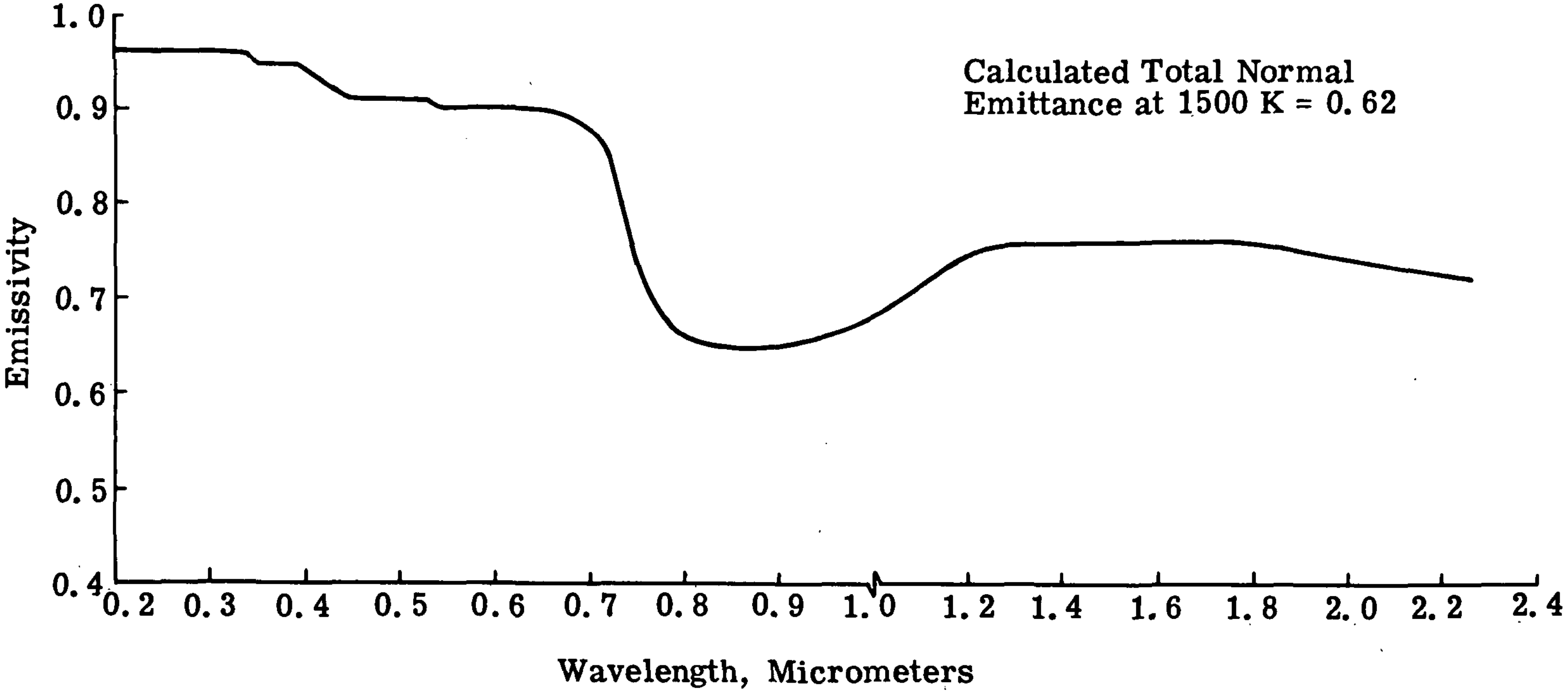

Calculated Total Normal Emittance at 1500 K = 0.62

Fig. 7a Spectral Emissivity versus Wavelength of Sintered Cenosphere Body with Four-Weight-Percent CoO Additive (Integrating Sphere)

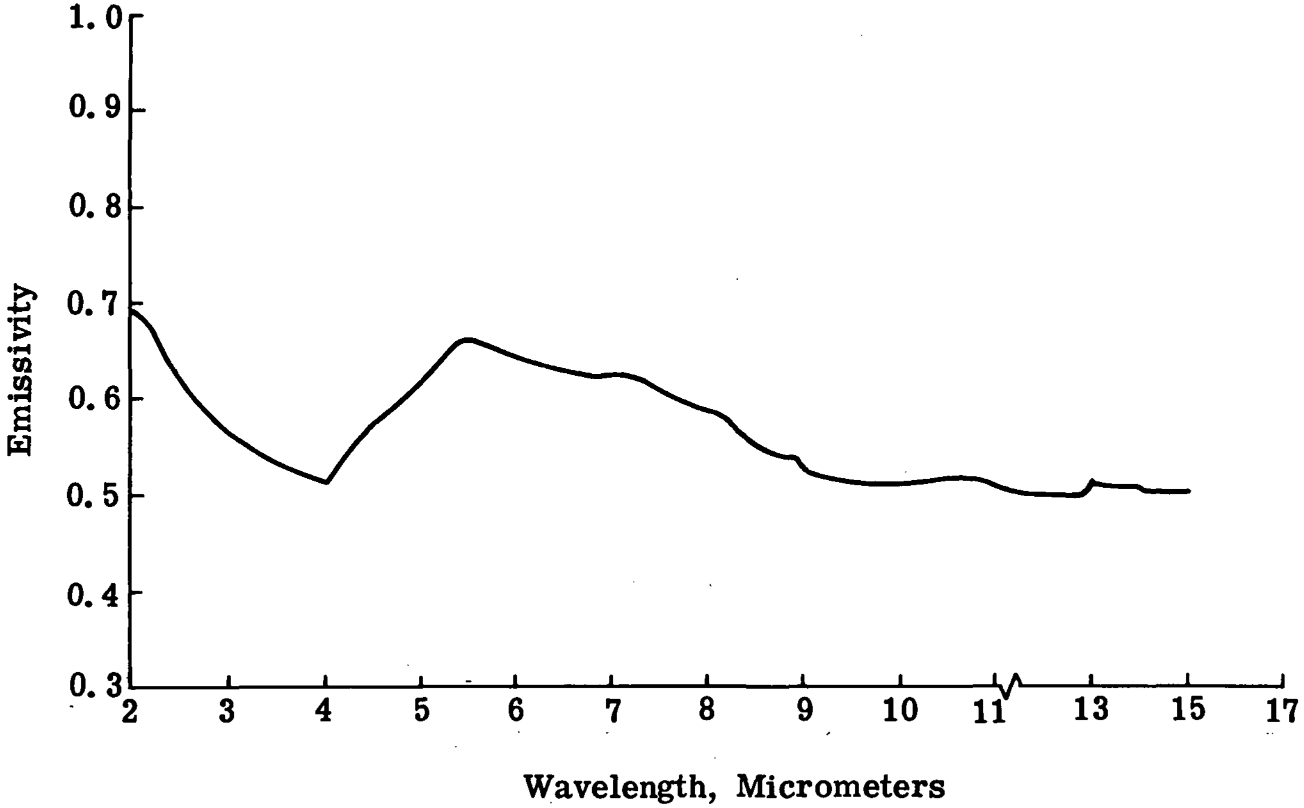

Fig. 7b Spectral Emissivity versus Wavelength of Sintered Cenosphere Body with Four-Weight-Percent CoO Additive (Heated Cavity)

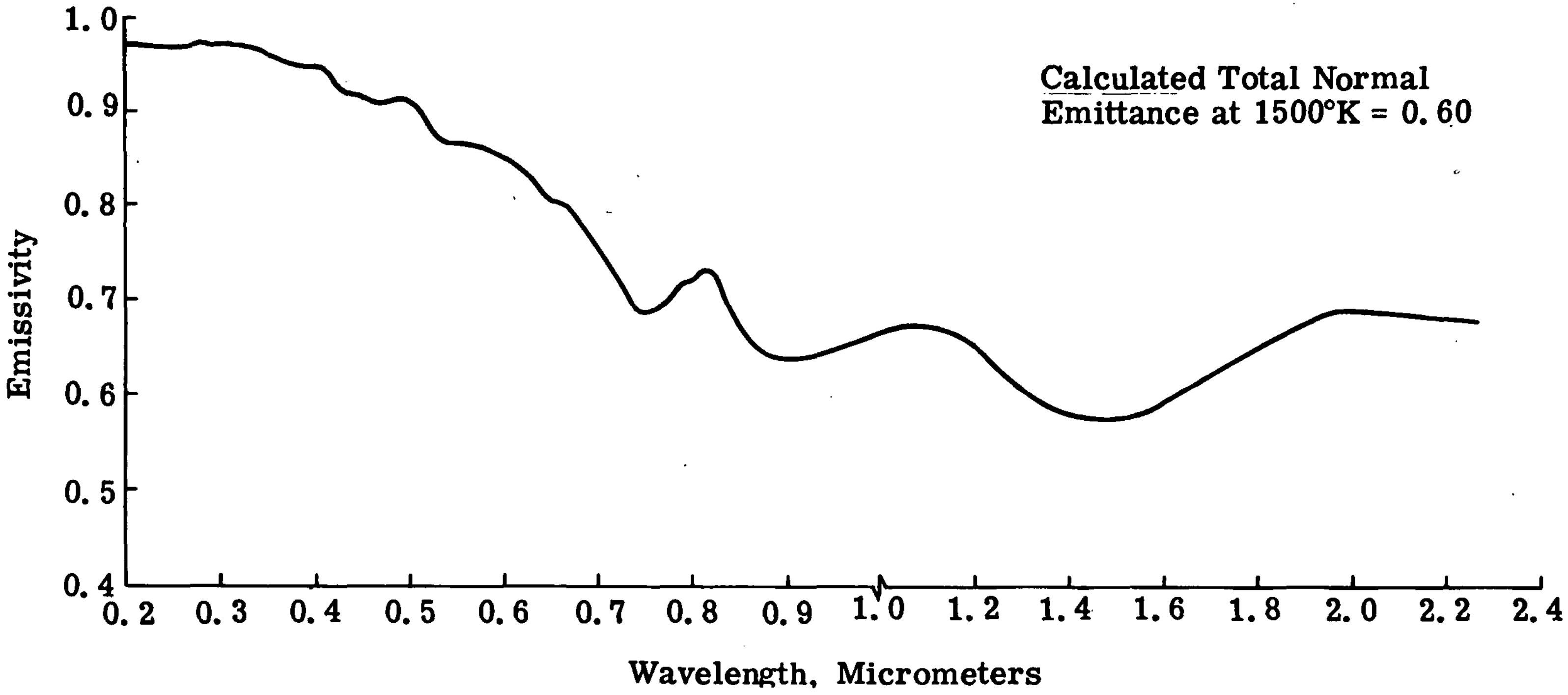

Fig. 8a Spectral Emissivity versus Wavelength of Sintered Cenosphere Body with Four-Weight-Percent NiO Additive (Integrating Sphere)

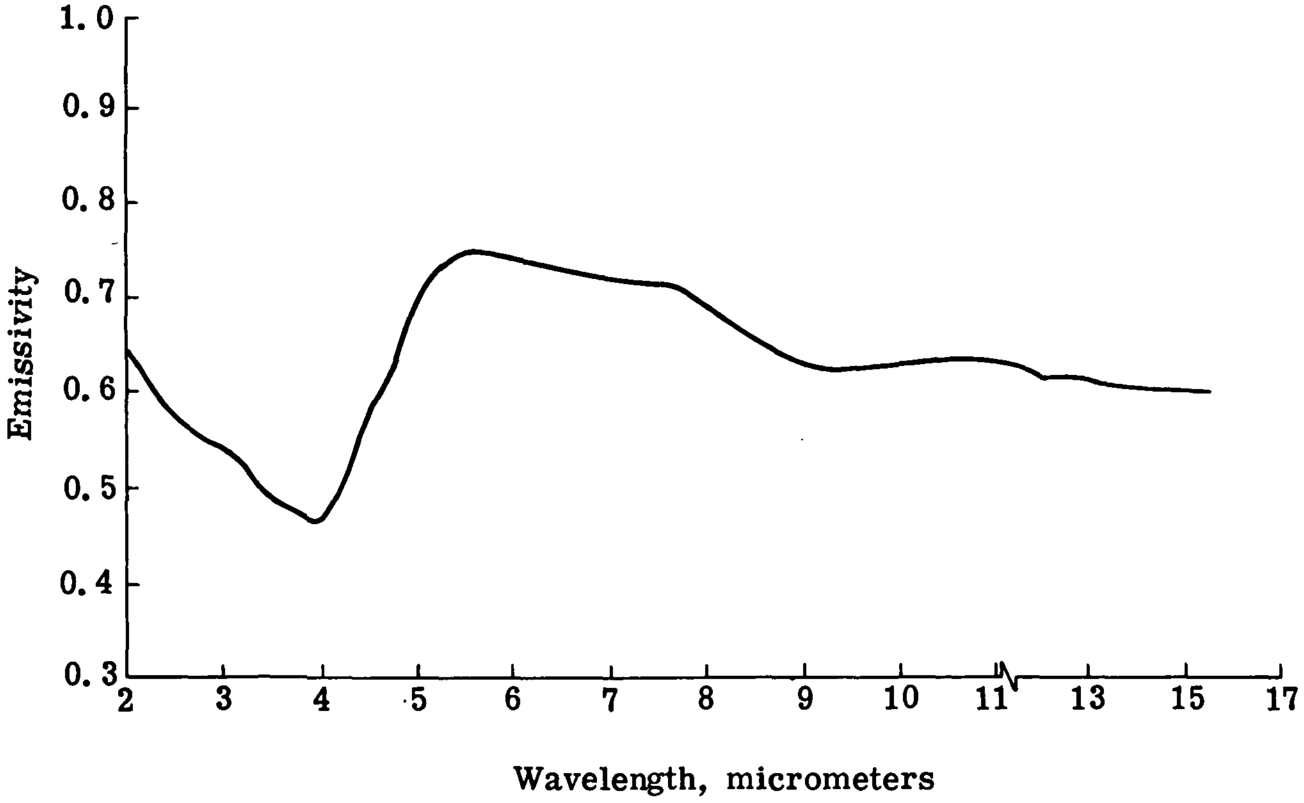

Fig. 8b Spectral Emissivity versus Wavelength of Sintered Cenosphere Body with Four-Weight-Percent NiO Additive (Heated Cavity)

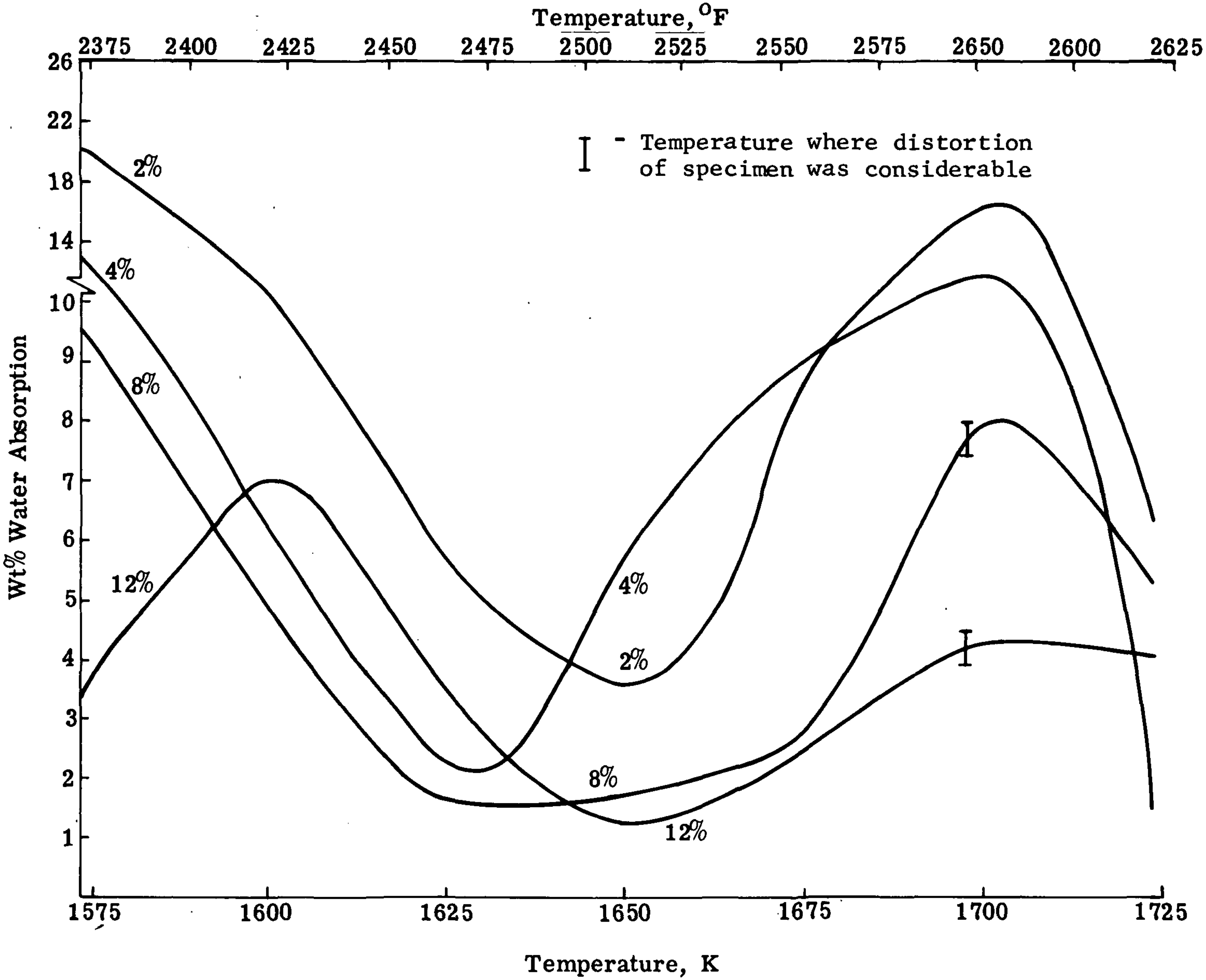

Fig. 9 Weight Percent Water Absorbtion versus Temperature in Sintered Cenosphere Bodies for Varying Amount of CoO Additive (One-Half Hour Firing Time)

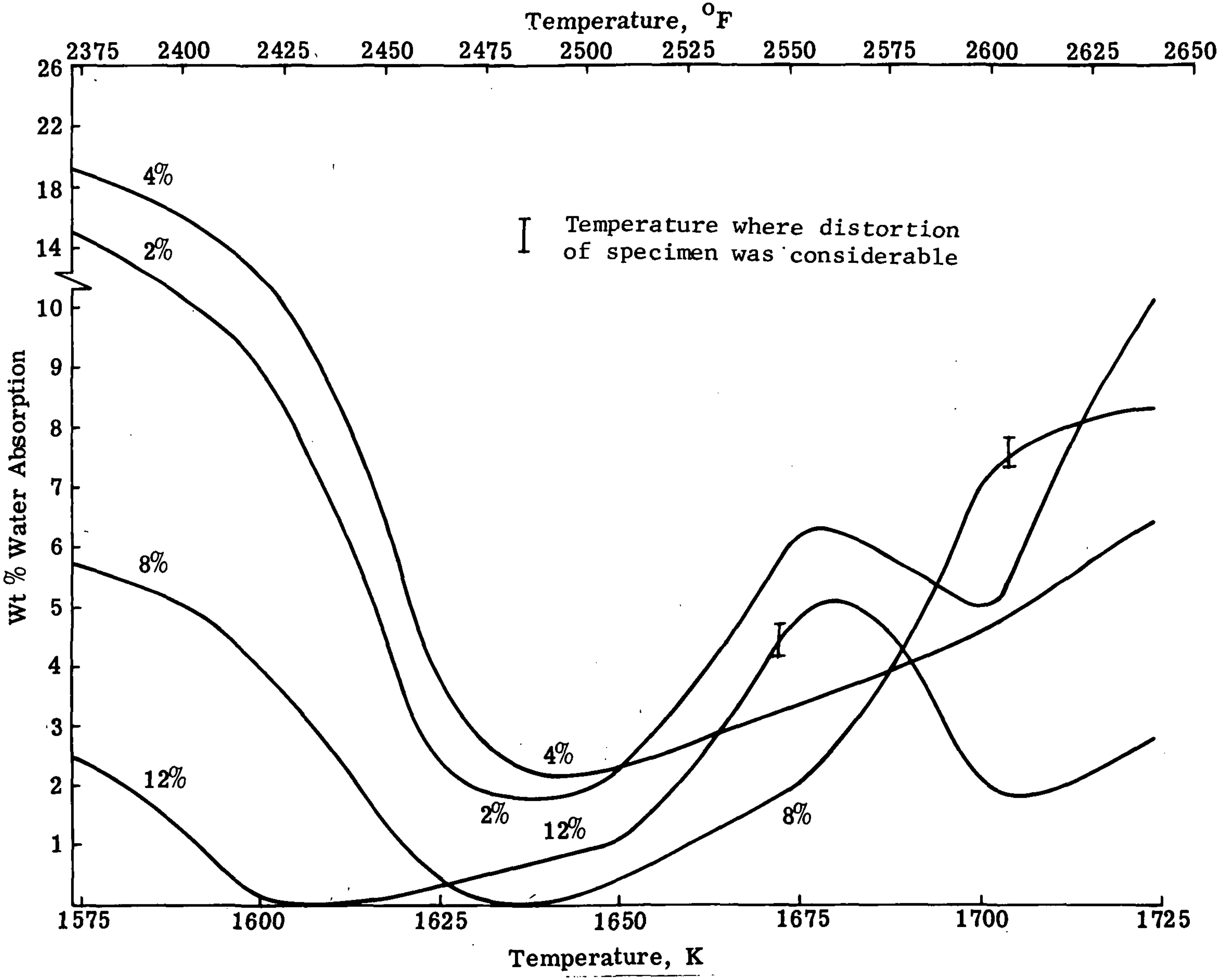

Fig. 10 Weight Percent Water Absorption versus Temperature in Sintered Cenosphere Bodies for Varying Amount of CoO Additive (One Hour Firing Time)

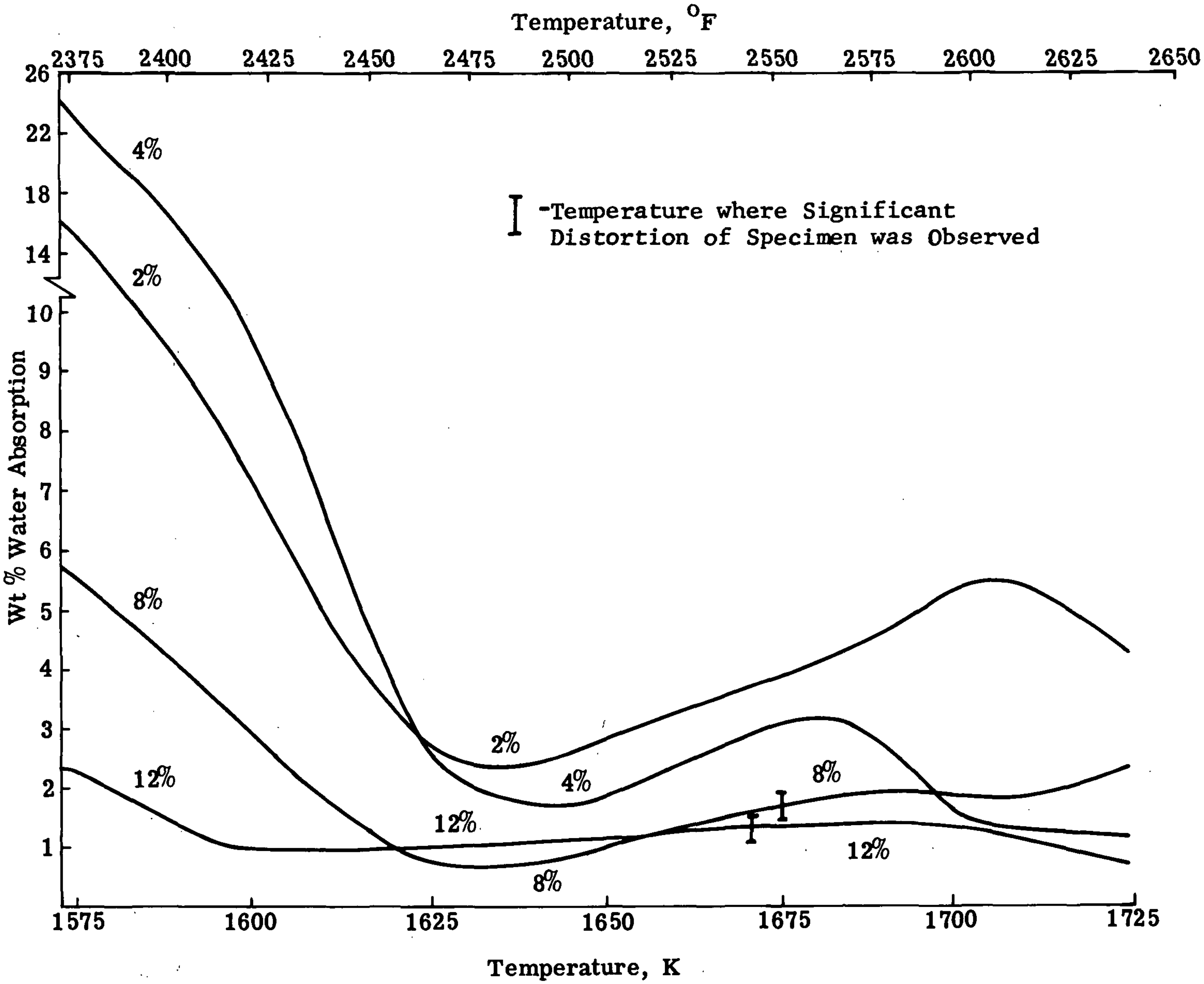

Fig. 11 Weight Percent Water Absorption versus Temperature in Sintered Cenosphere Bodies for Varying Amounts of CoO Additive (Two Hour Firing Time)

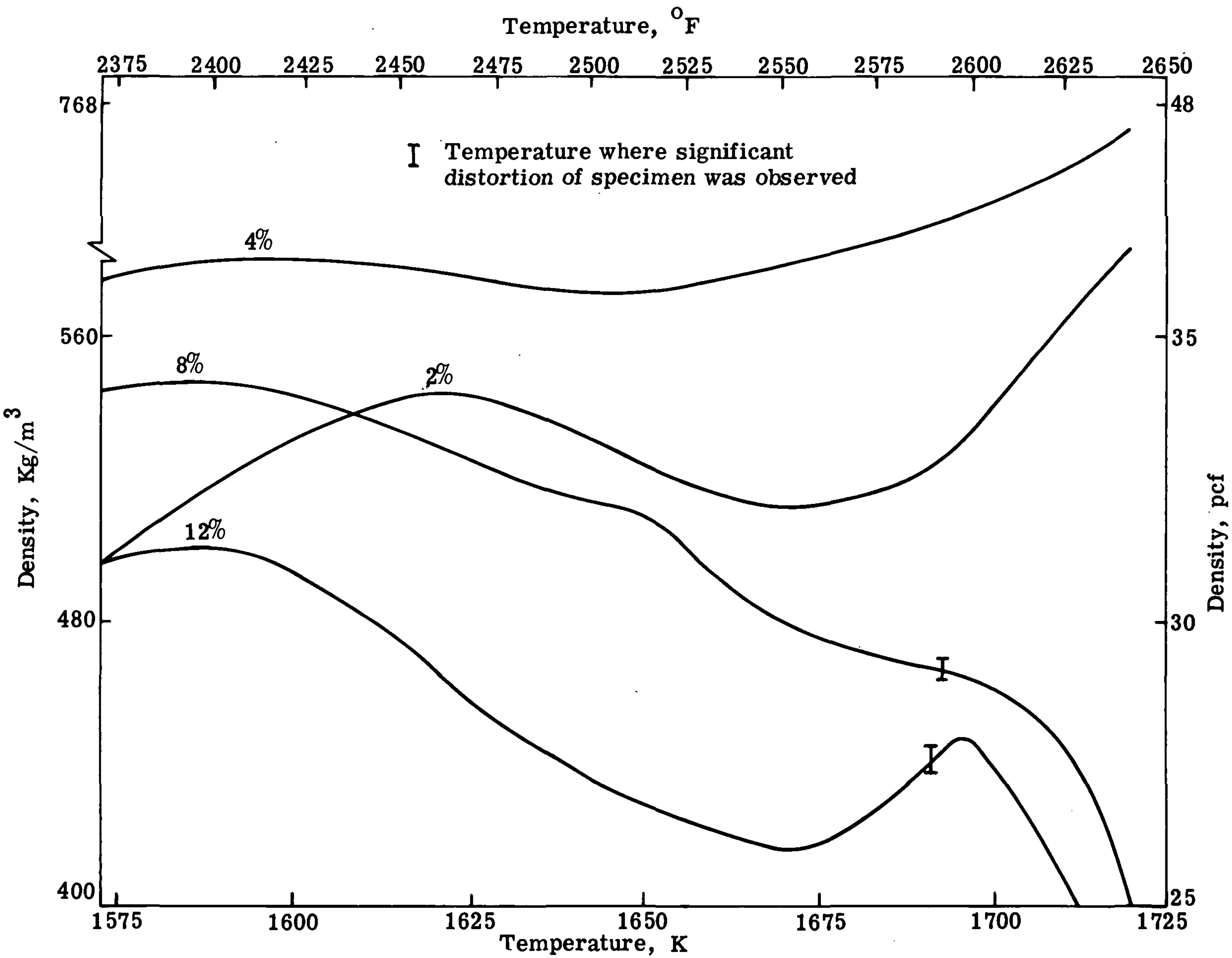

Fig. 12 Density versus Temperature of Sintered Cenosphere Bodies for Various CoO Concentrations (Half-Hour Firing Time)

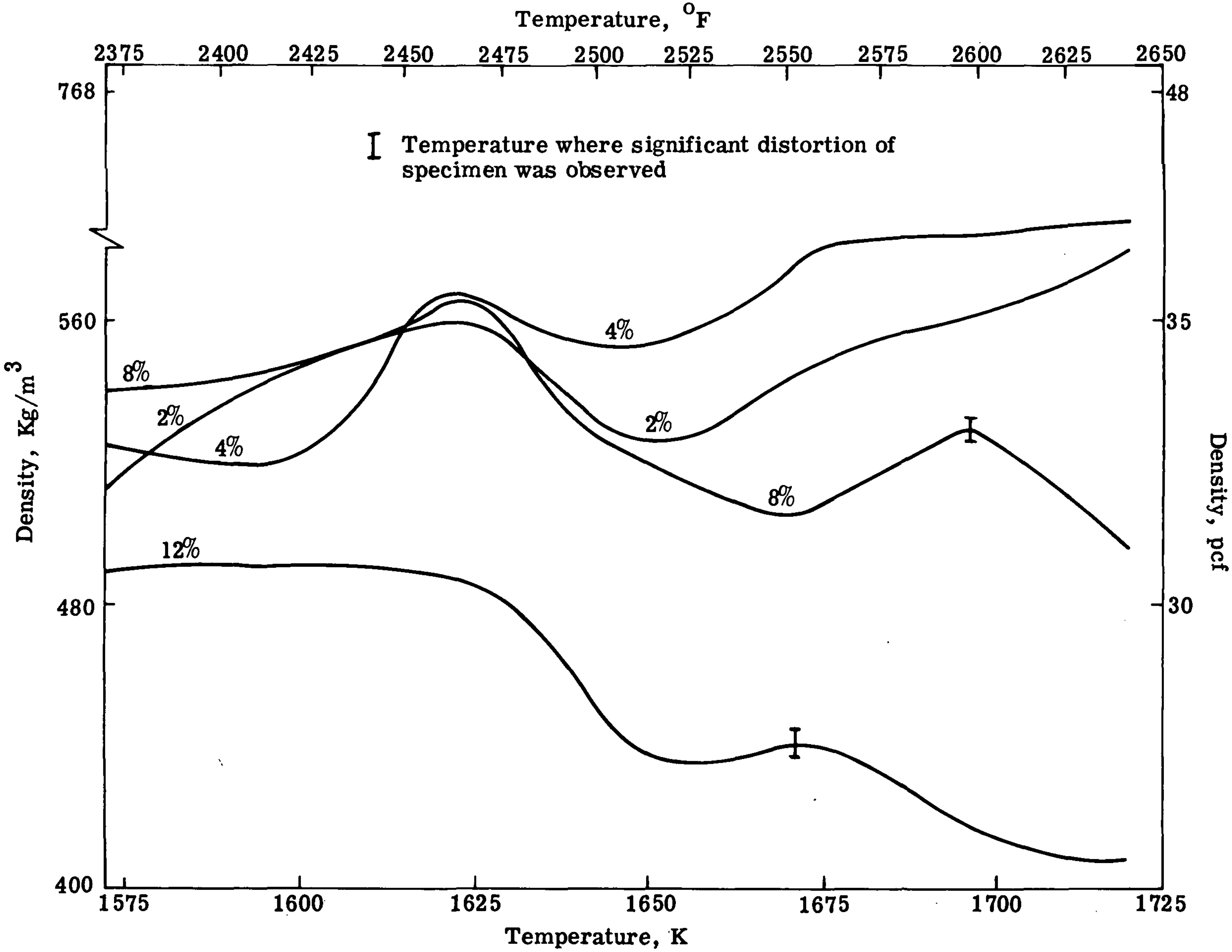

Fig. 13 Density versus Temperature of Sintered Cenosphere Bodies for Various CoO Concentrations (One Hour Firing Time)

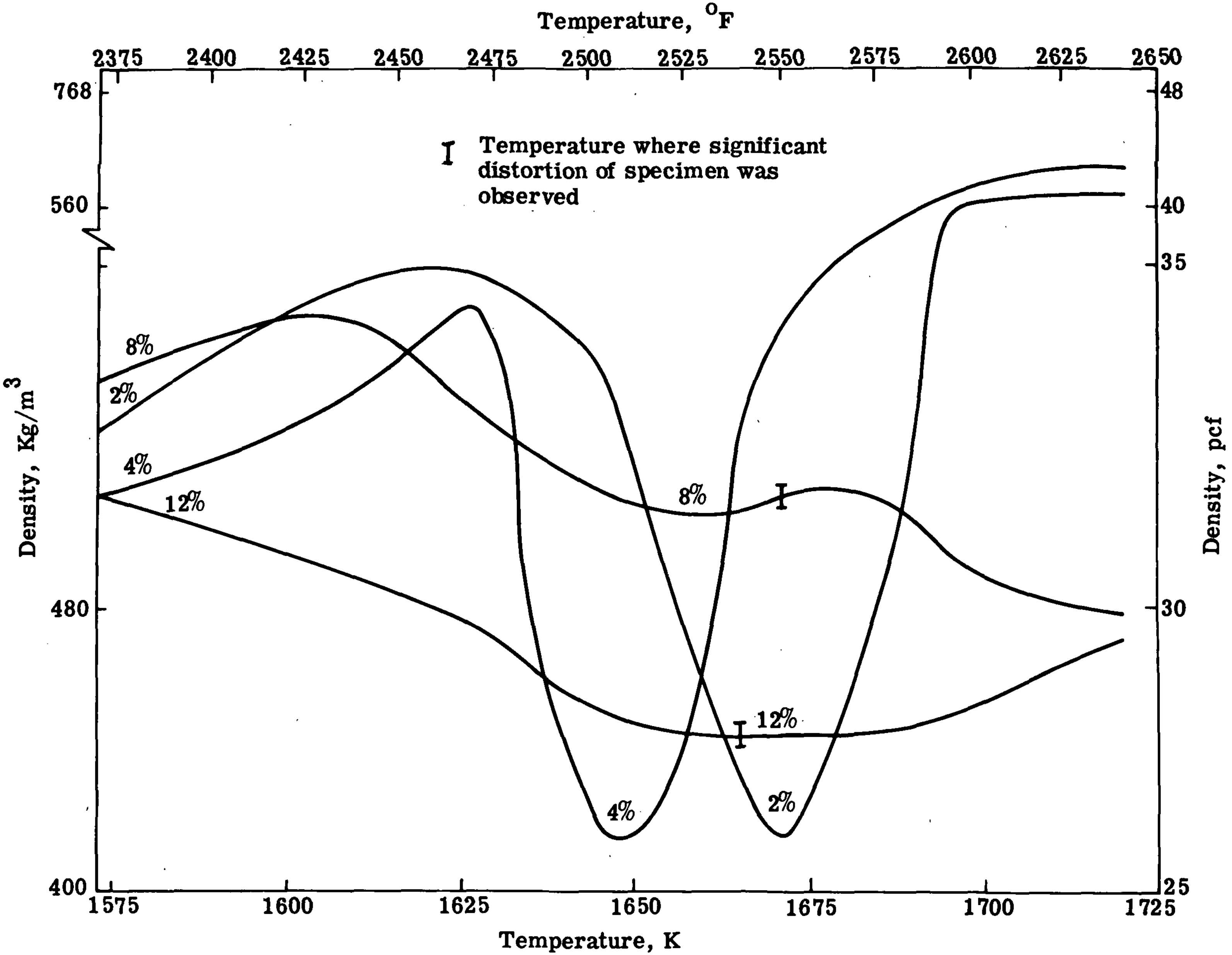

Fig. 14 Density versus Temperature of Sintered Cenosphere Bodies for Various CoO Concentrations (Two Hour Firing Time)

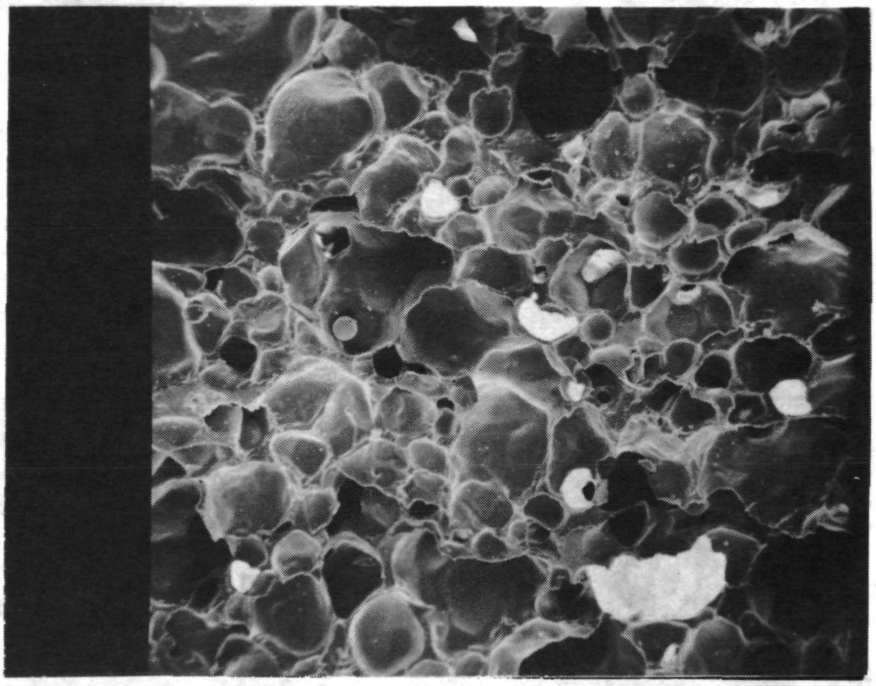

4 Wt.% CoO Additive (100X)

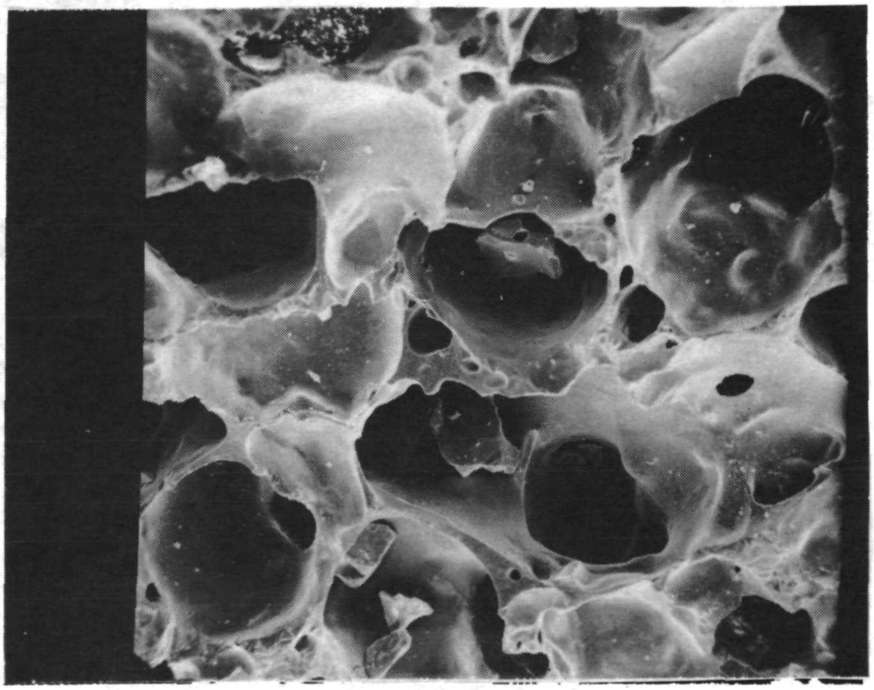

12 Wt. % CoO Additive (100X)

Fig. 15 Scanning Electron Microscope Photographs of Sintered Cenosphere Bodies Fired at 1650 K for One Hour

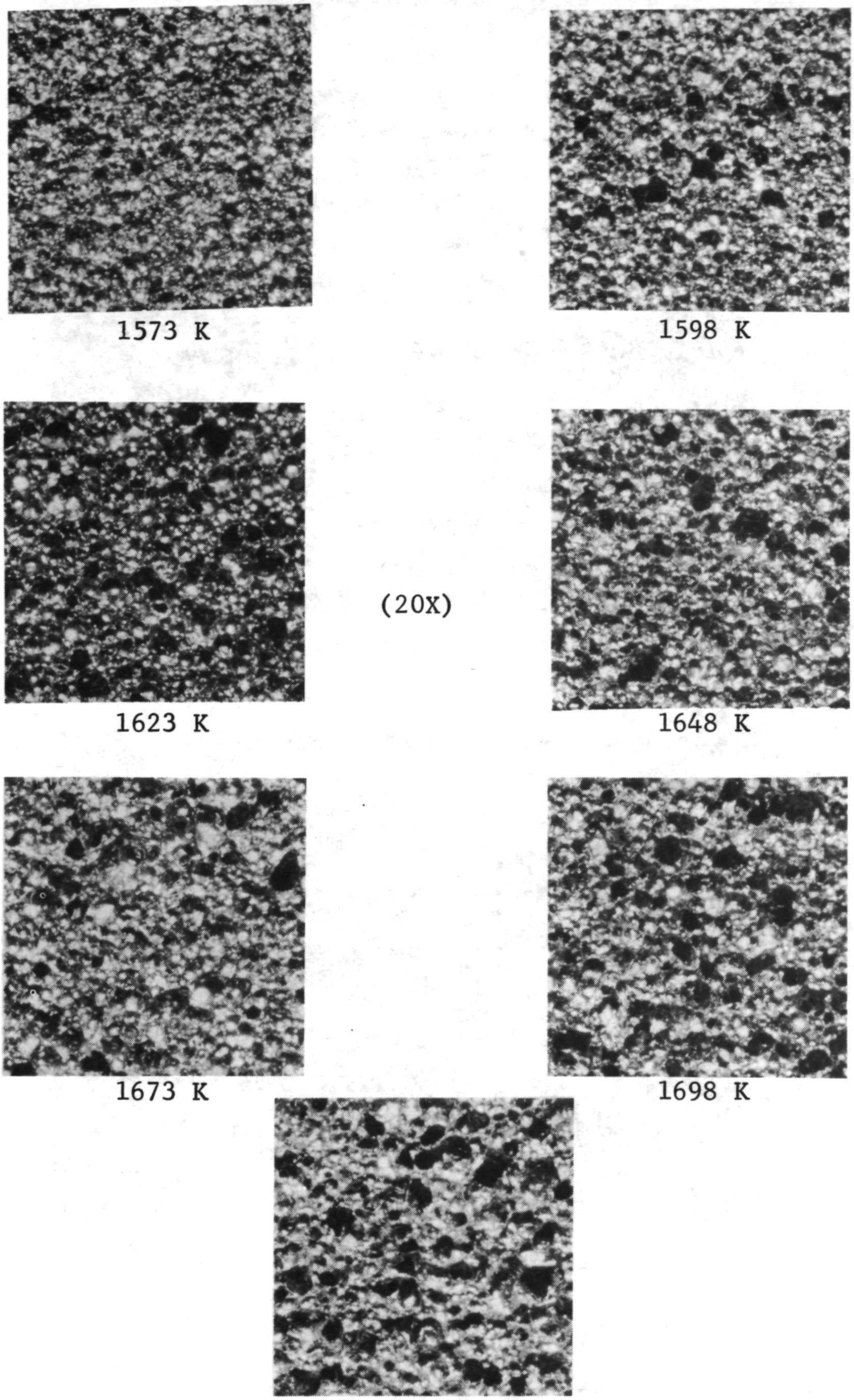

1573 K

1598 K

(20X)

1623 K

1648 K

1673 K

1698 K

1723 K

Fig. 16 Optical Micrographs Showing Effect of Temperature on Pore Sizes of CPI with Four-Weight-Percent CoO Additive (One Hour Heat Treatment)

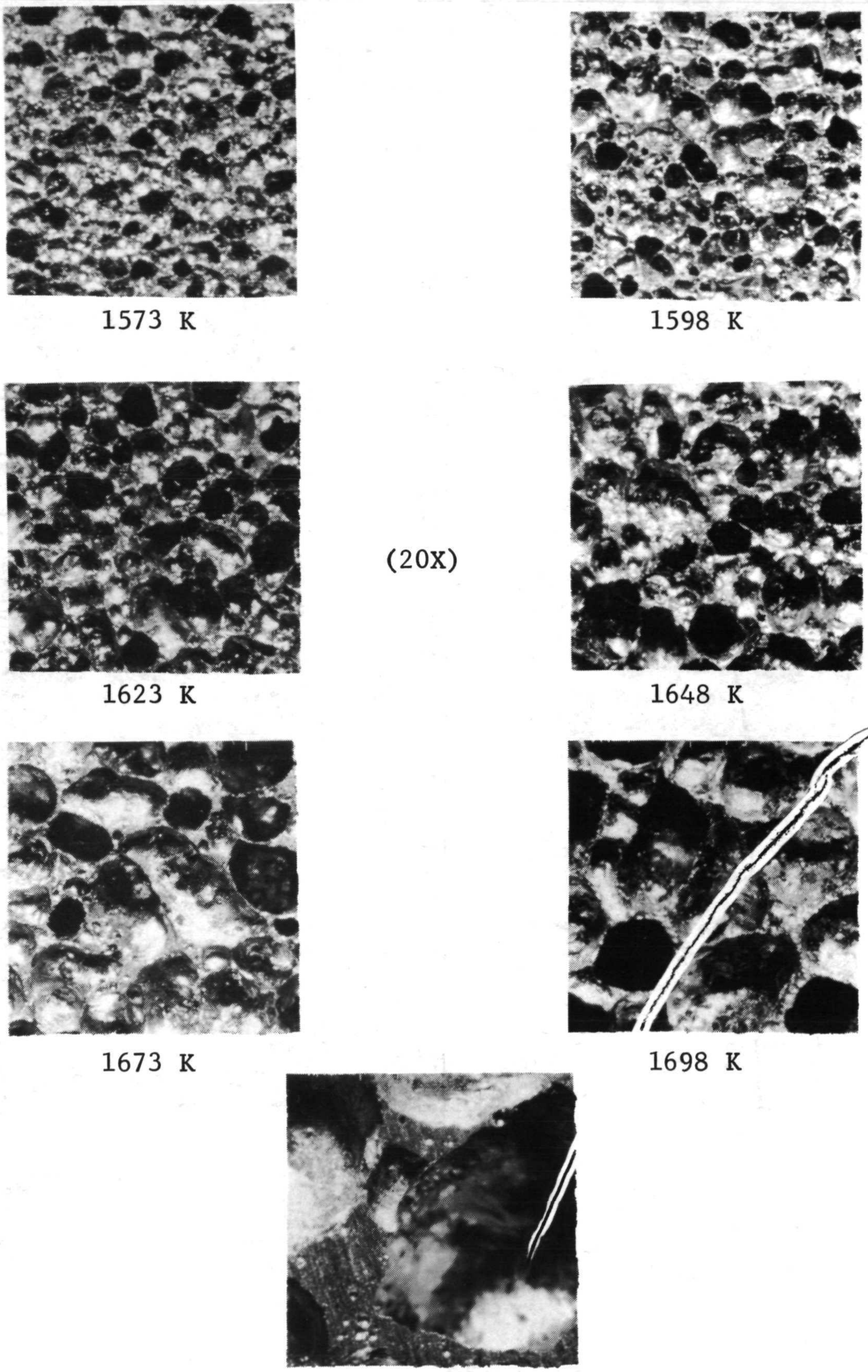

1573 K

1598 K

(20X)

1623 K

1648 K

1673 K

1698 K

1723 K

Fig. 17 Optical Micrographs Showing Effect of Temperature on Pore Sizes of CPI with Twelve-Weight- Percent CoO Additive (One Hour Heat Treatment)

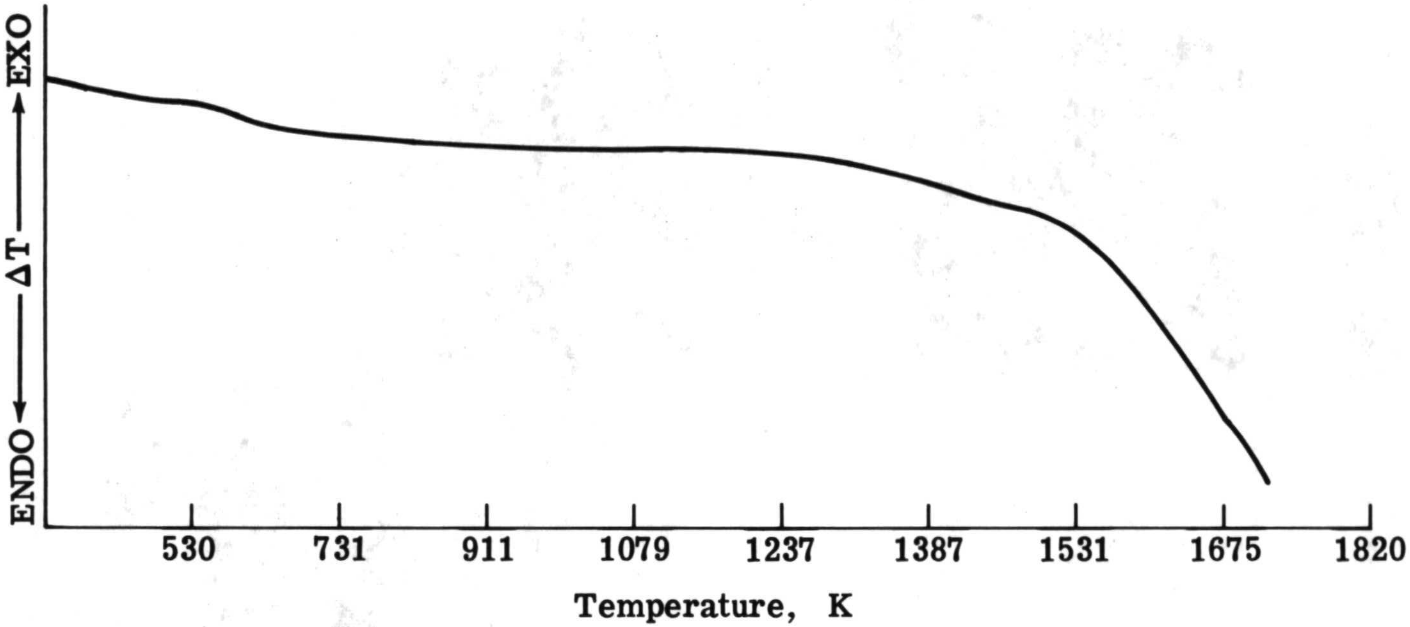

Note: Ordinate Scale Nonlinear

Fig. 18 Differential Thermal Analysis of Pure Sintered Cenospheres

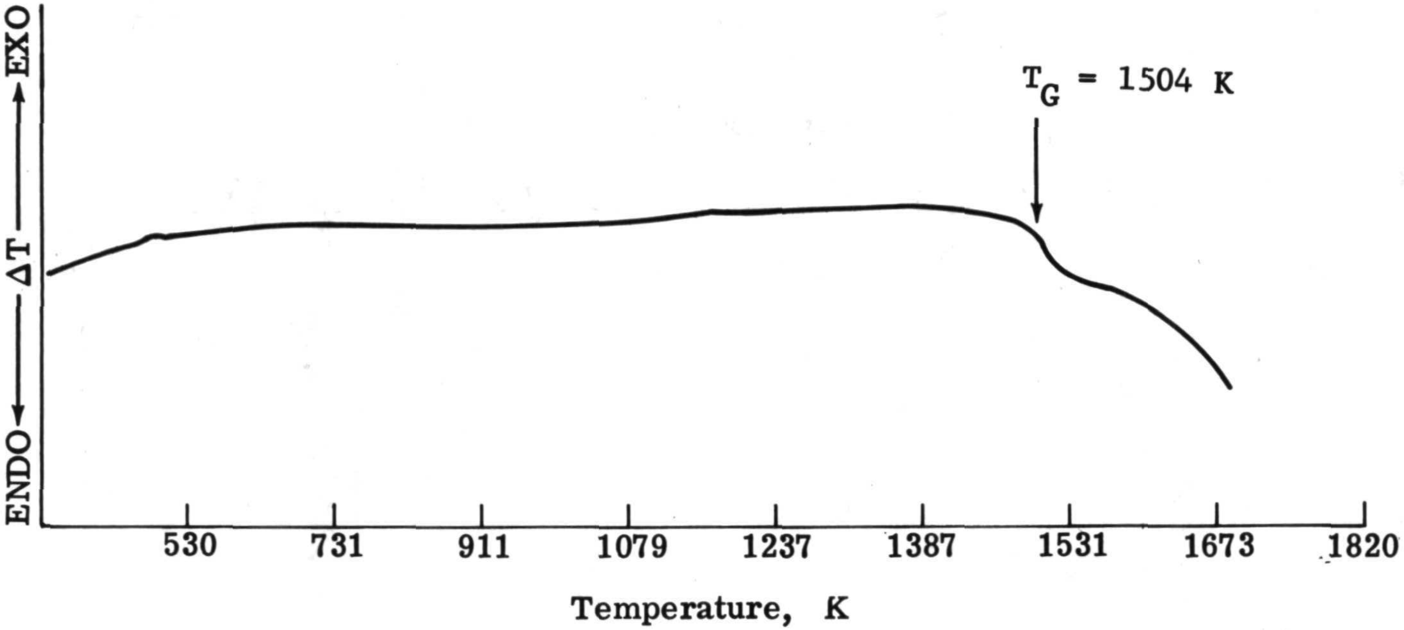

Note: Ordinate Scale Nonlinear

Fig. 19 Differential Thermal Analysis of Sintered Cenospheres with Four-Weight-Percent CoO Additive

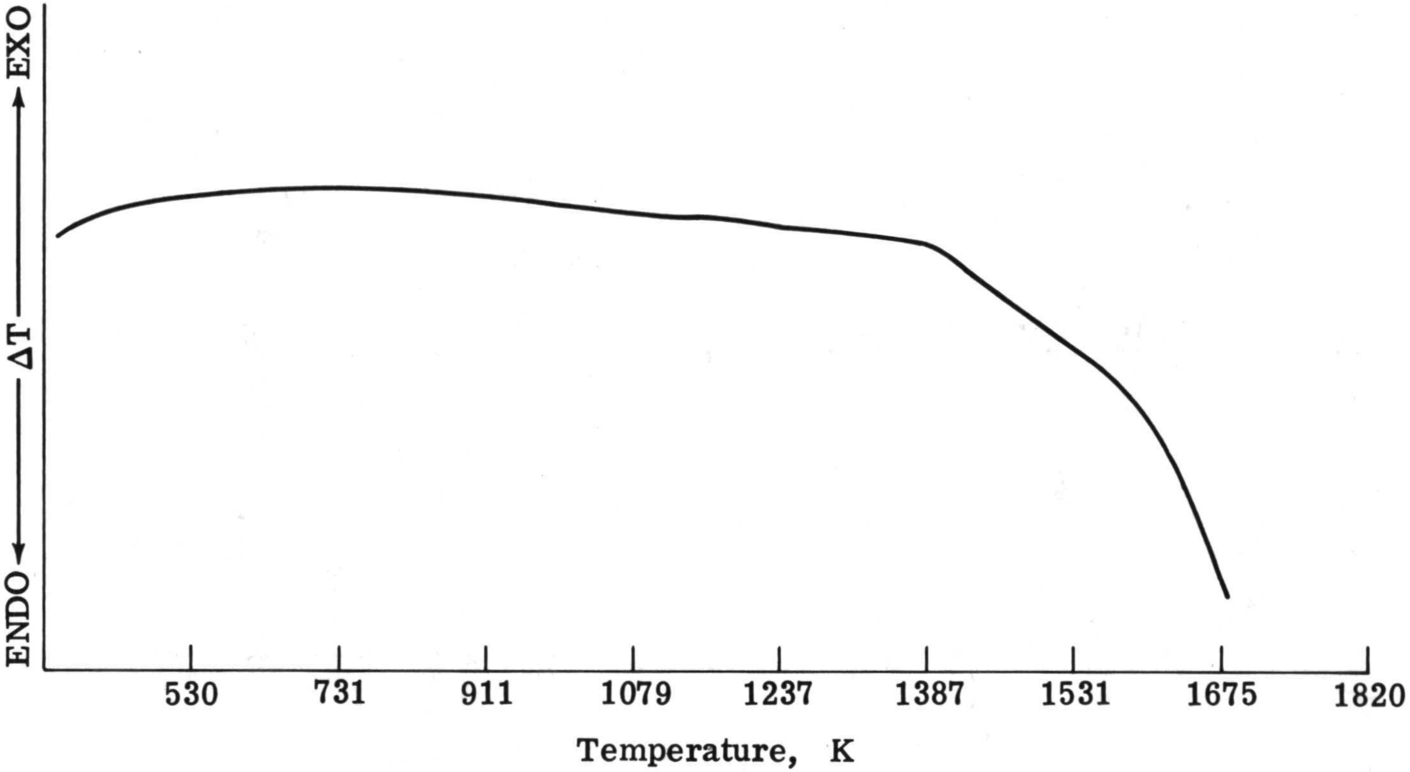

Note: Ordinate Scale Nonlinear

Fig. 20 Differential Thermal Analysis of Sintered Cenospheres with Twelve-Weight-Percent CoO Additive

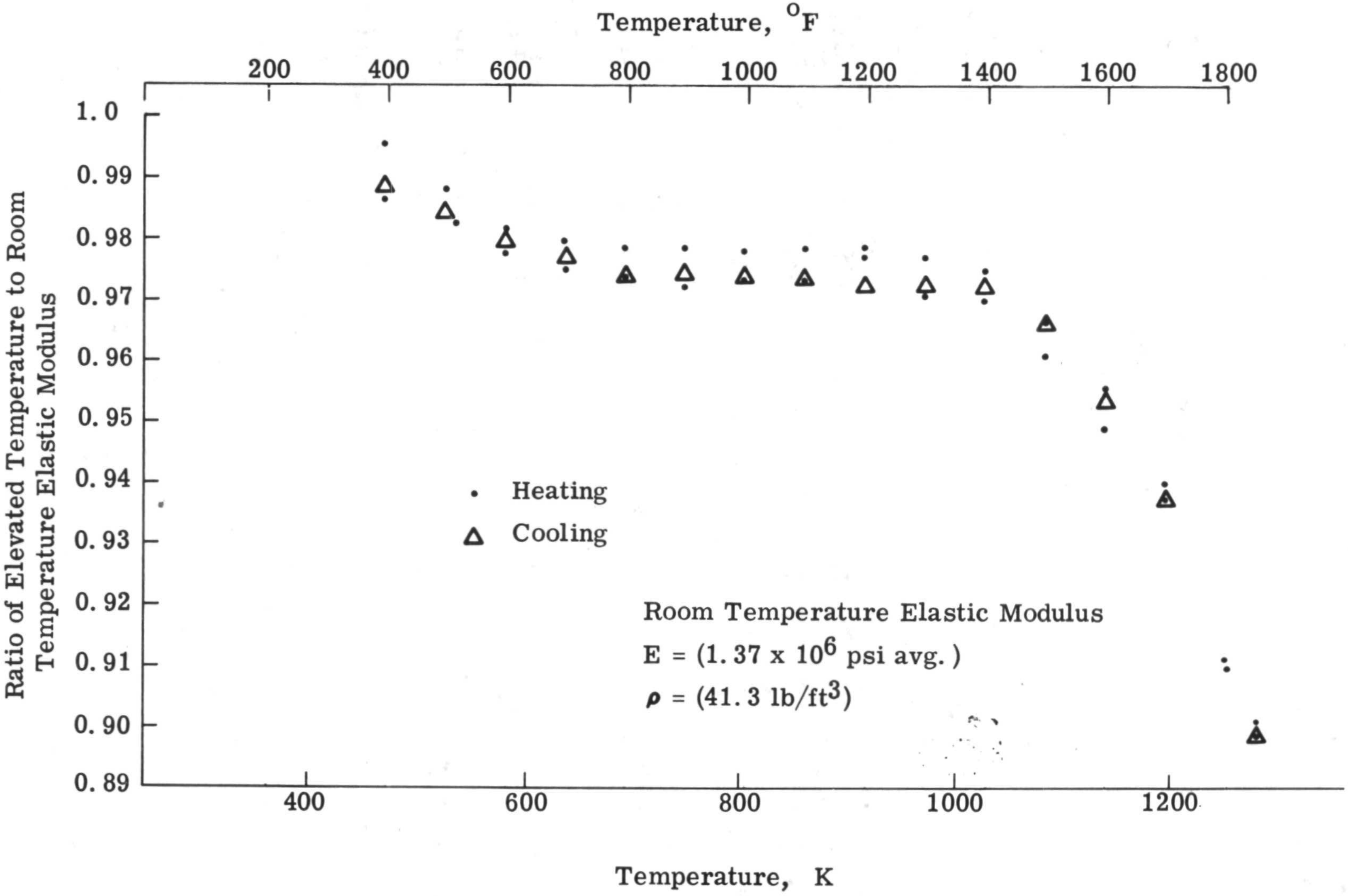

Fig. 21 Temperature Dependency of the Elastic Modulus of a Cenosphere Body with Twelve-Weight-Percent CoO Additive

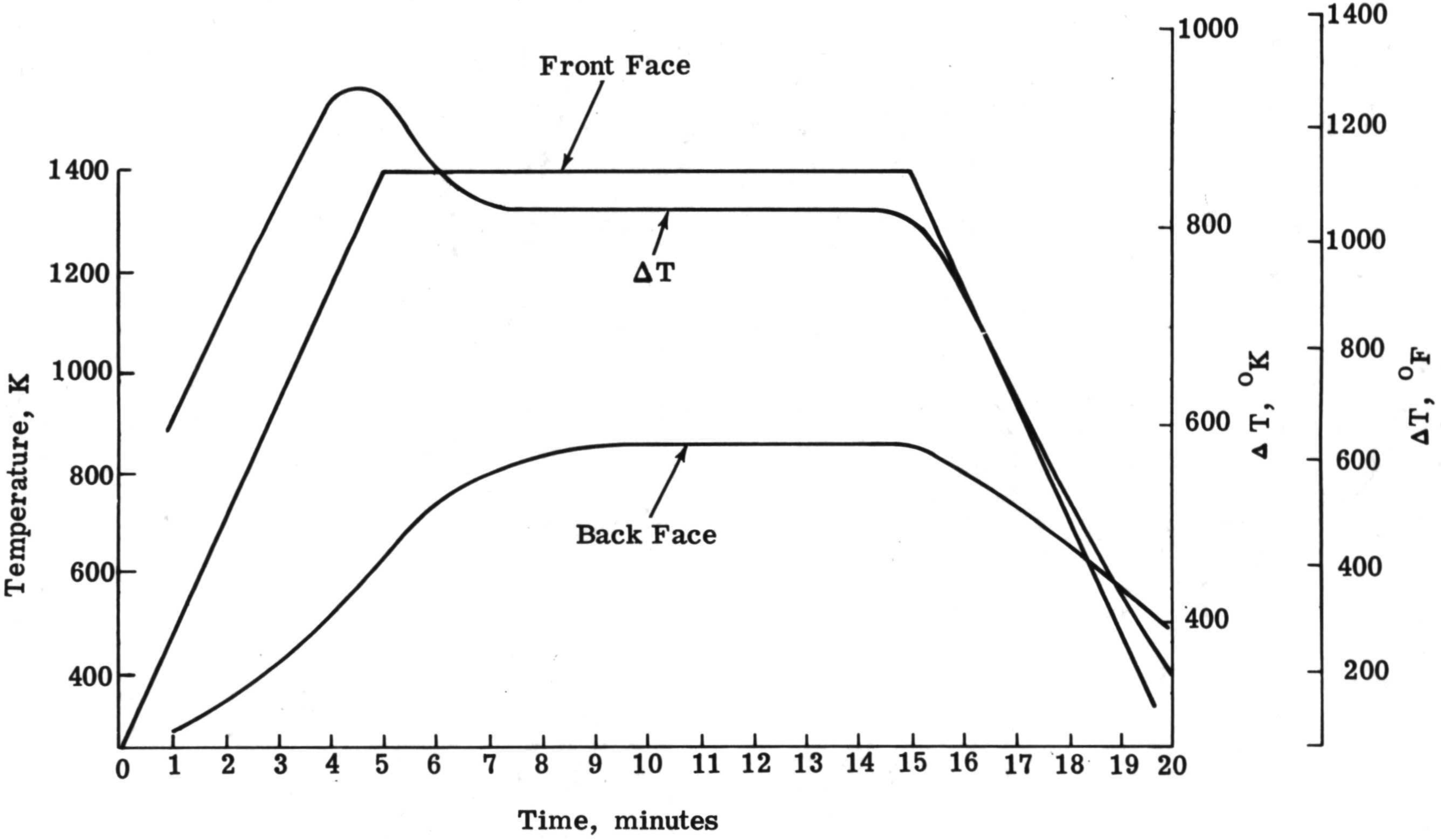

Fig. 22 Typical Time-Temperature Profile Showing Temperature Drop Across a 1cm-Thick CPI Plate with Twelve-Weight-Percent CoO Additive (Uninsulated Back Face)

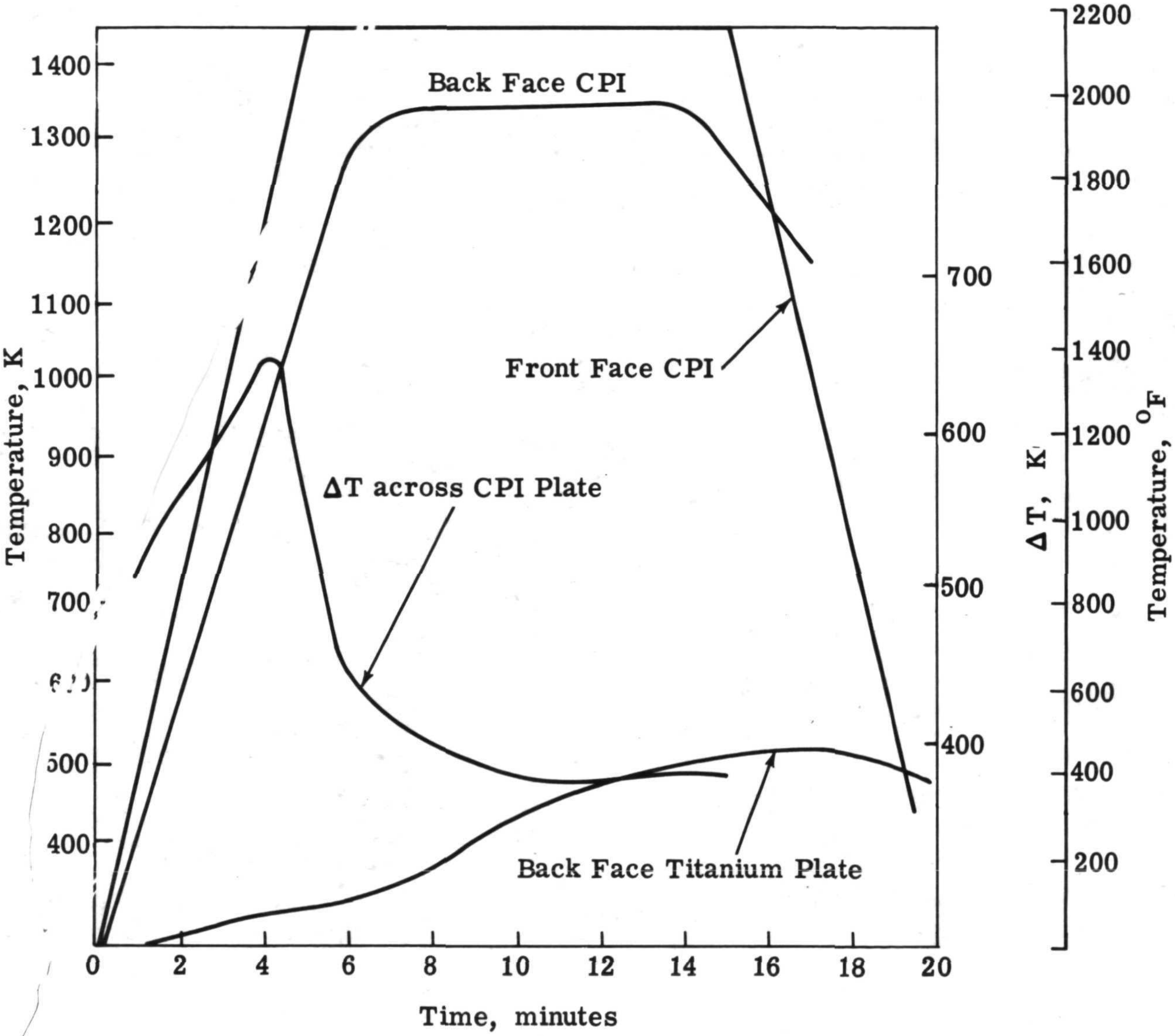

Fig. 23 Simulated Re-entry Temperature Profile for a 1cm-Thick CPI Plate Backed by 0.038m of Microquartz Supported on a Titanium Plate

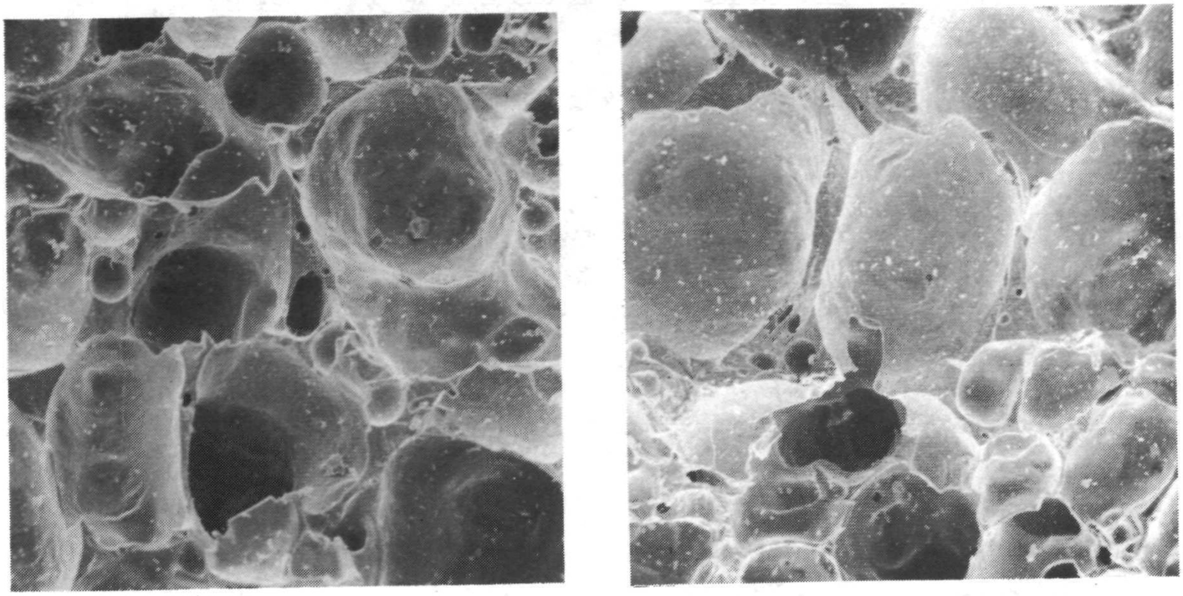

Sample R-1 (90X~ Sample R-3 (90X)

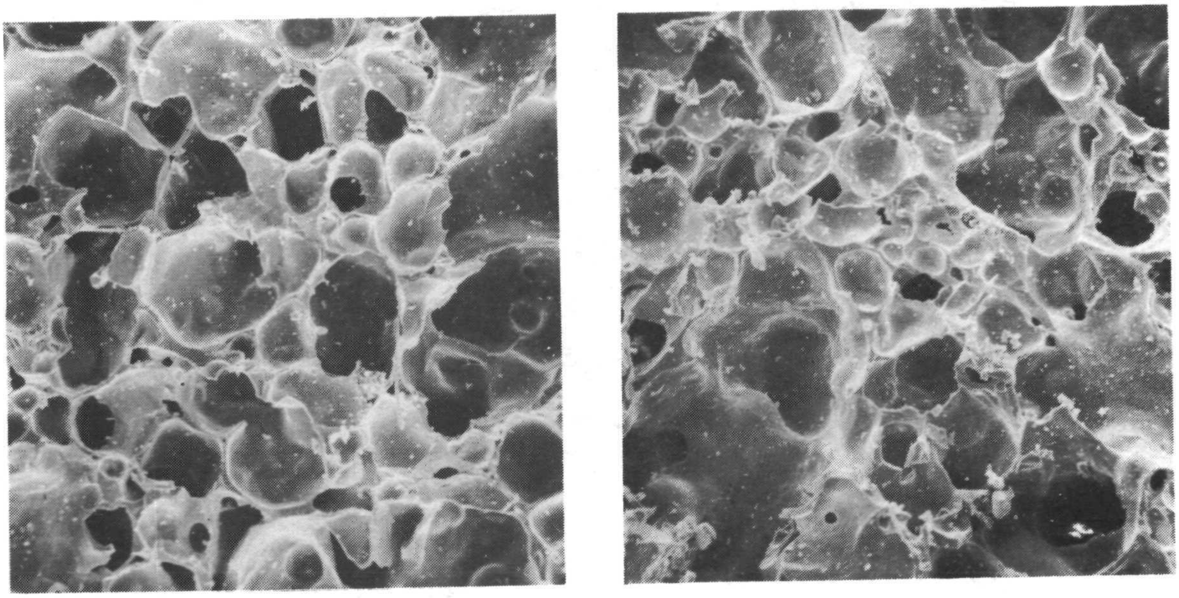

Sample S-4 (100X) Sample S-5 (90X)

Fig. 24 Scanning Electron Microscope Photographs of R- and S-Series Scaled-Up CPI Tiles

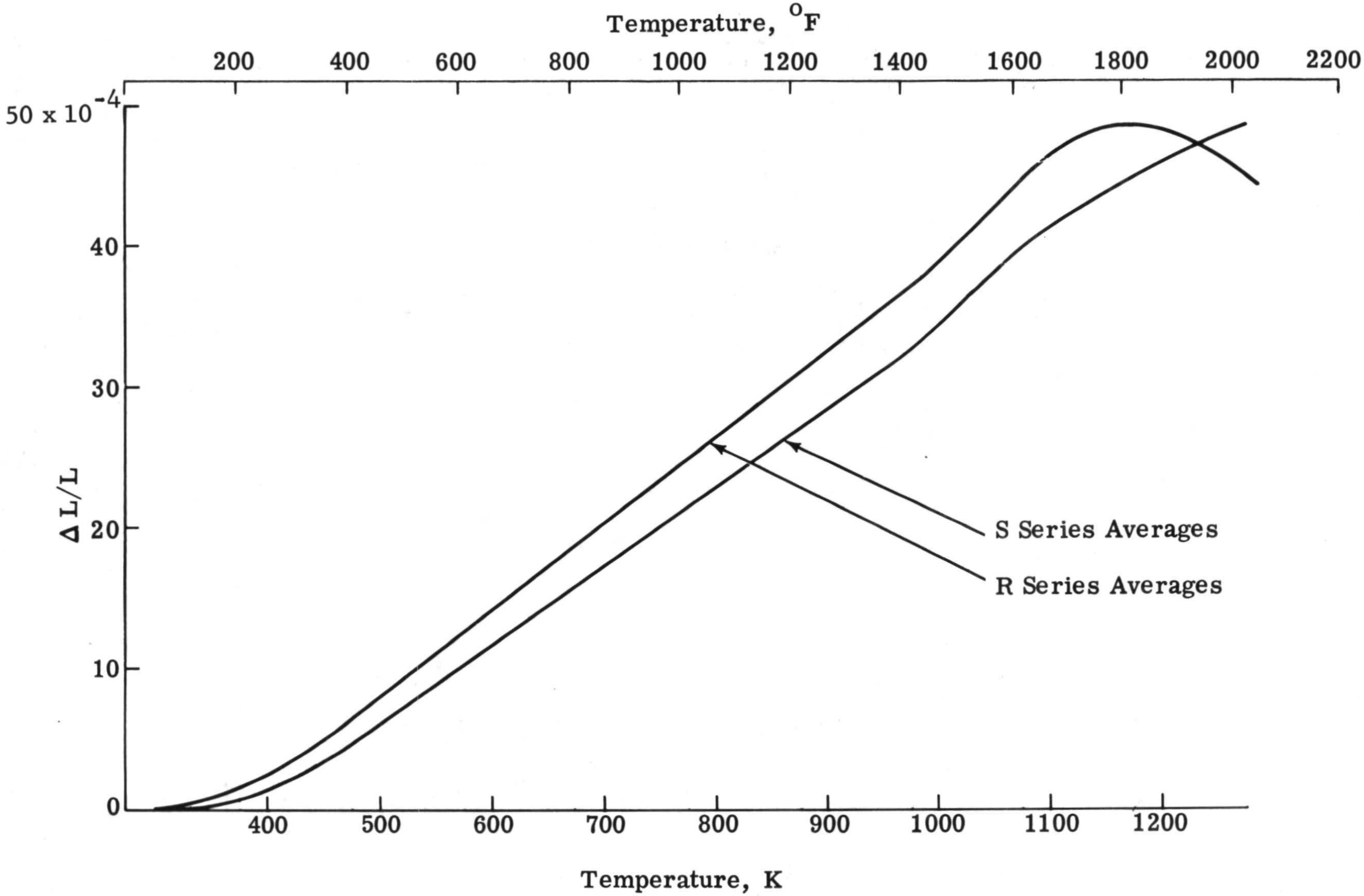

Fig. 25 Thermal Expansion of Sintered, Scaled-Up R- and S-Series CPI Tiles

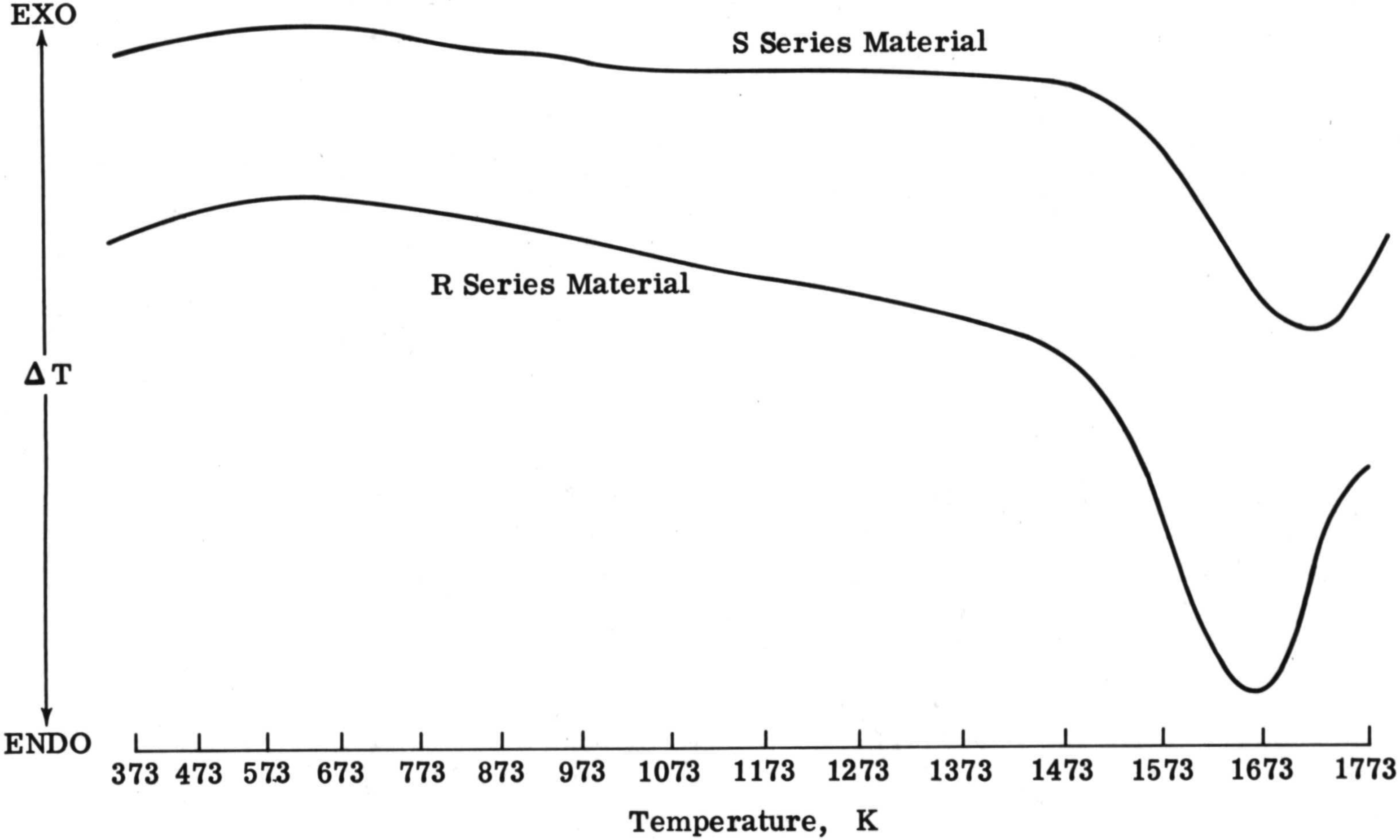

Note: Ordinate Scale Nonlinear

Fig. 26 Differential Thermal Analysis Traces of Scaled-Up R- and S-Series CPI Tiles

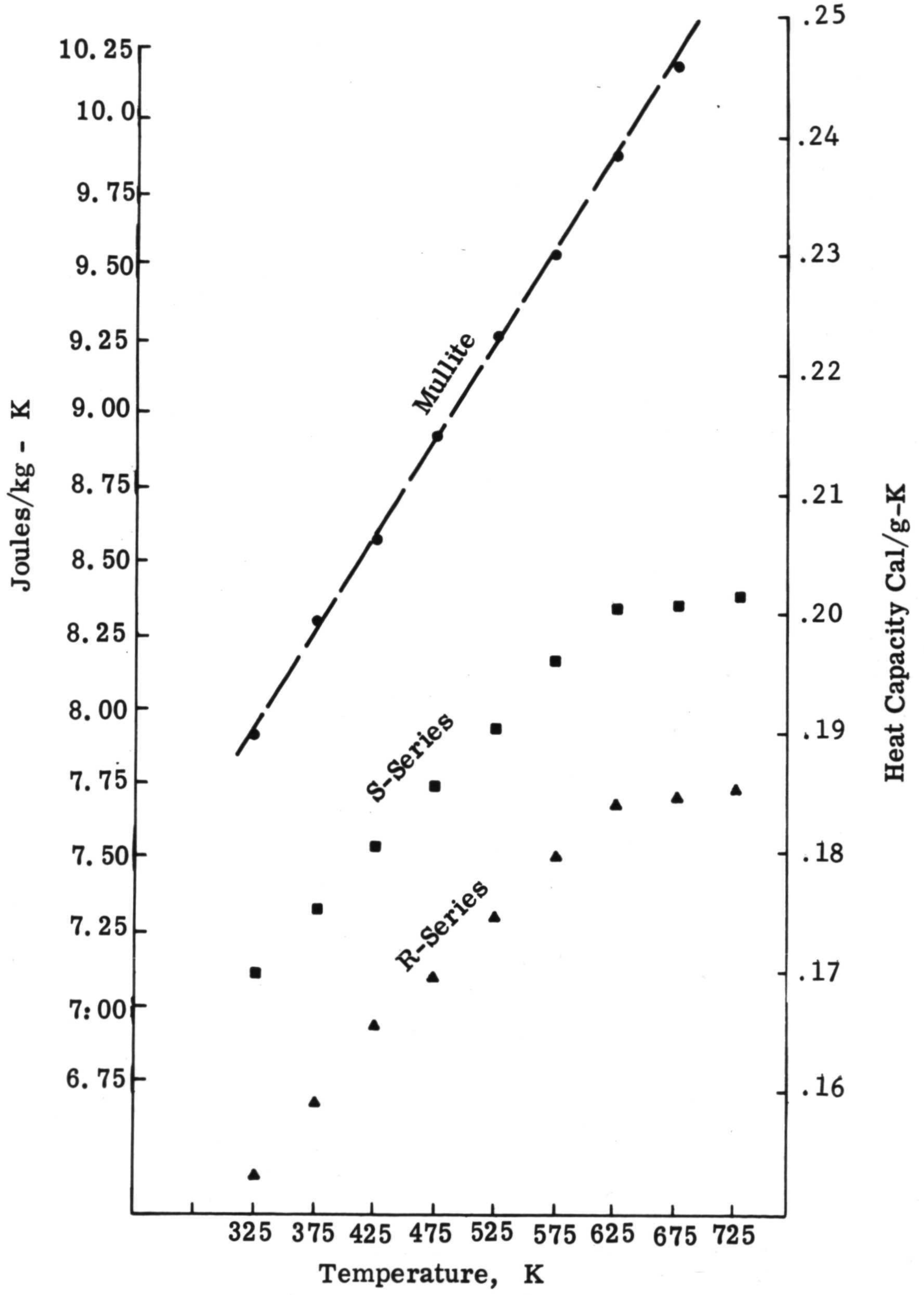

Fig. 27 Heat Capacity versus Temperature of Scaled-Up CPI Tiles (R- and S-Series Samples and Mullite)

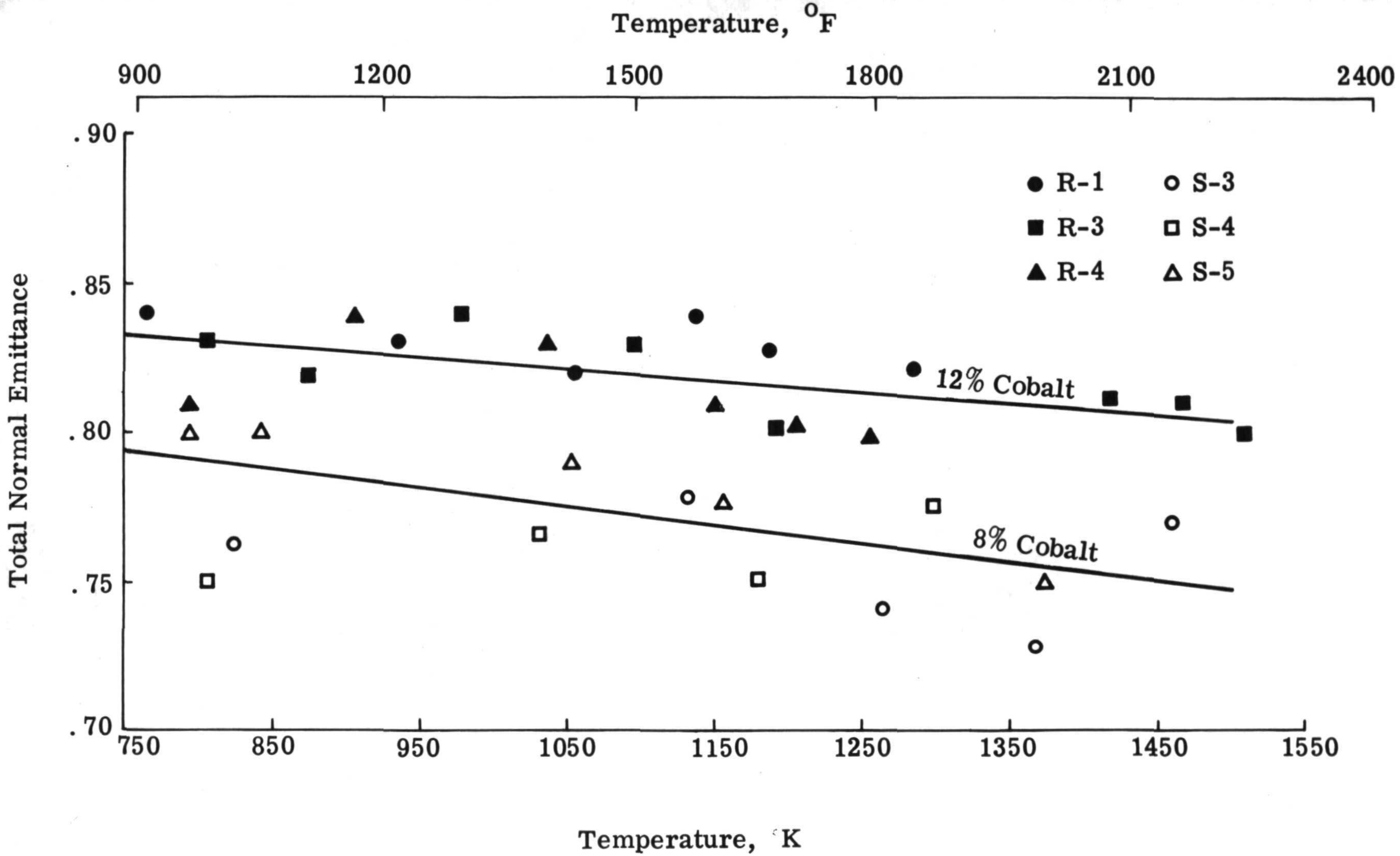

Fig. 28 Total Normal Emittance versus Temperature of Scaled-Up R- and S-Series CPI Tiles

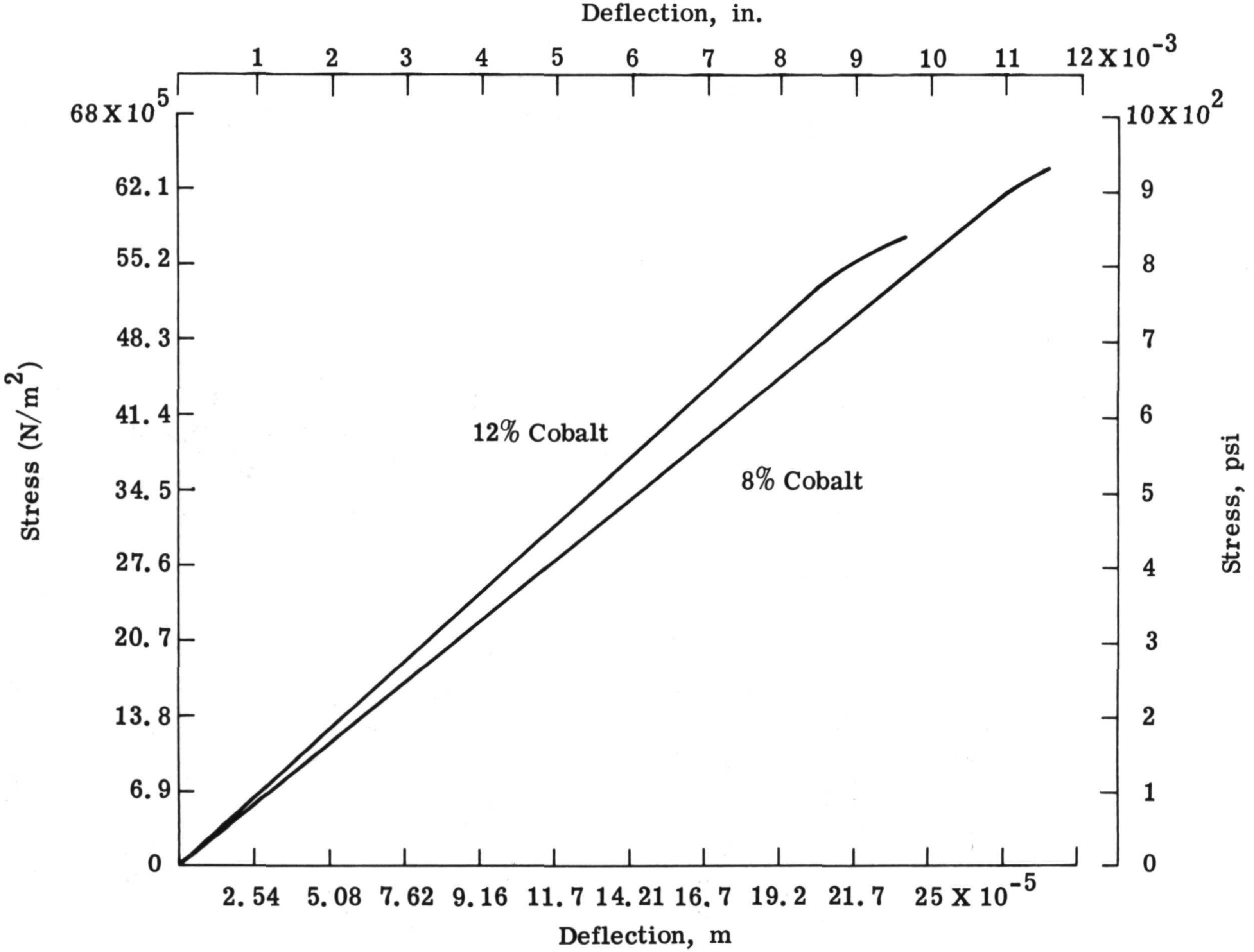

Fig. 29 Stress-Deflection Curve for Single-Point Loaded Flexure Specimen

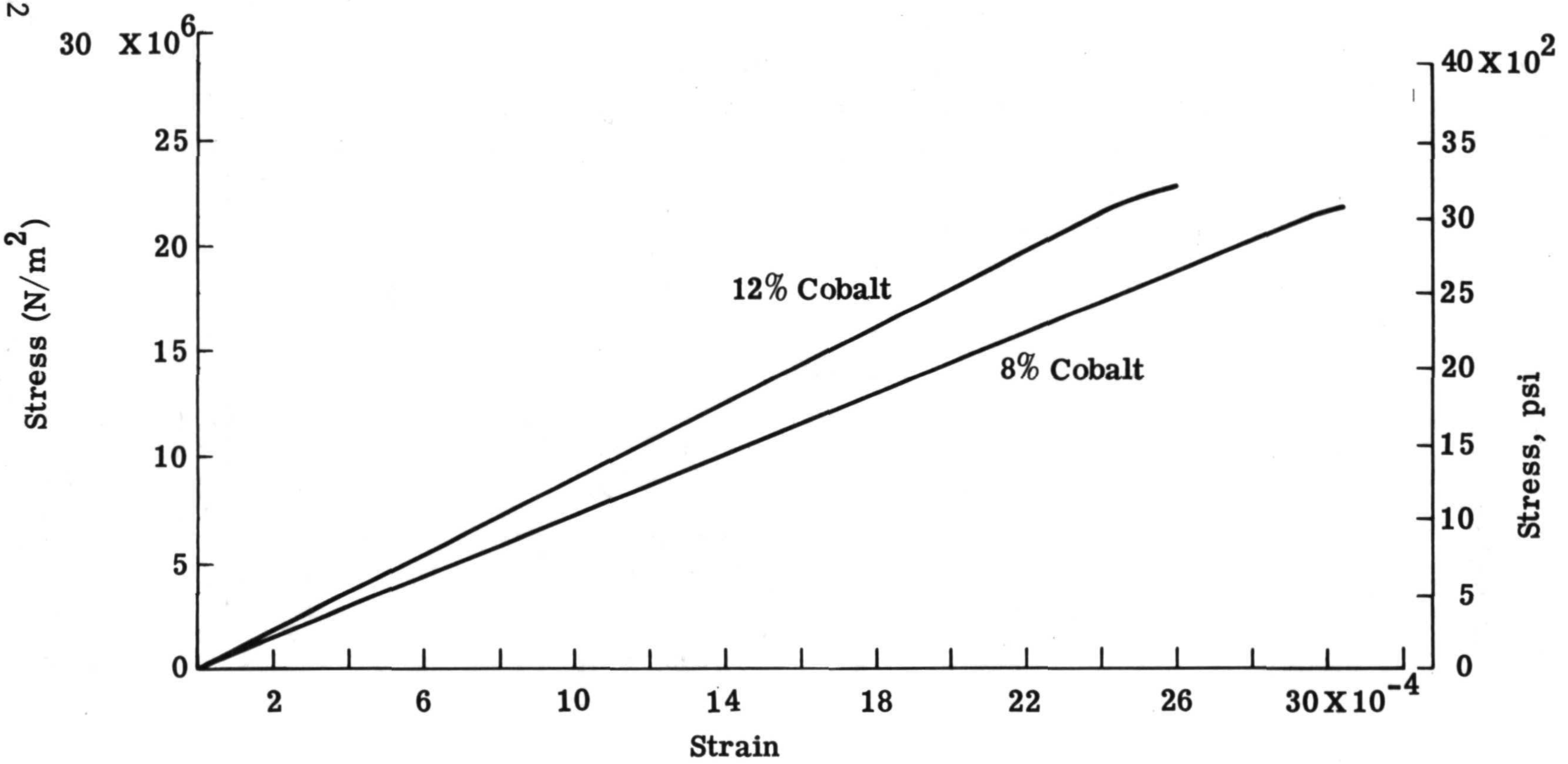

Fig. 30 Stress-Strain Curve of R- and S-Series CPI Specimens Edgewise Compression Loaded

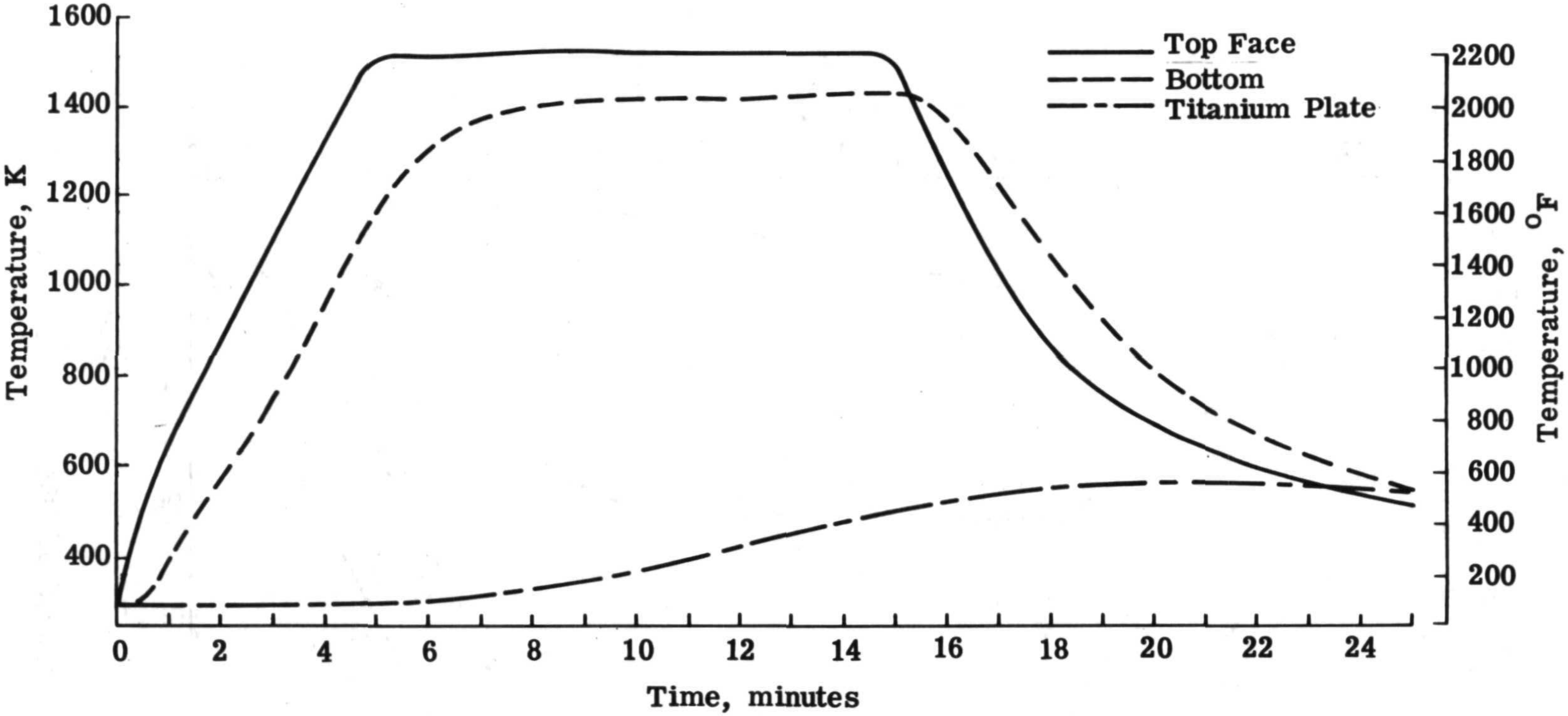

Fig. 31 Typical Re-entry Profile for a Scaled-Up CPI Specimen Containing Eight-Weight-Percent CoO Additive

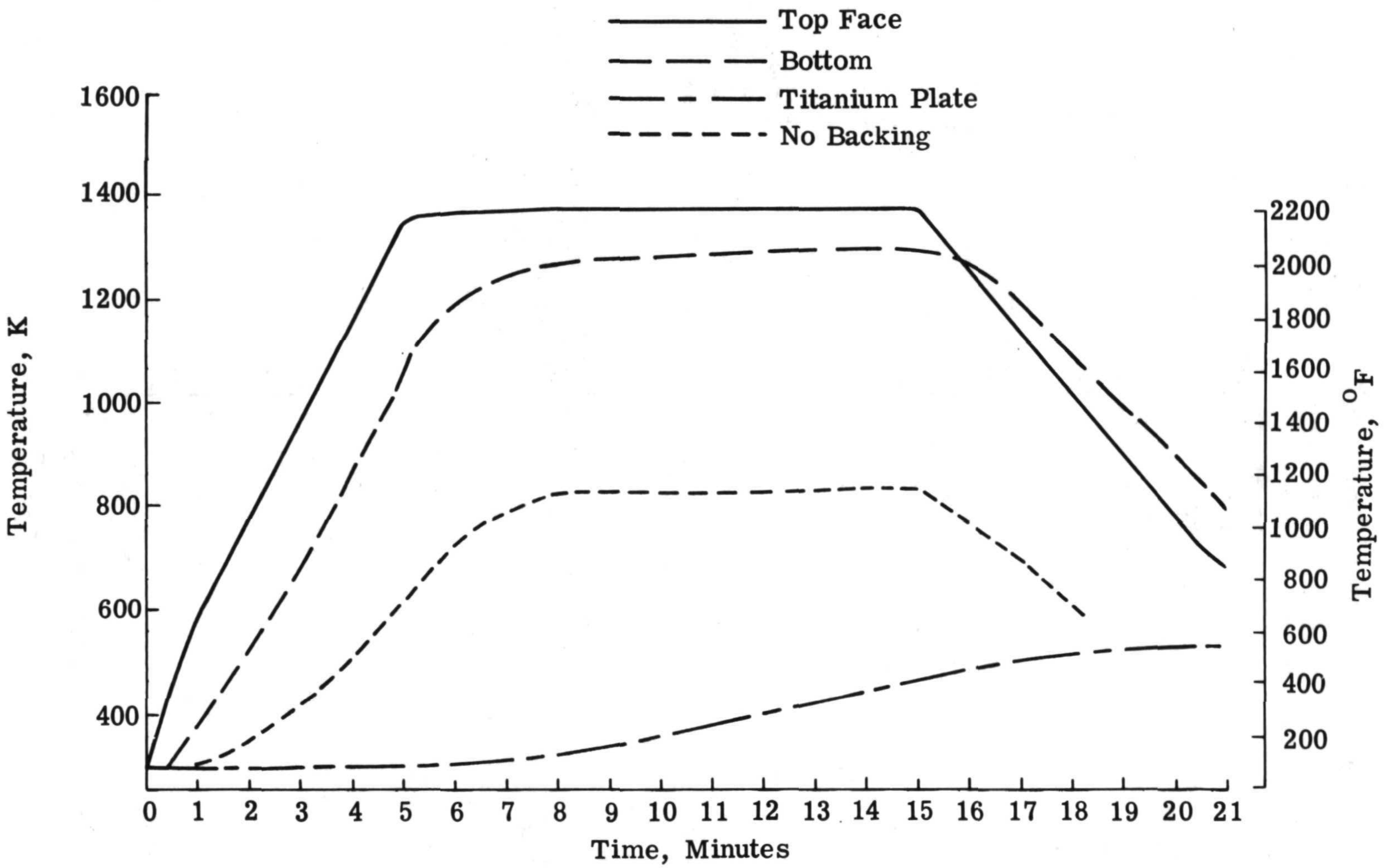

Fig. 32 Typical Re-entry Profile for a Scaled-Up CPI Specimen Containing Twelve-Weight-Percent CoO Additive

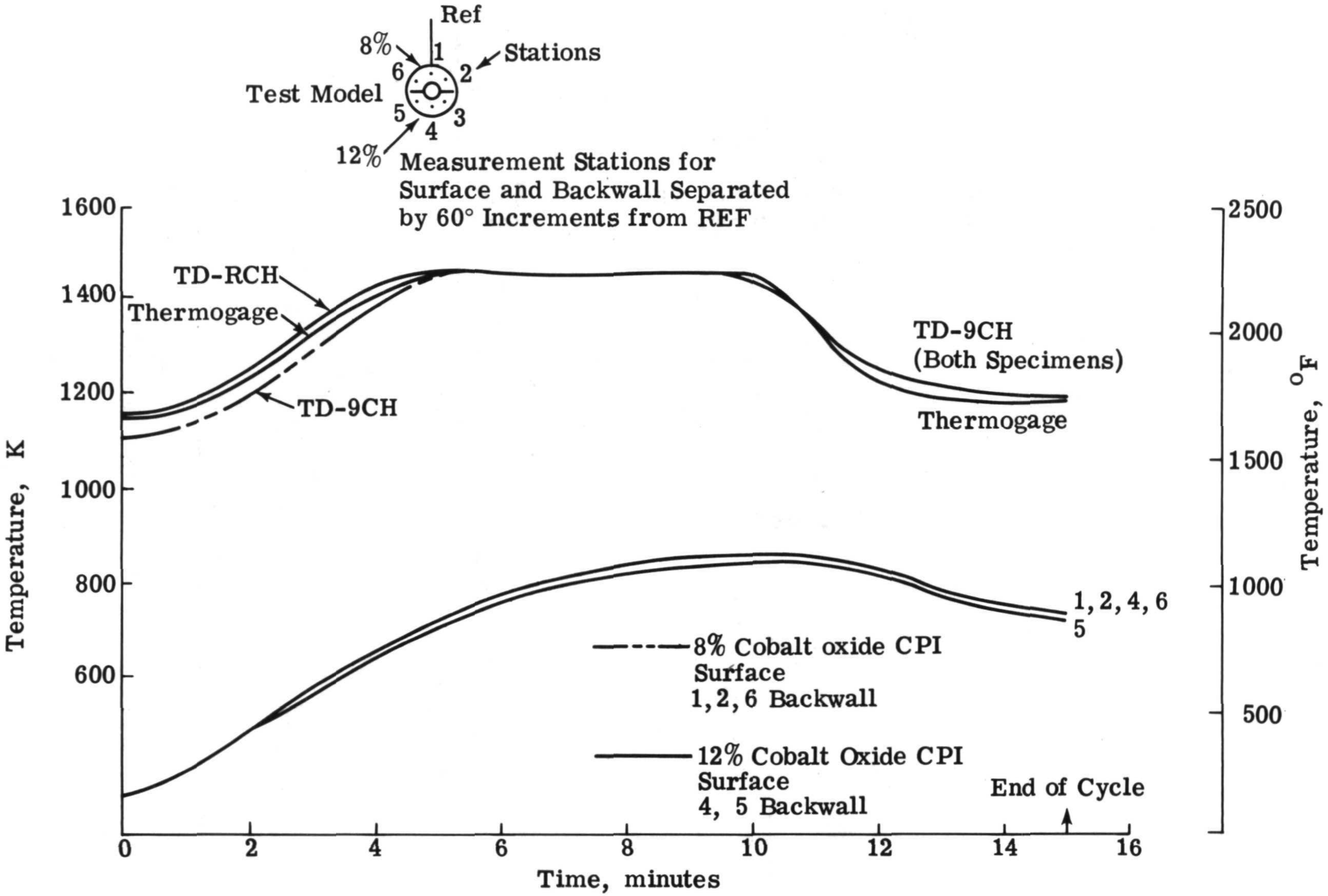

Fig. 33 Typical Surface and Back Face Temperature Response of a CPI Specimen in the Plasma Arc Jet

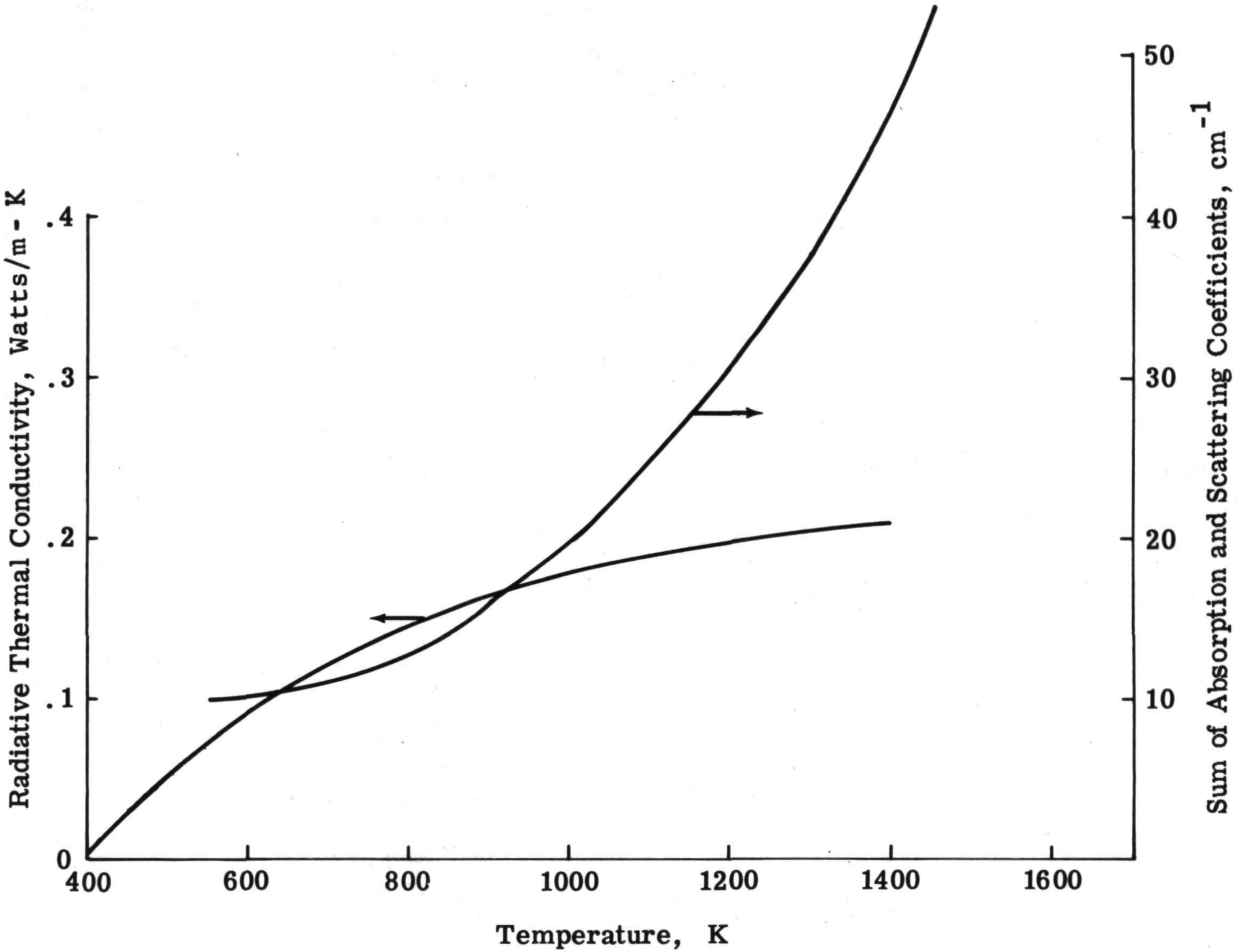

Fig. 34 Radiative Thermal Conductivity and Absorption and Scattering Coefficients versus Temperature in CPI Specimens

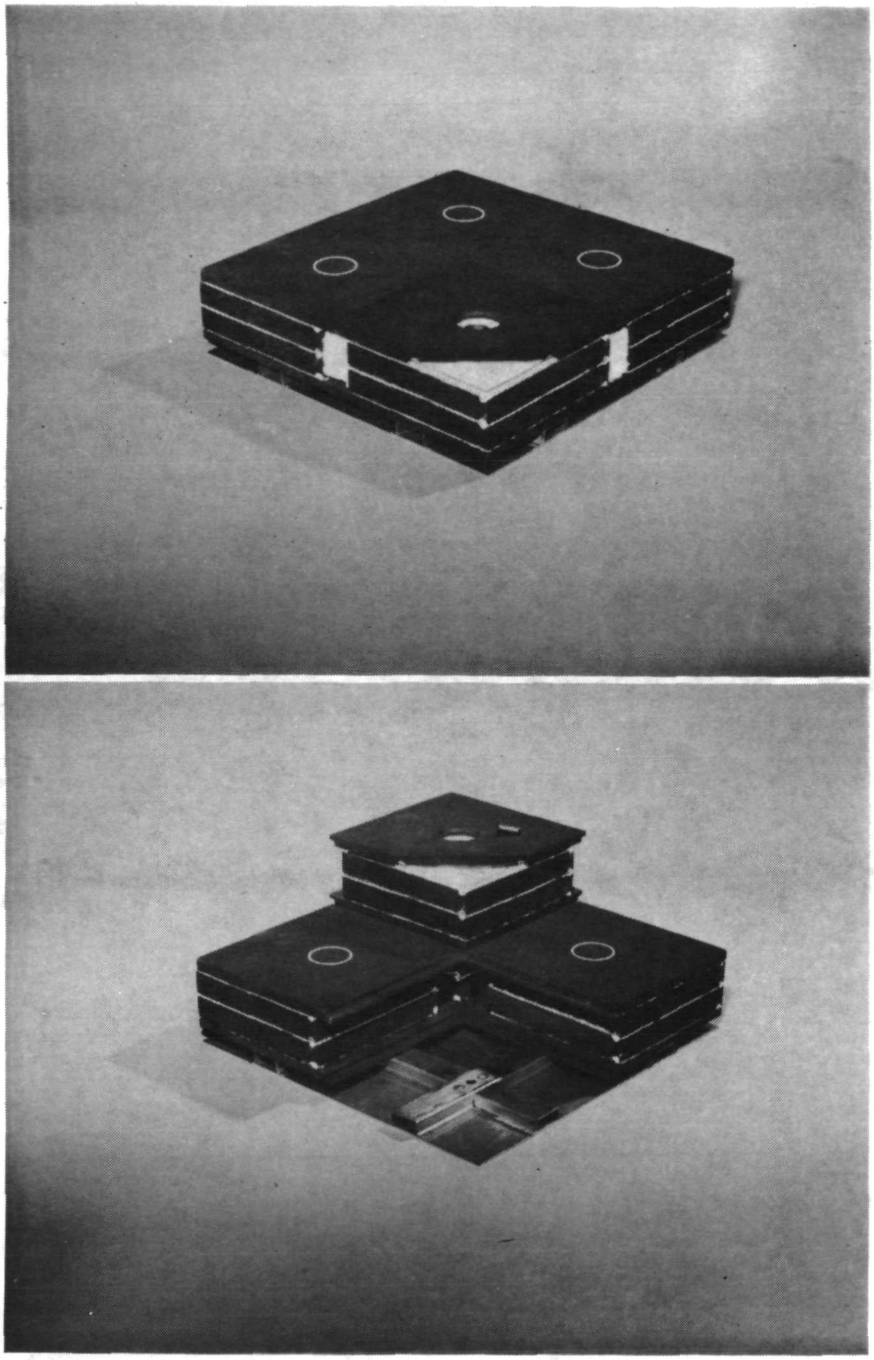

Fig. 35 Composite CPI Heat Shield Showing Joints, Attachments, and Primary Structure

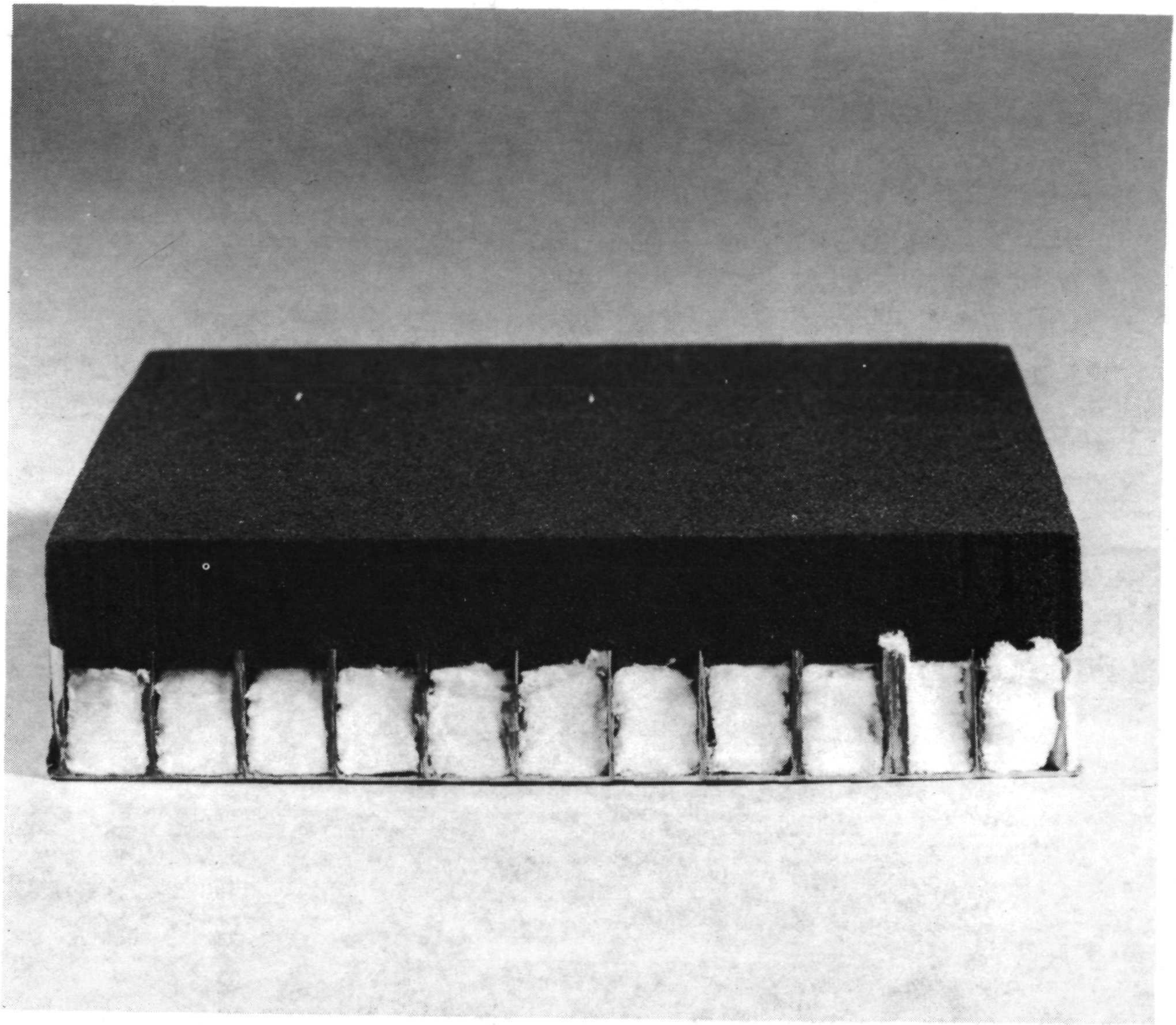

Fig. 36 Composite CPI Heat Shield Showing CPI Embedded into Fiber-Filled Honeycomb

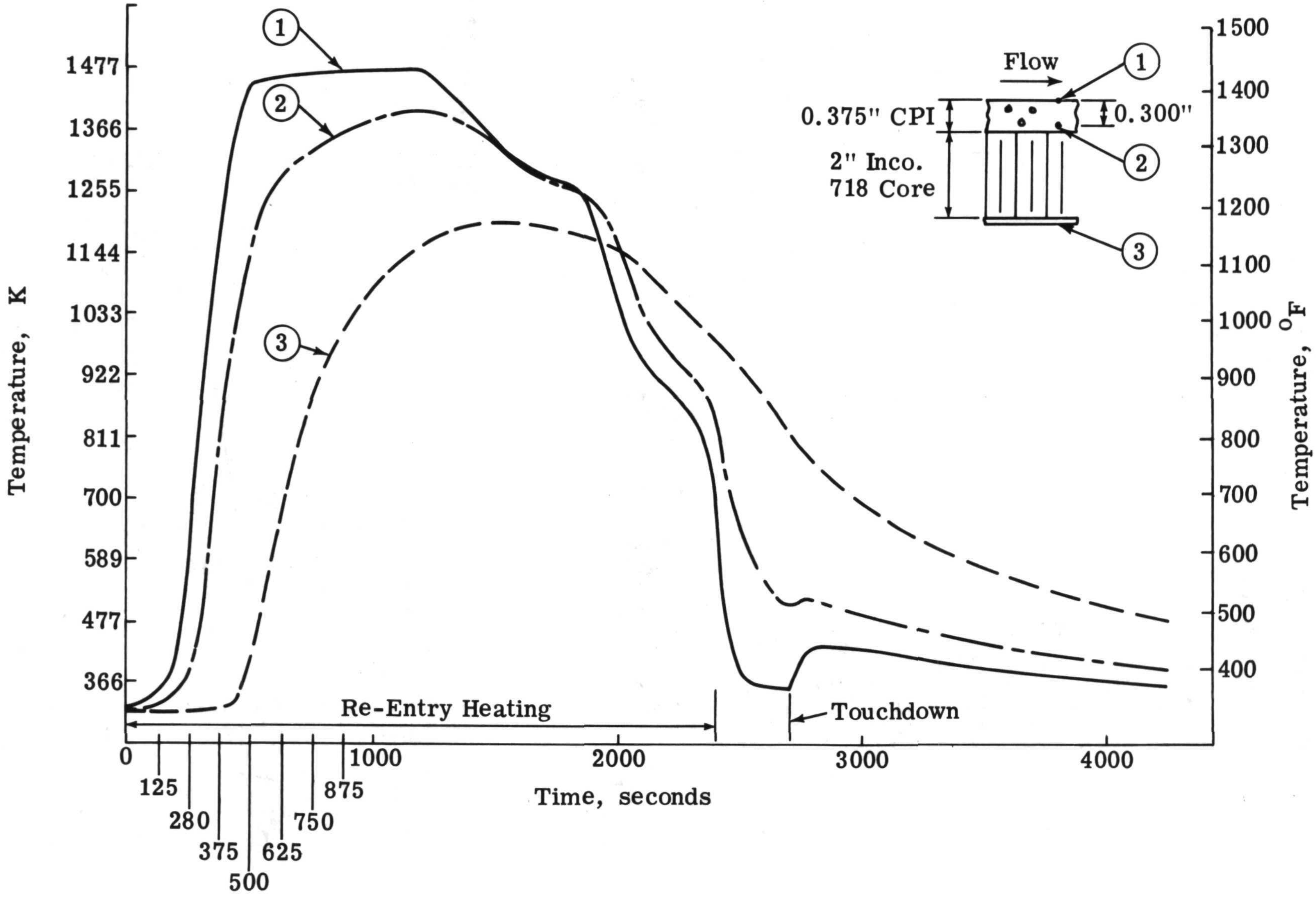

Fig. 37 Temperature Response of a CPI-Inconel 718 Panel where the CPI Plate is 1cm Thick

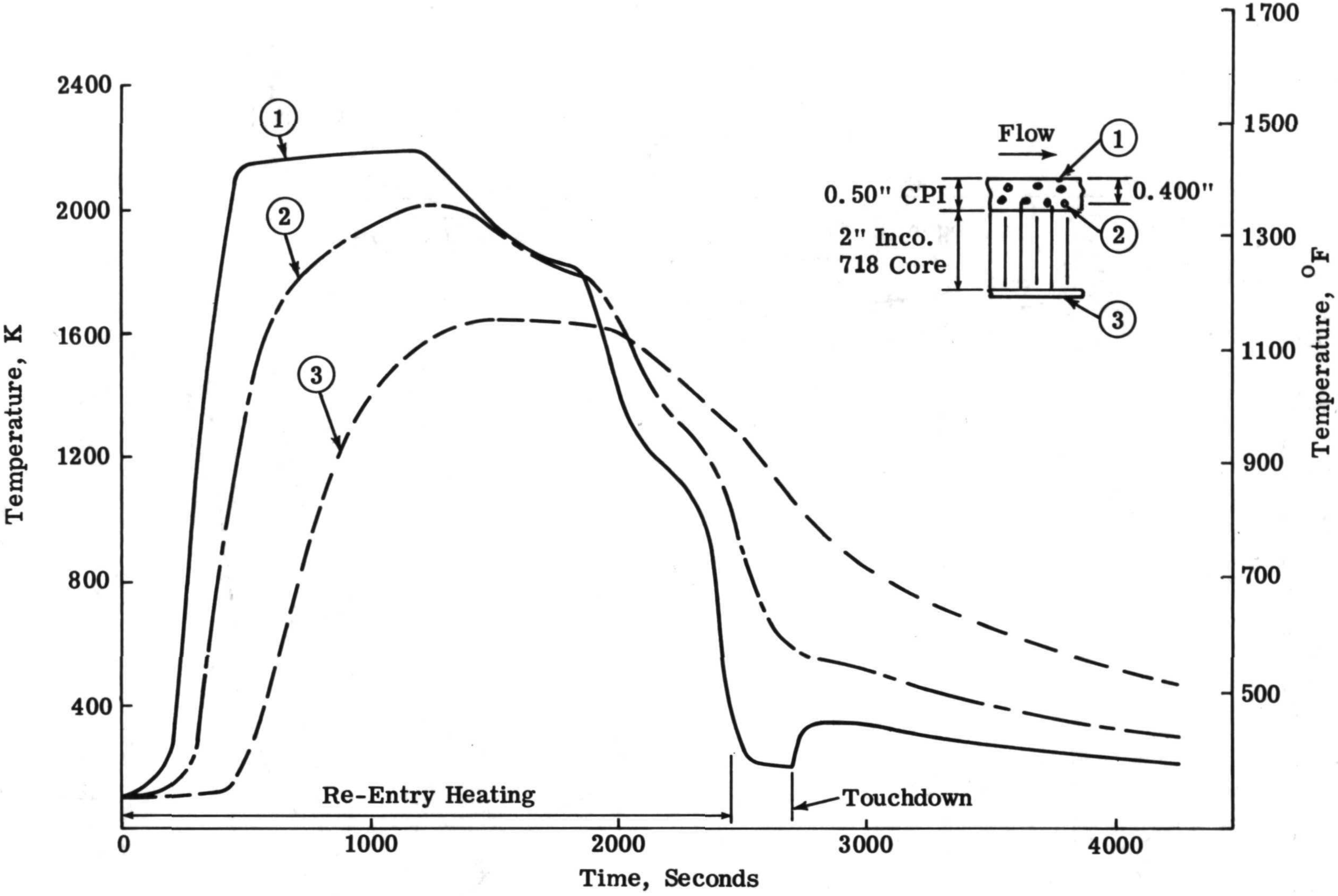

Fig. 38 Temperature Response of a CPI-Inconel 718 Panel where the CPI Plate Is 1.27cm Thick

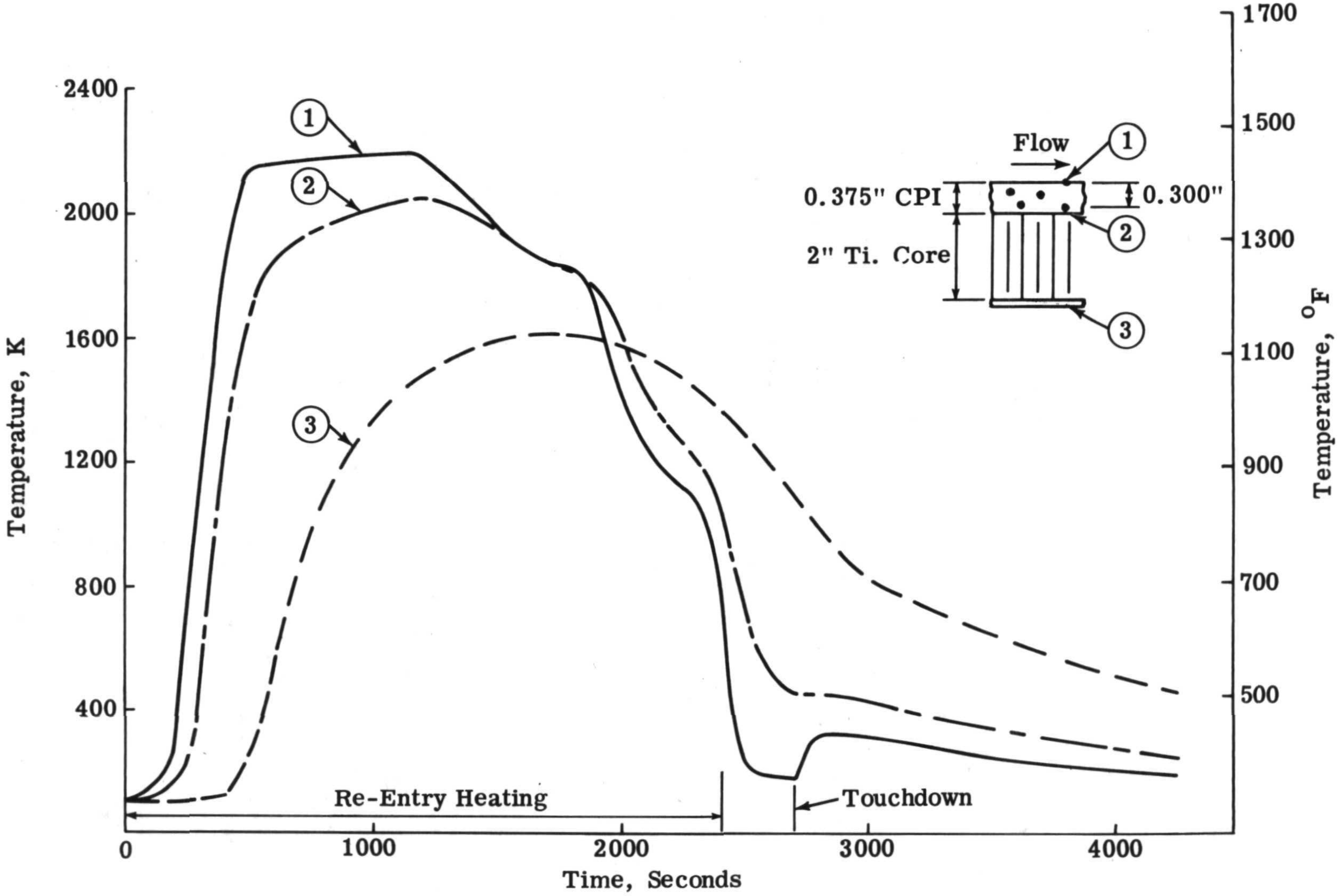

Fig. 39 Temperature Response of a CPI-Titanium Panel where the CPI Plate Is 1cm Thick

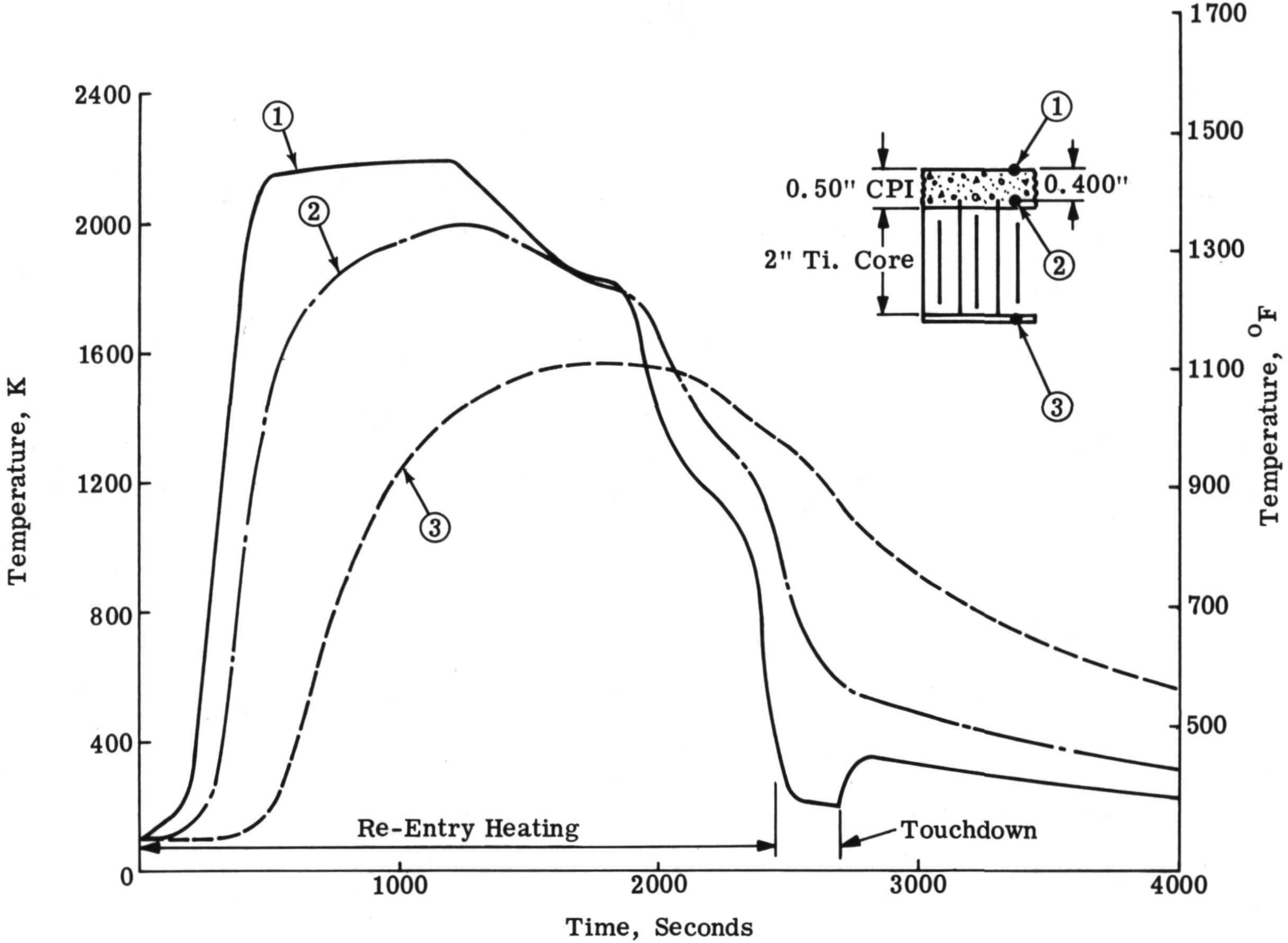

Fig. 40 Temperature Response of a CPI-Titanium Panel where the CPI Plate Is 1.27cm Thick

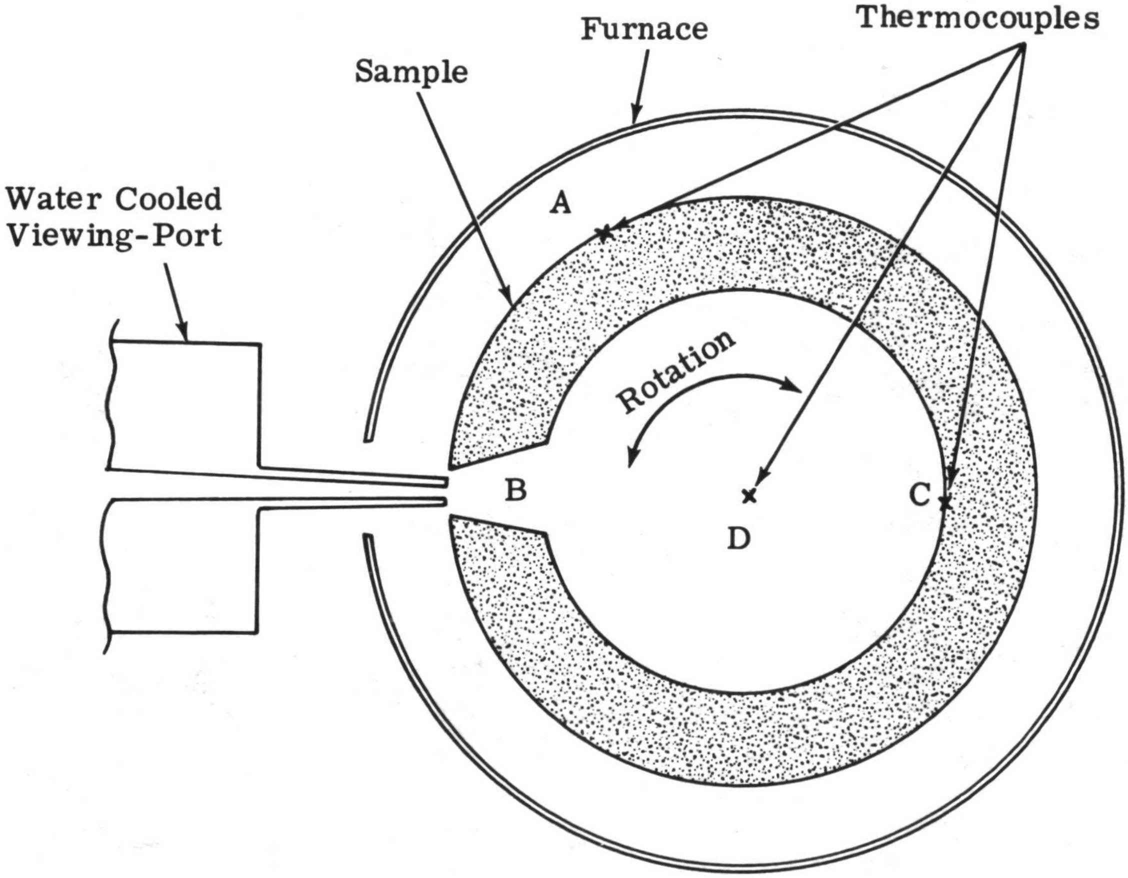

Fig. 41 Cross Section of Rotating Specimen Furnace Used for Emittance Measurements

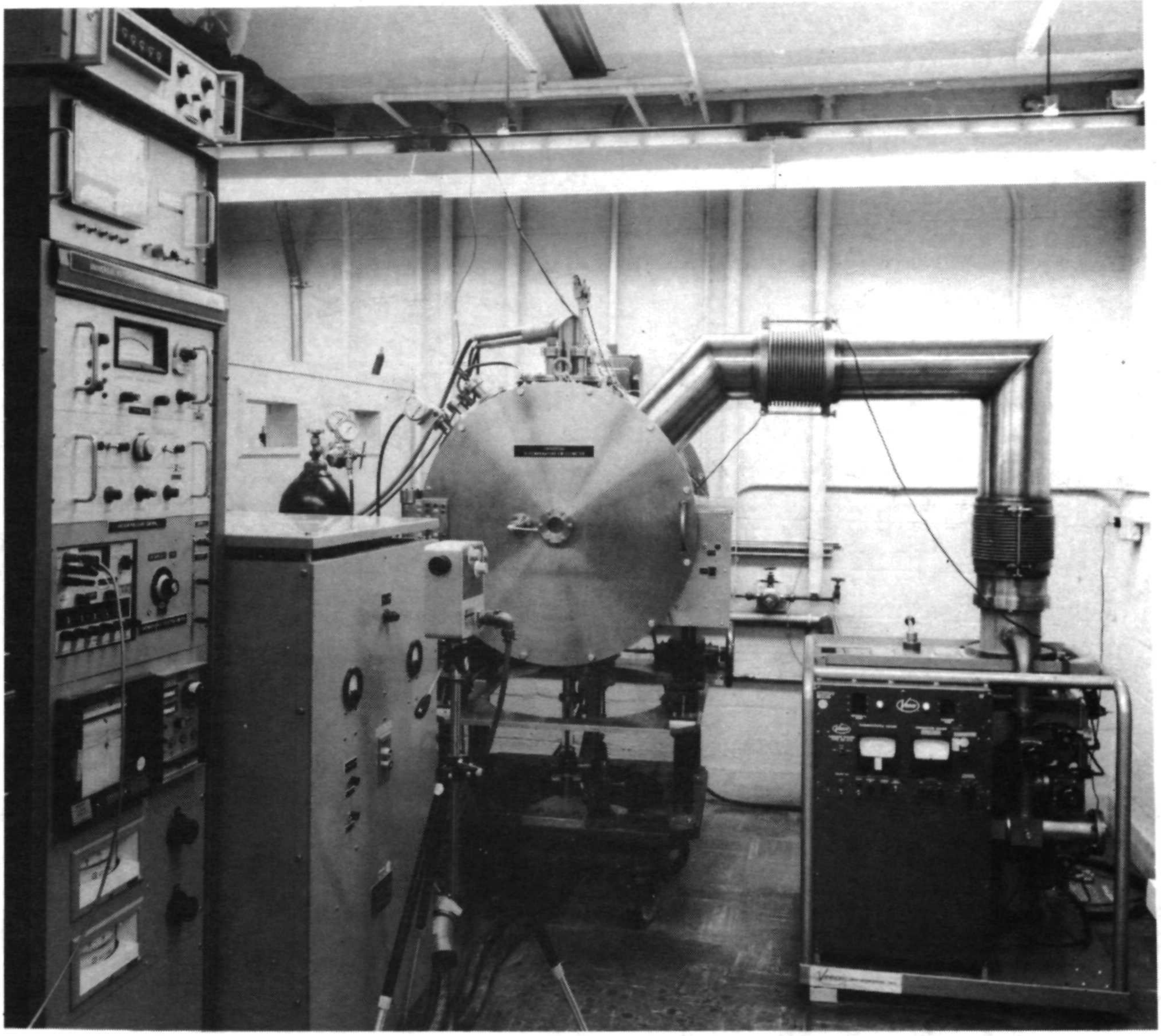

Fig. 42 Total Normal Emittance Apparatus

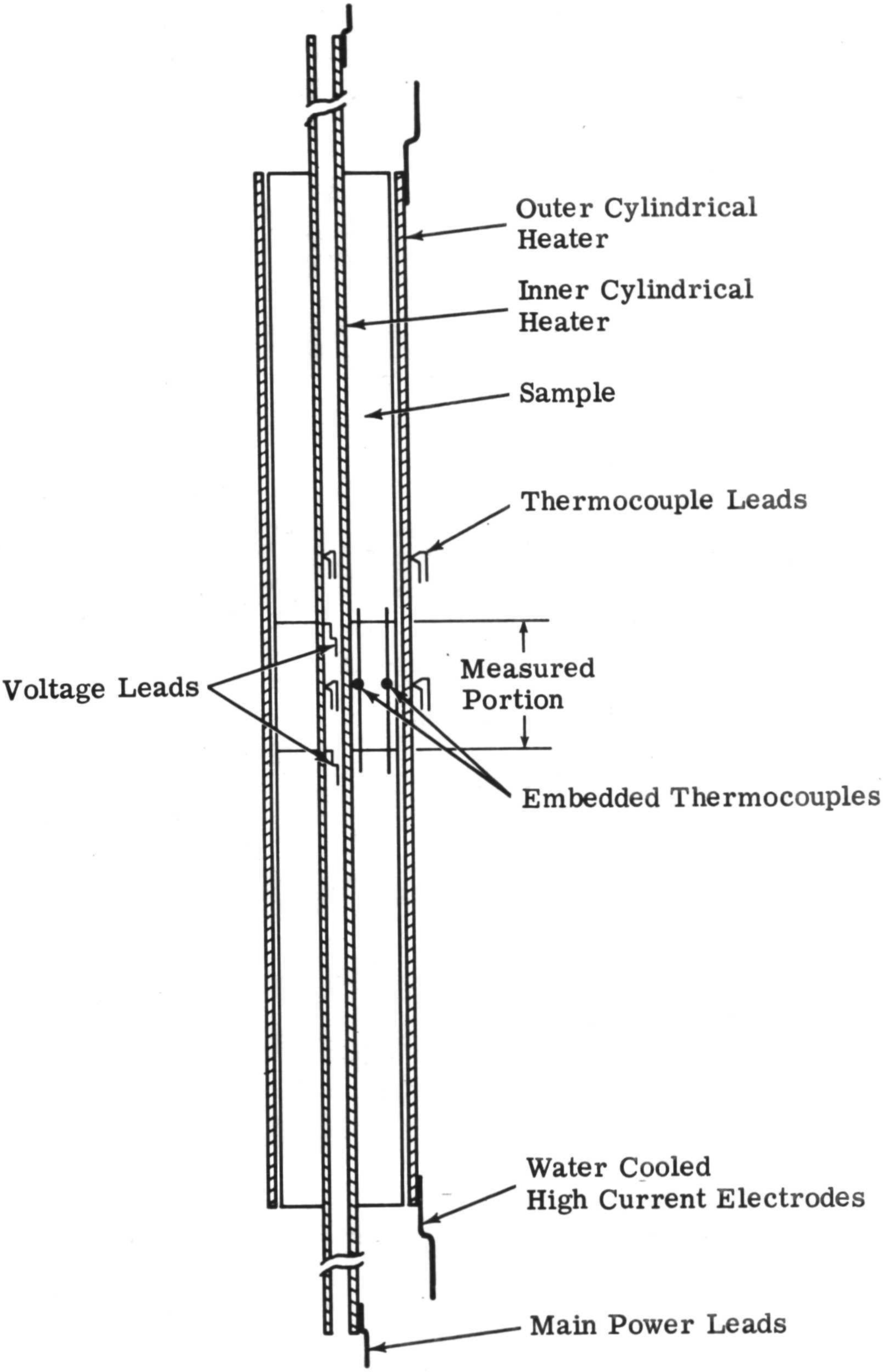

Fig. 43 Thermal Conductivity Apparatus

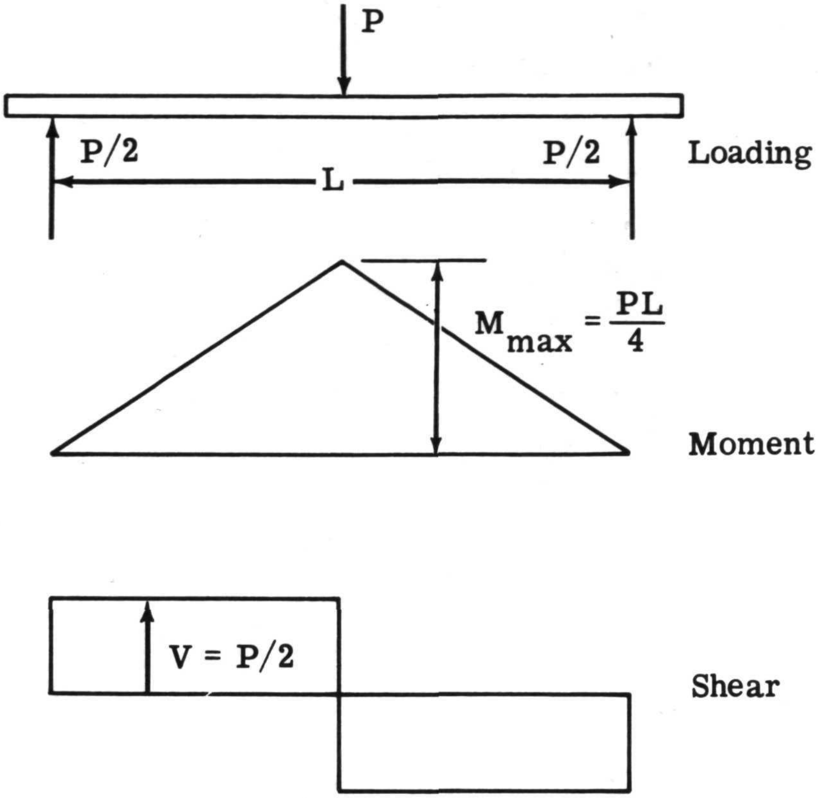

a) Loading, Moment, and Shear Diagram

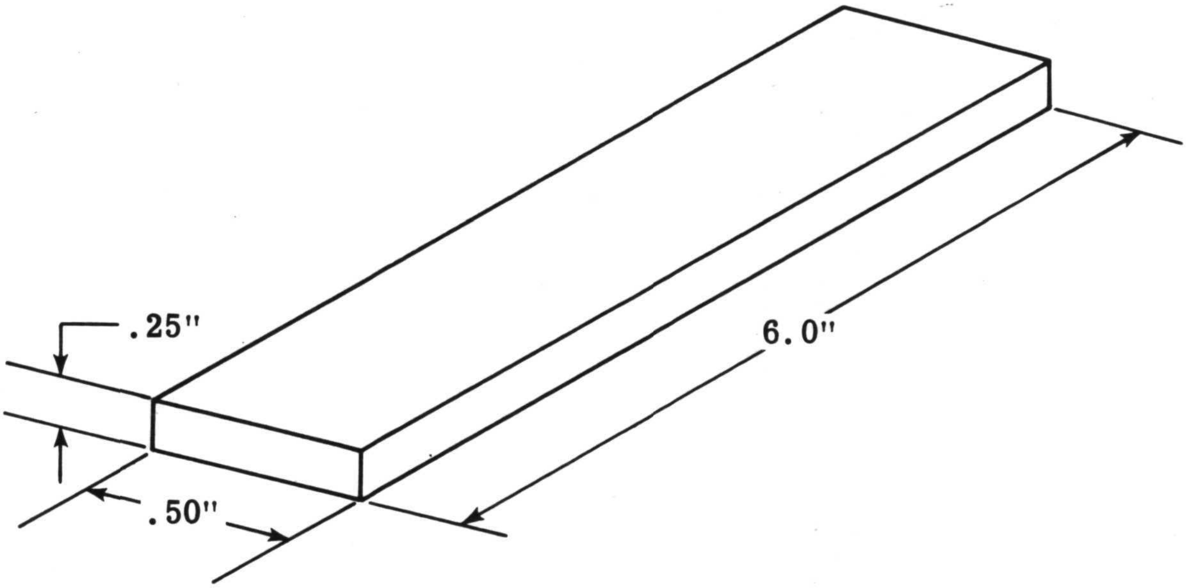

b) Flexure Specimen

Fig. 44 Single Center Point Loading Arrangement

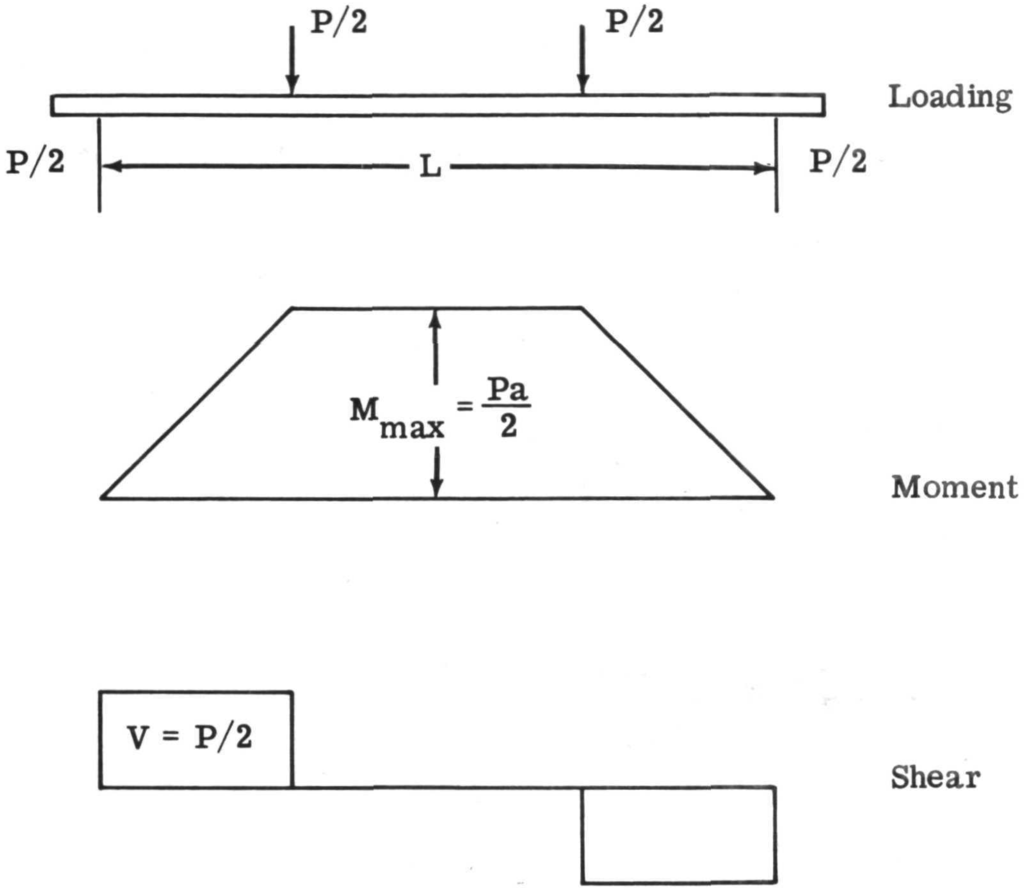

a) Loading, Moment, and Shear Diagram

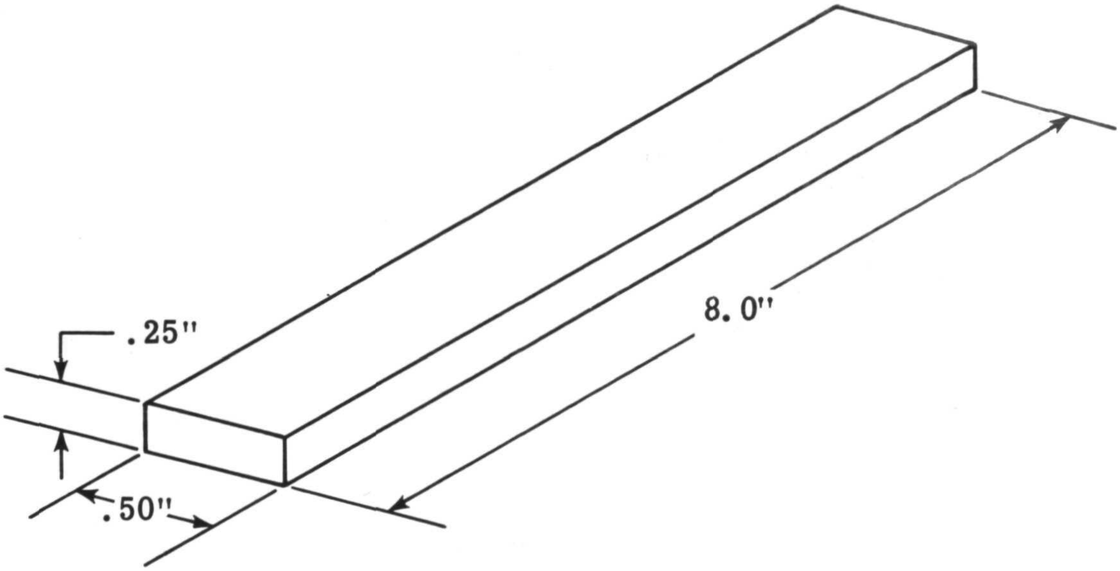

b) Flexure Specimen

Fig. 45 Four Point Loading Arrangement

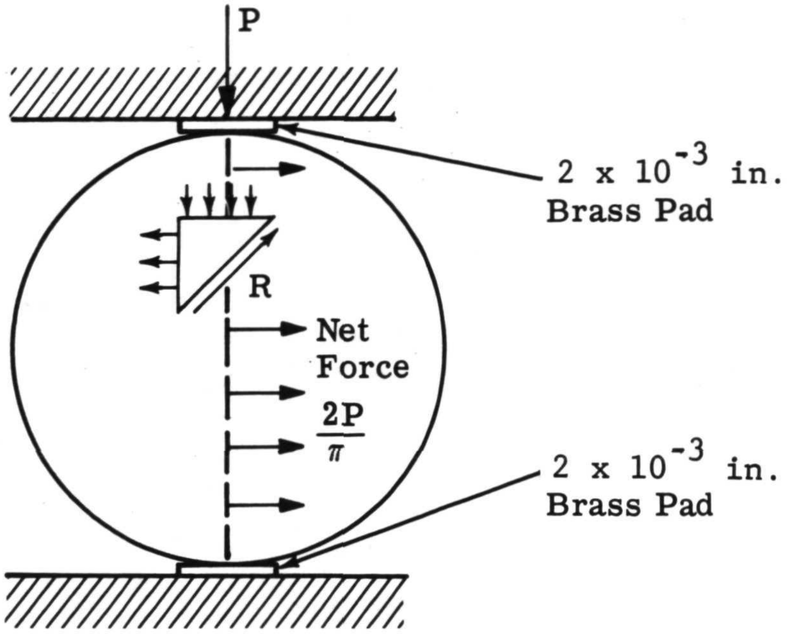

a) Stress Distribution

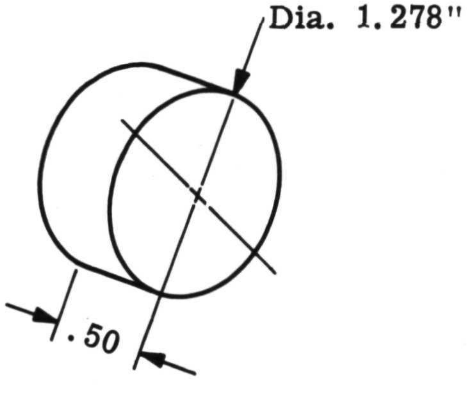

b) Dimensions

Fig. 46 Diametral Compression Specimen

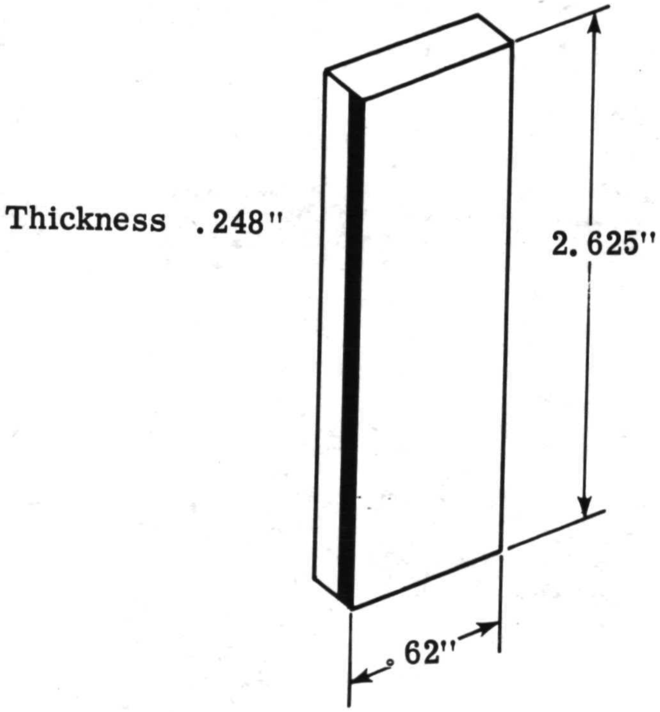

Fig. 47 Dimensions of Edgewise Compression Specimen

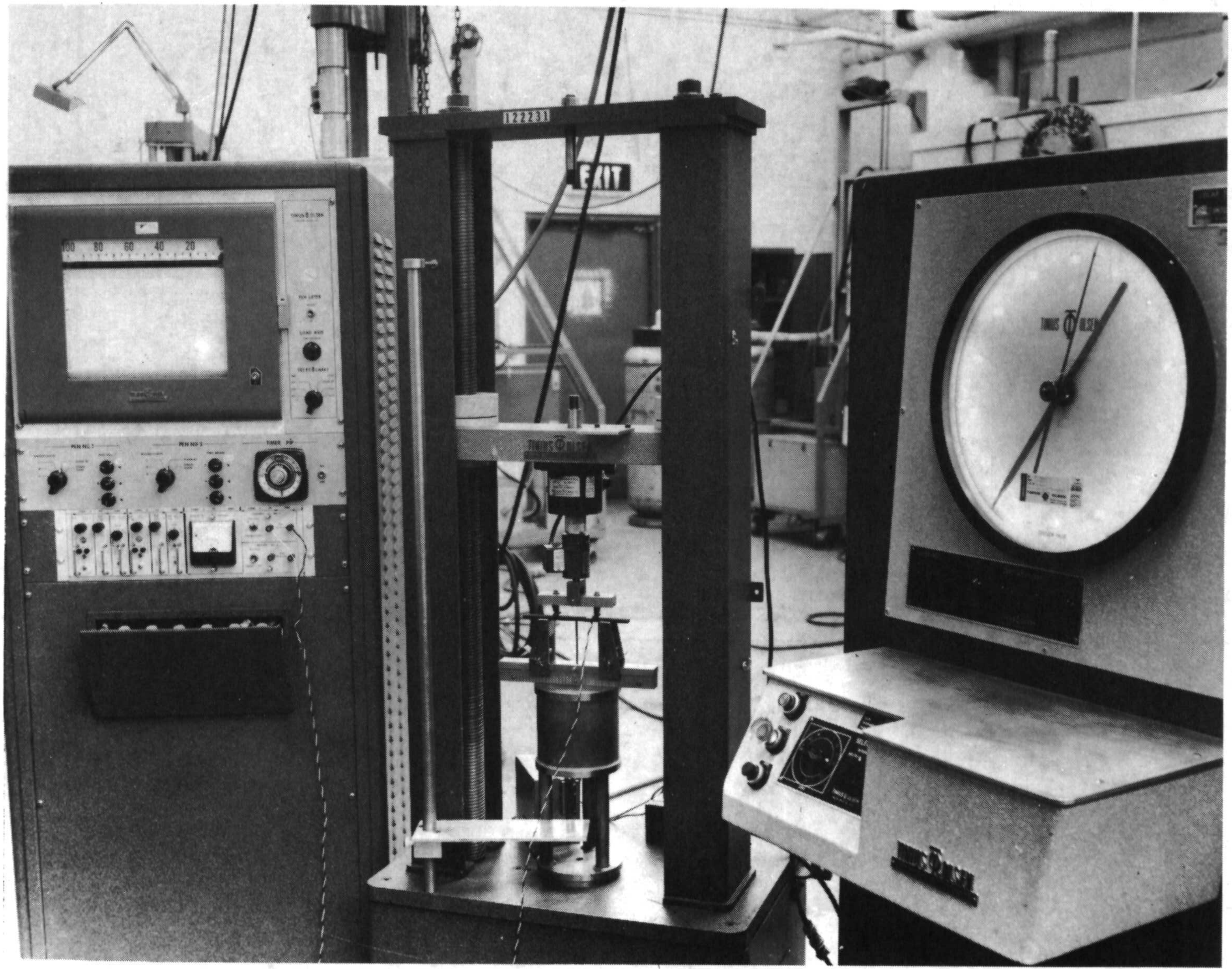

Fig. 48 Over-all View of Tinius Olsen Lo-Cap Universal Testing Machine with Quarter Point Flexural Loading Fixturization Installed. Strain gauge data (note wire on specimen) are recorded by the x-y-y' autograph recorder at left.

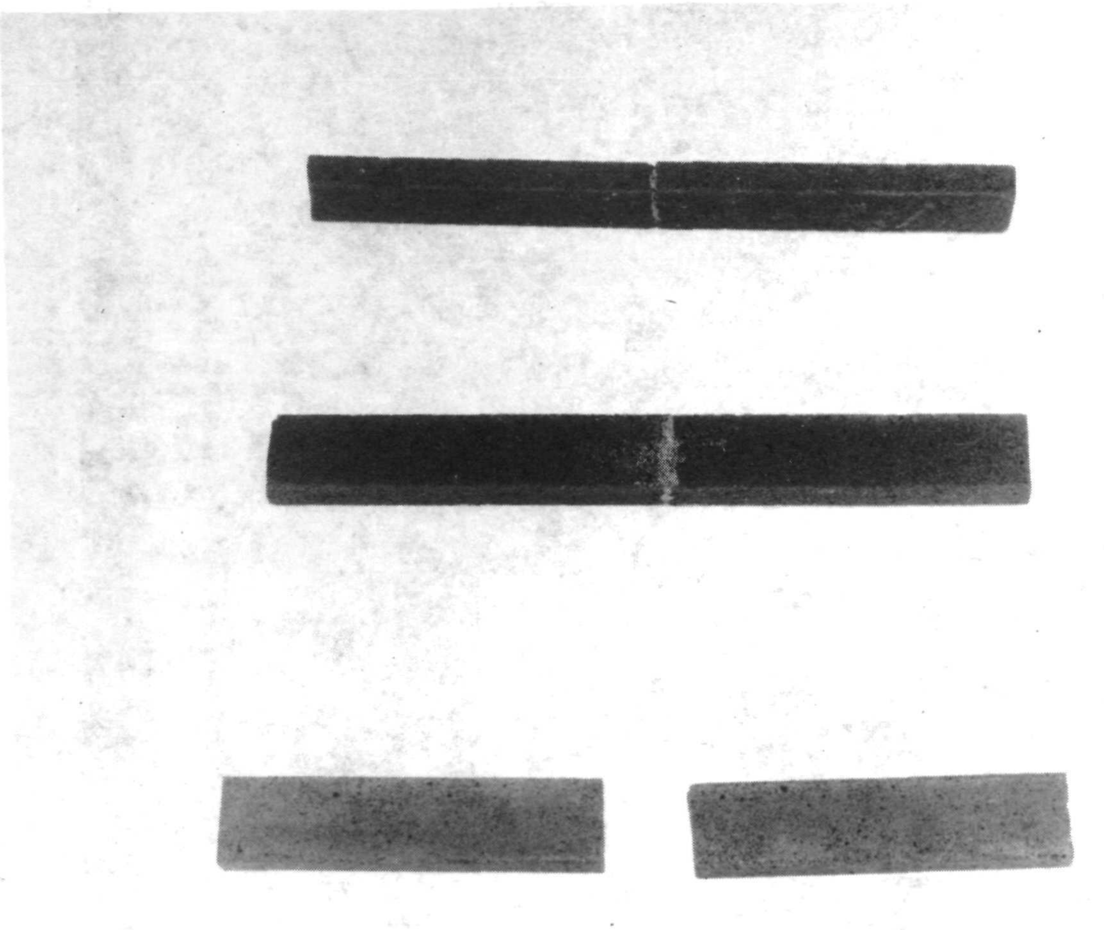

Fig. 49 Beam Specimens Used in Single Center Point Flexure Tests. Failure occurs at midspan, under loading point.

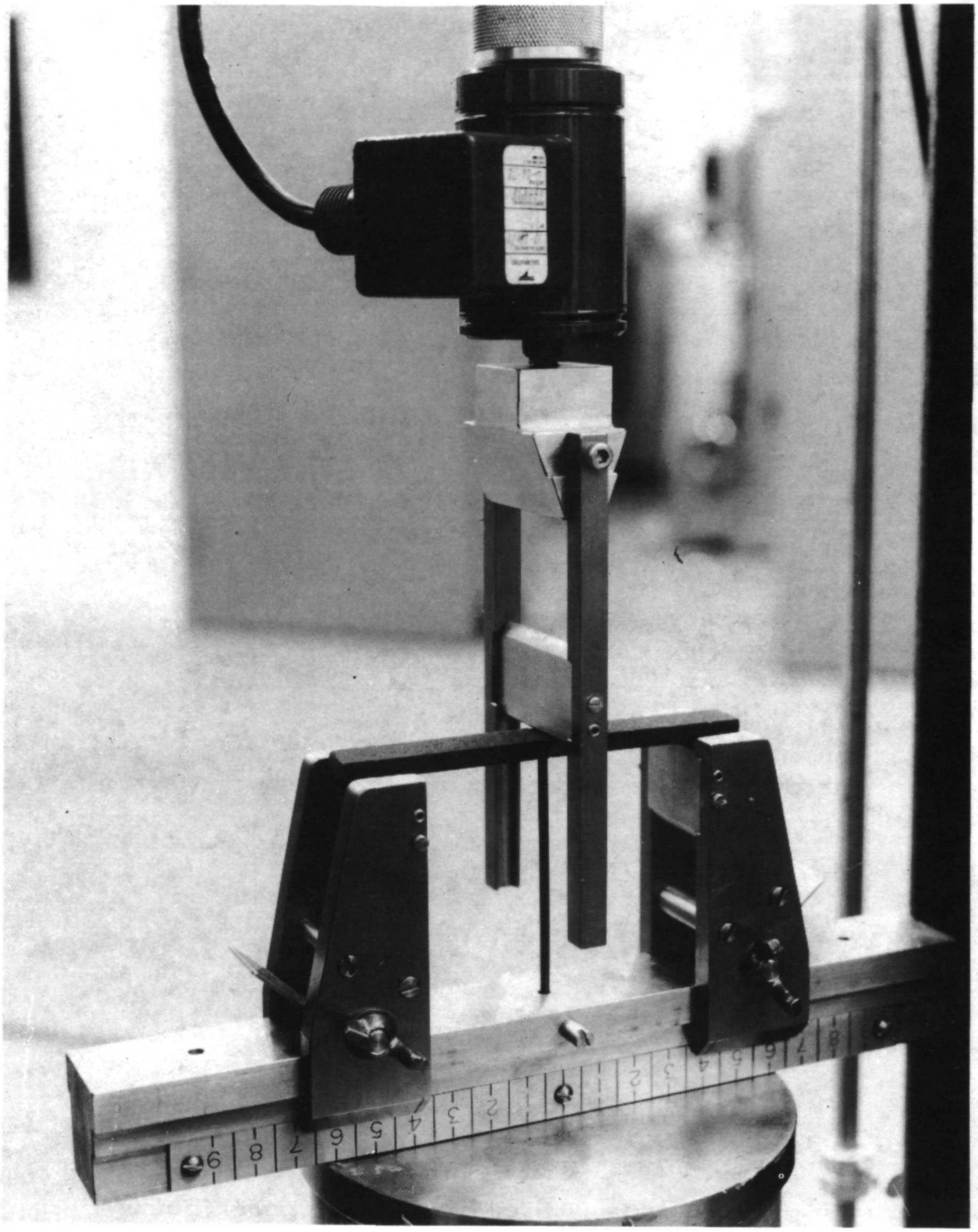

Fig. 50 Fixturization of the Single Center Point Flexure Test. Vertical bar at midspan is deflection transmission rod.

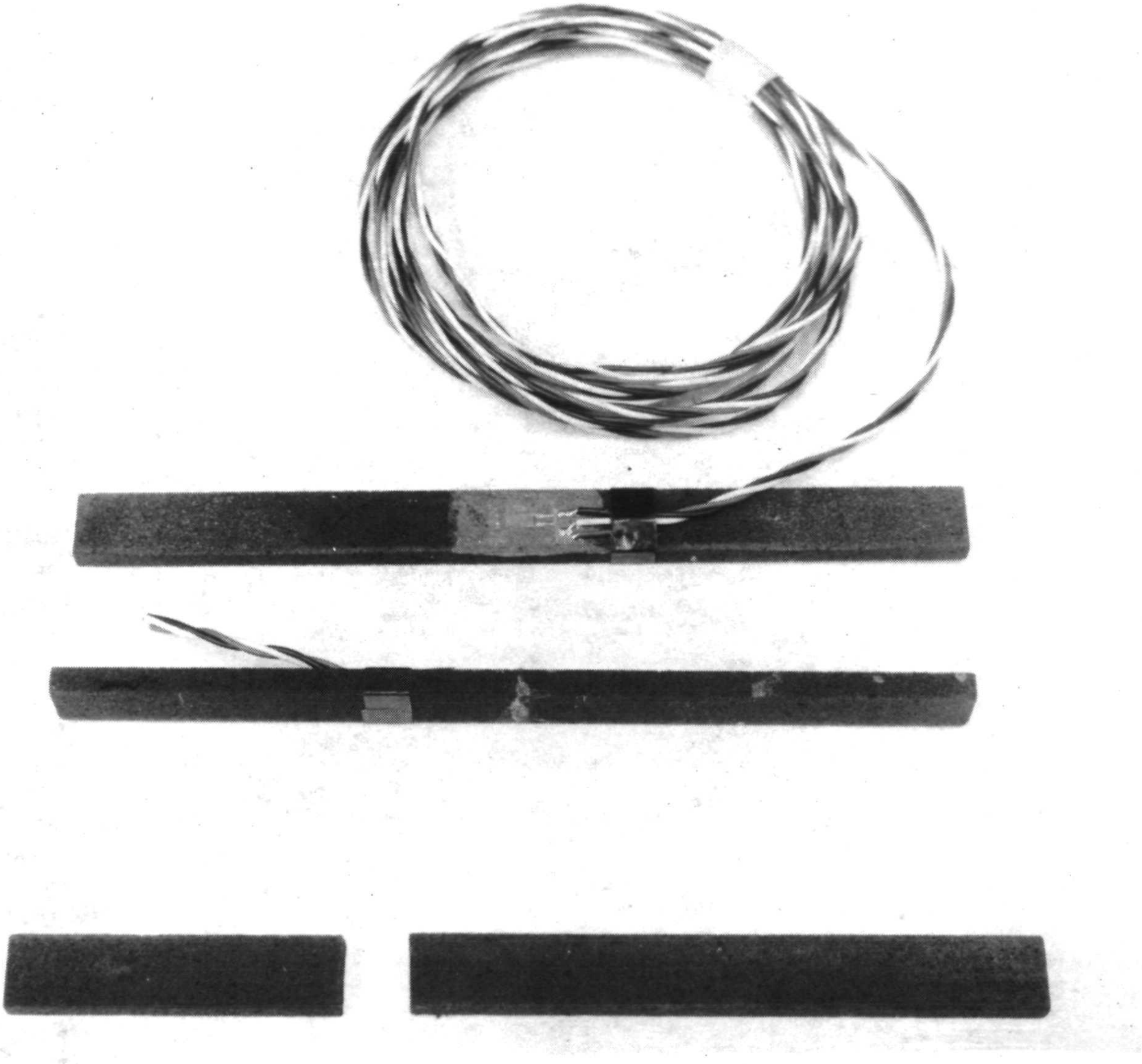

Fig. 51 Flexure Specimens, Quarter Point Loading. Note strain gauge installed at tension face of specimen.

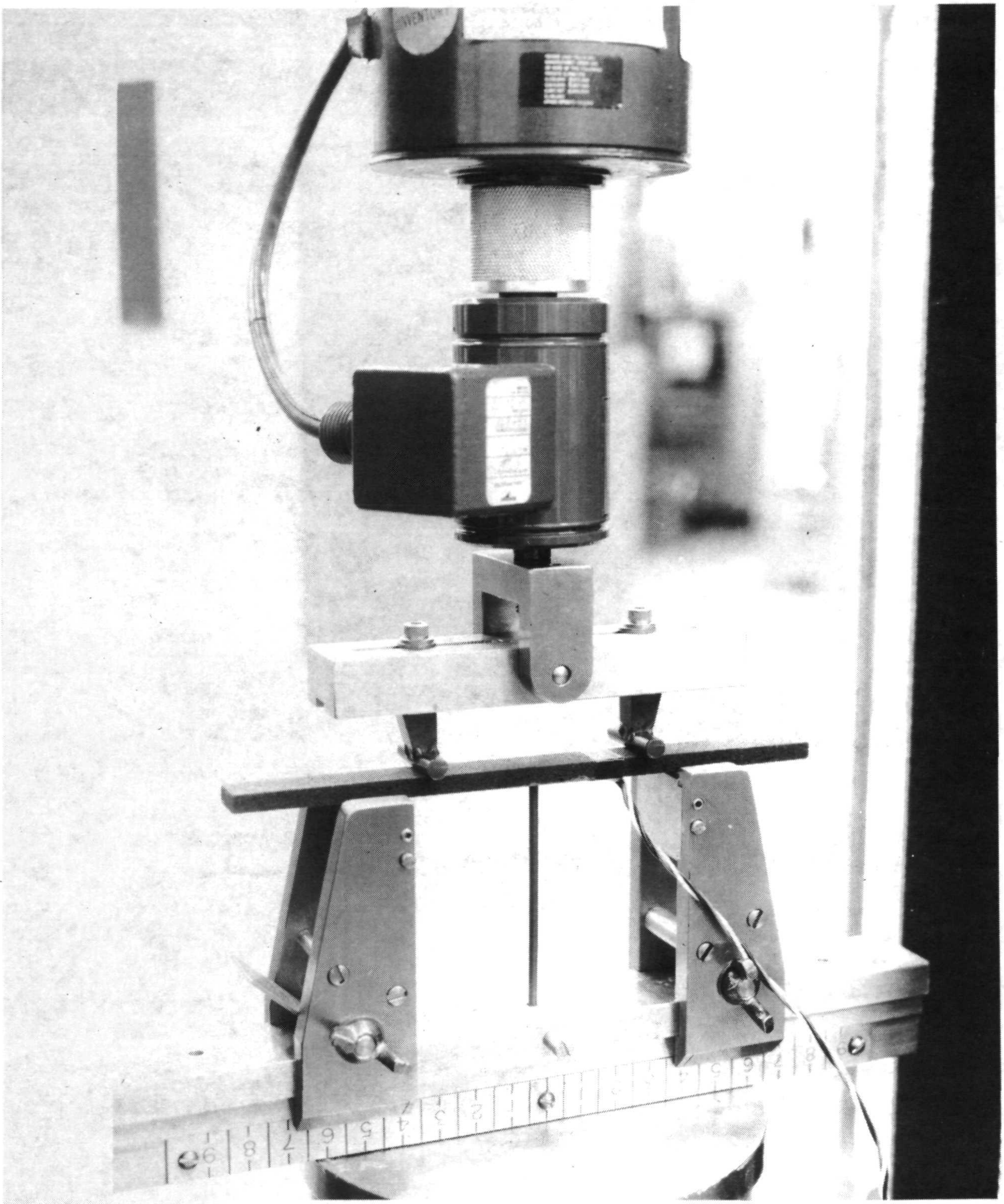

Fig. 52 Quarter Point Flexure Fixtures. Deflection is recorded at specimen midspan by deflectometer transmission rod (vertical bar).

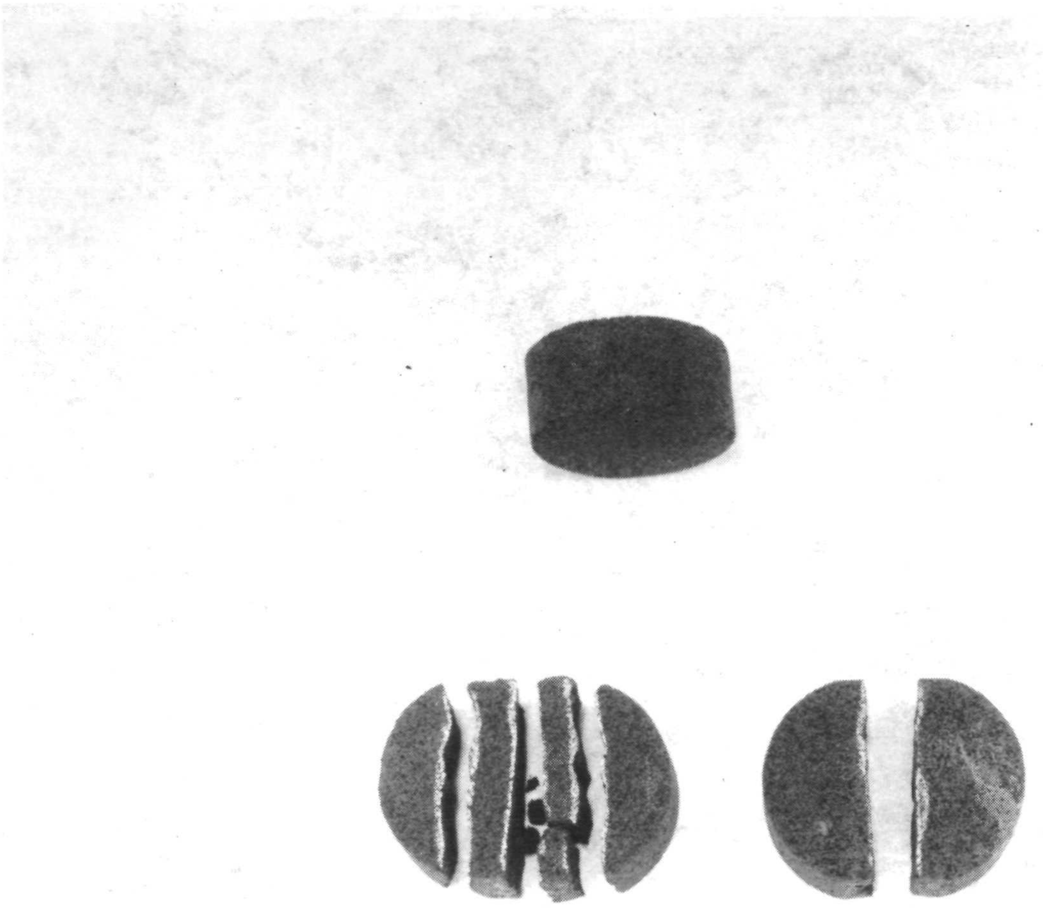

Fig. 53 Tensile (Diametral Compression) Specimen Before and After Testing. Note the two modes of failure - multiple fracture (with characteristic triple clef) and single tensile plane failure.

Fig. 54 Close-up of Diametral Compression Fixture. Brass pads atop and under specimen ease transition of loading from machine platens to specimen.

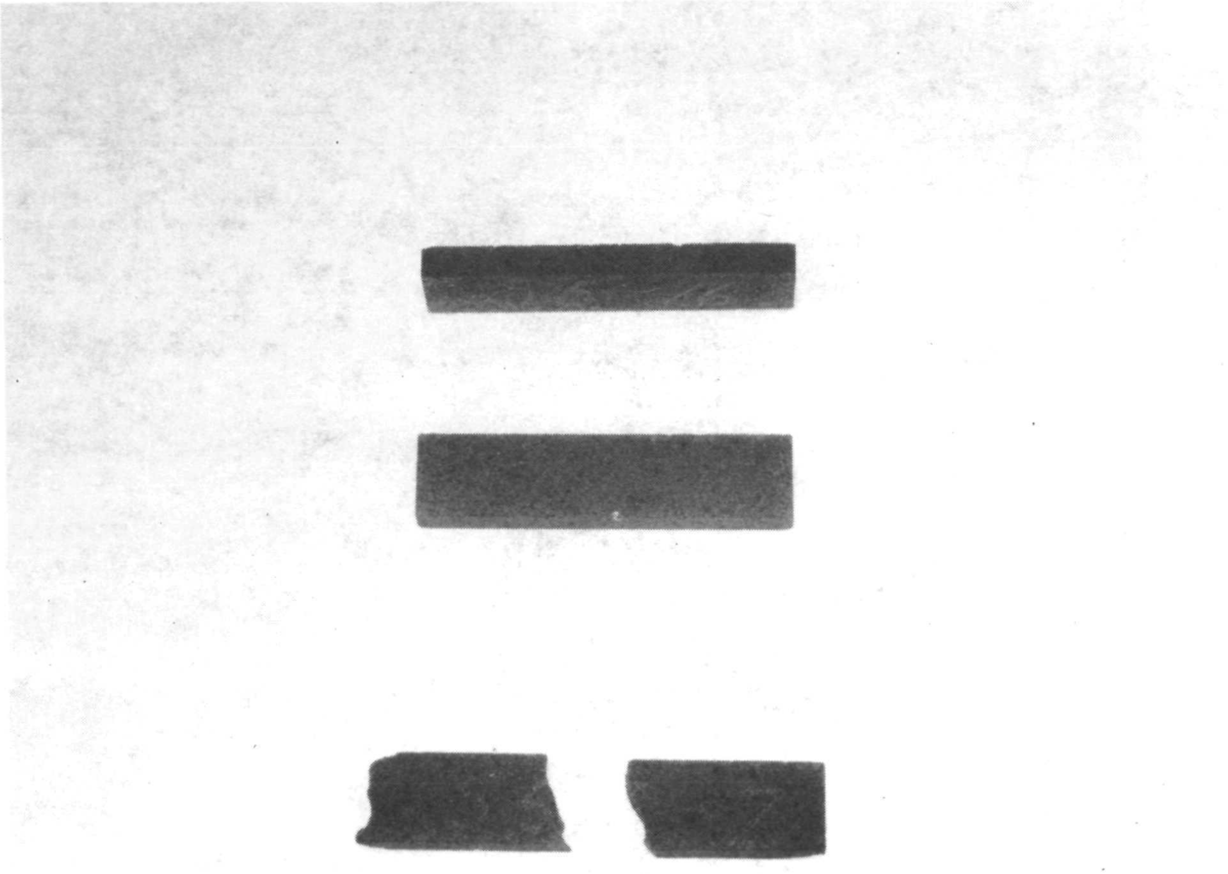

Fig. 55 Edgewise Compression Specimen Before and After Test

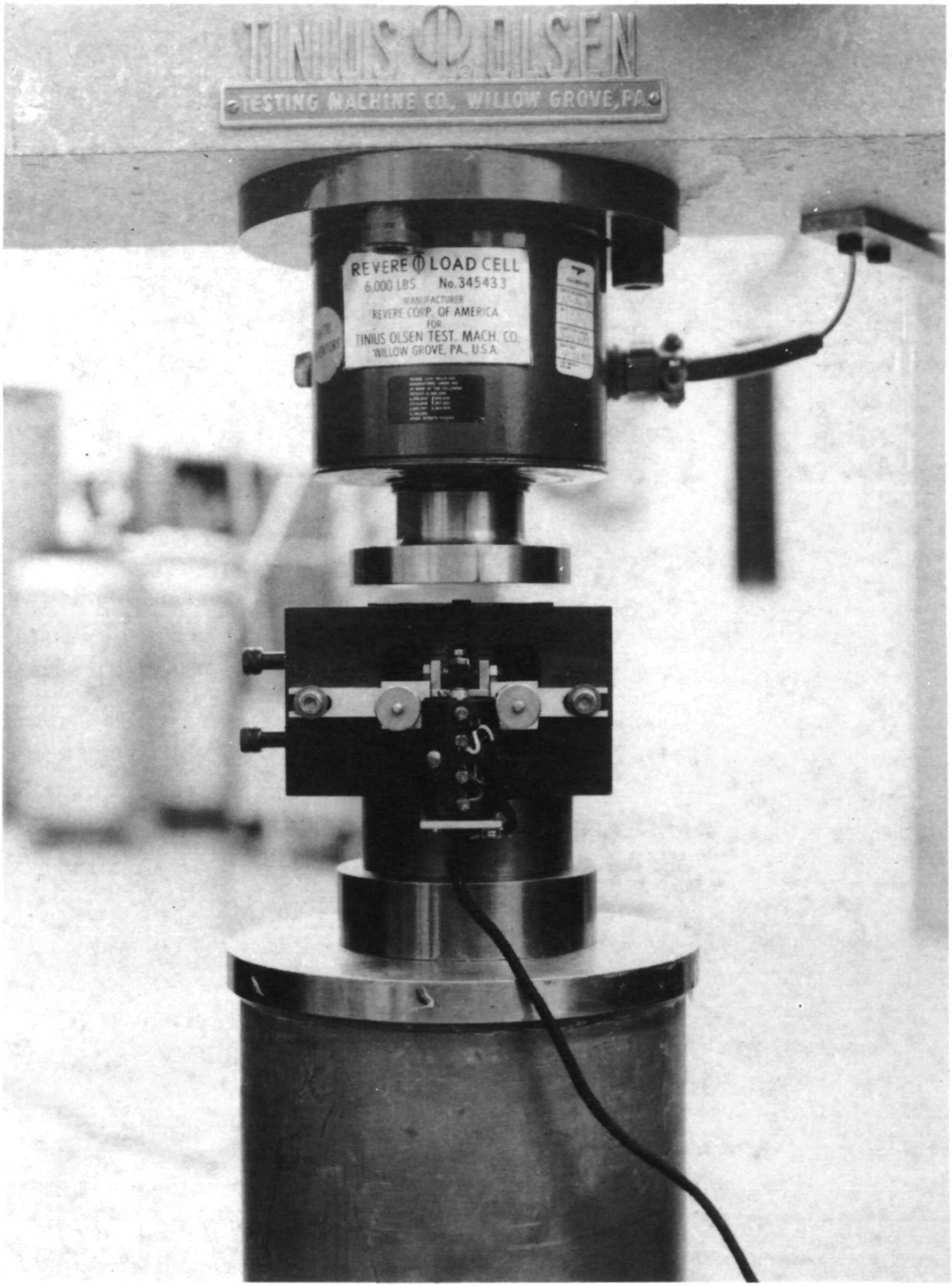

Fig. 56 View of Test Set-up Showing Montgomery-Templin Sheet Compression Fixture that Provides Lateral Specimen Restraint

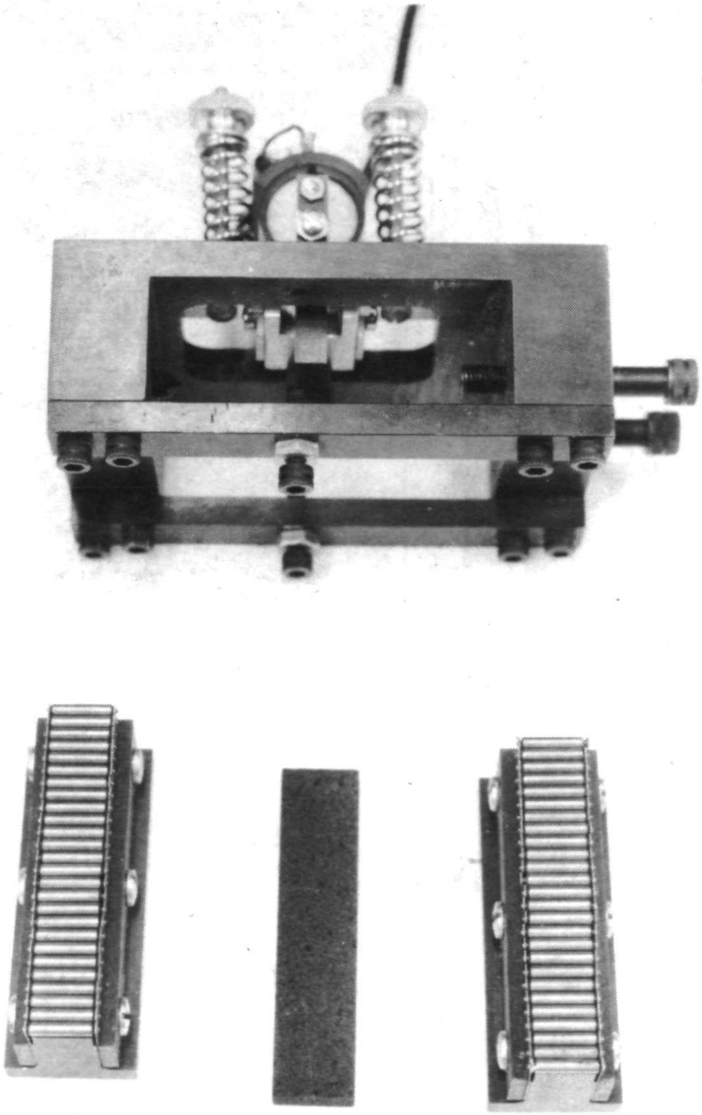

Fig. 57 Detailed View of Montgomery-Templin Fixture. Observe pin roller bearing for minimizing sliding friction and compressometer mount.

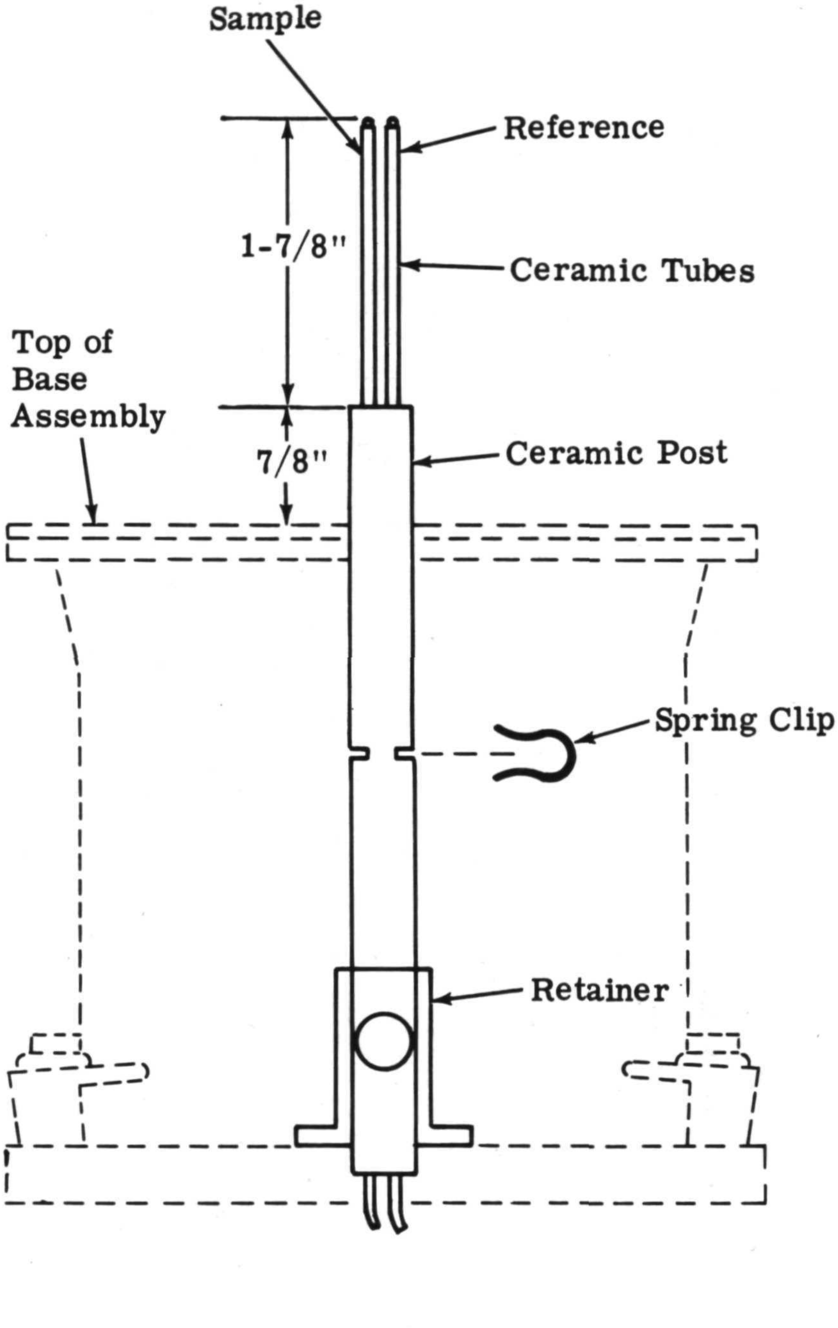

Fig. 58a The Differential Thermal Analysis Apparatus

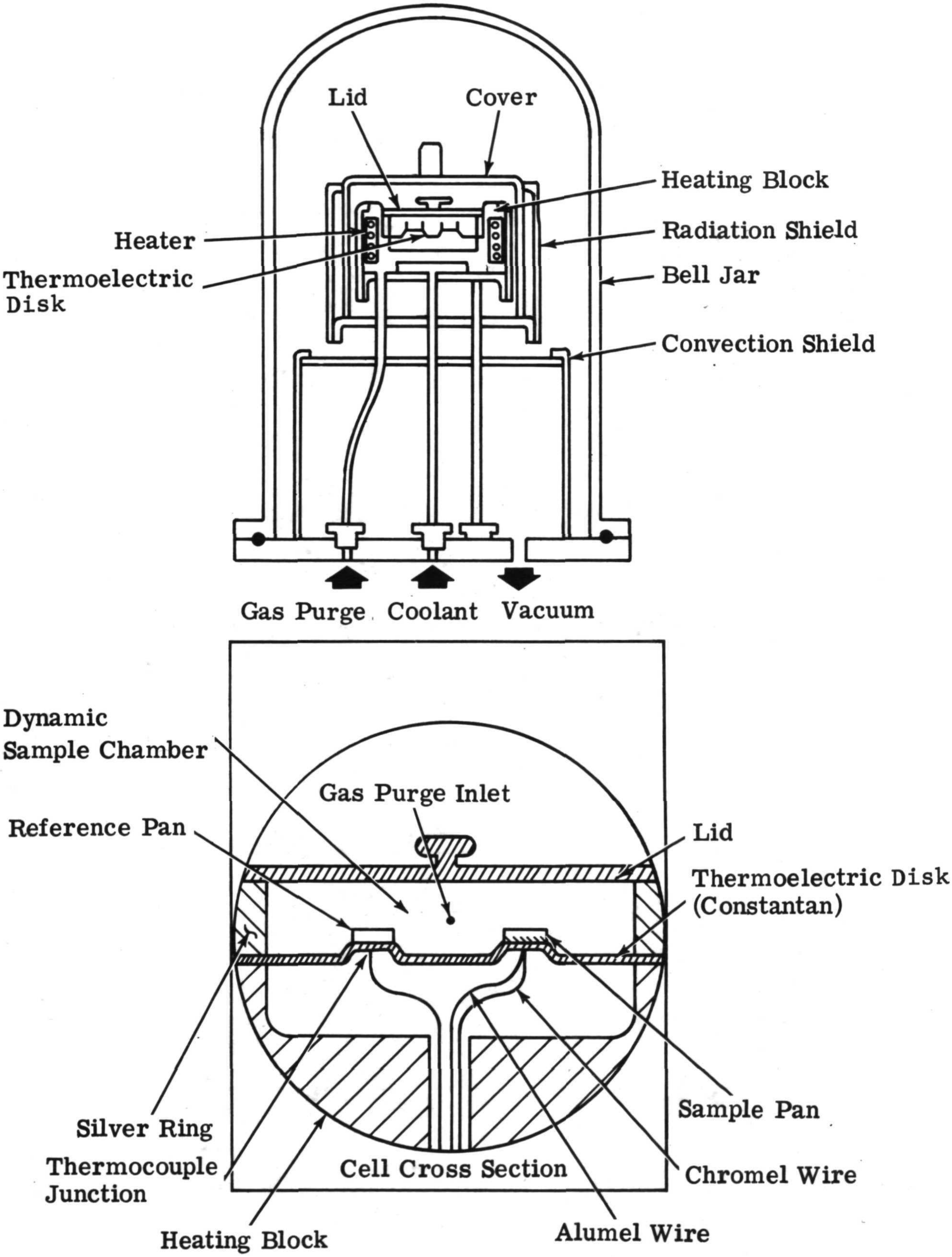

Fig. 58b The Differential Scanning Calorimeter Apparatus

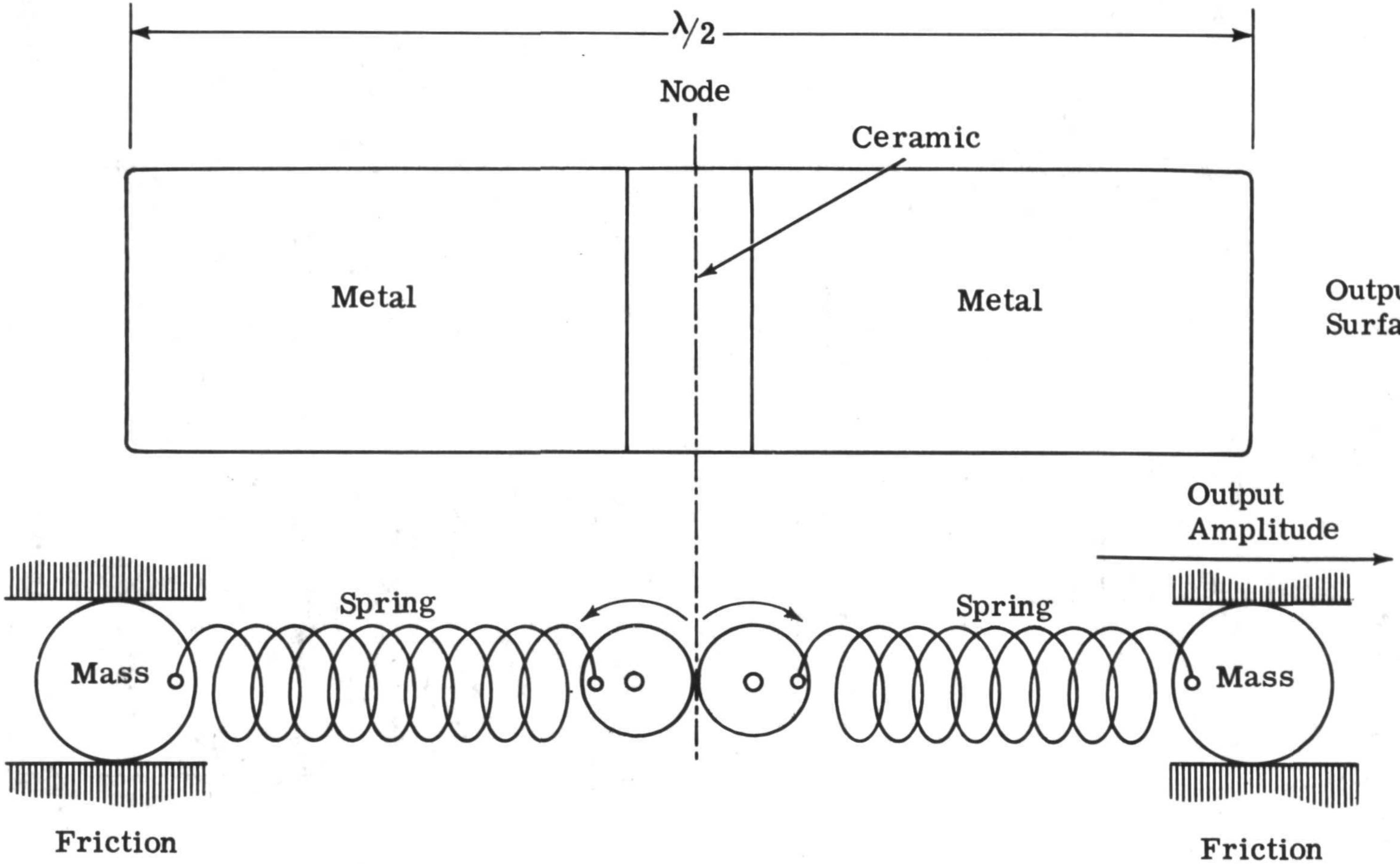

Fig. 59 The Symmetrical Piezoelectric "Sandwich" Type Transducer and Its Equivalent

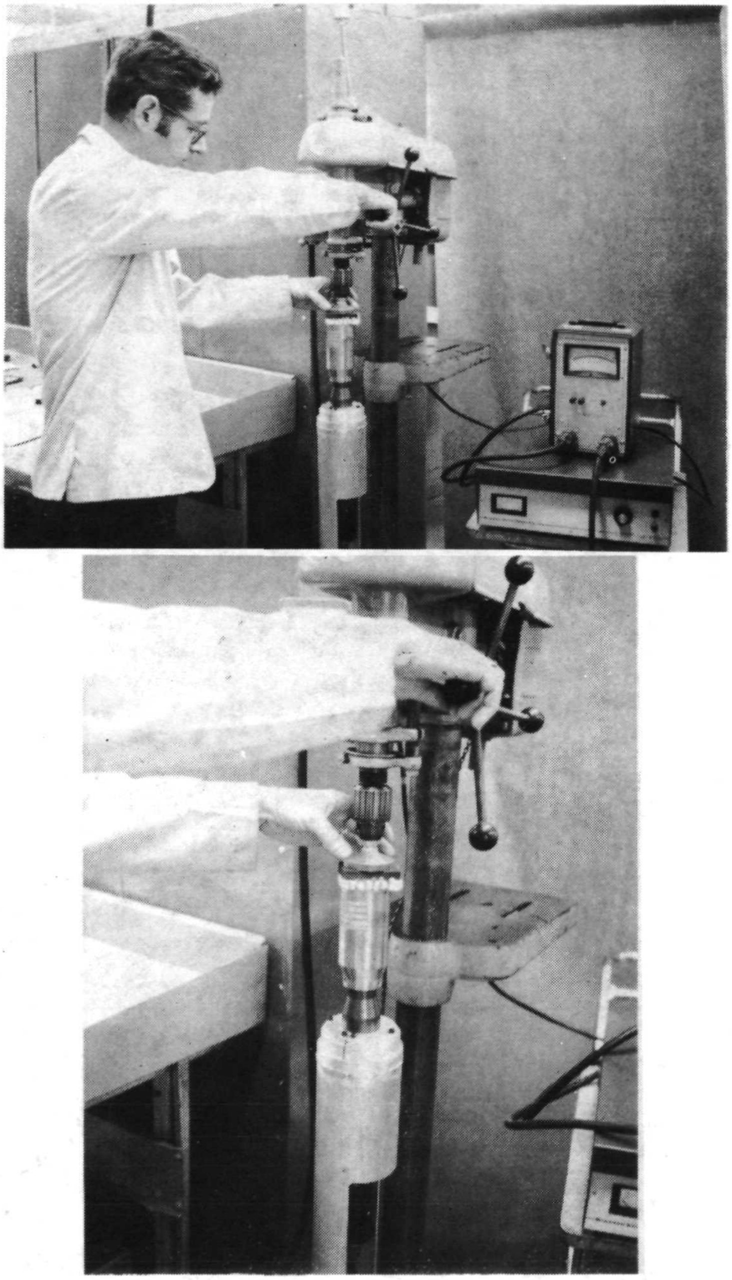

Fig. 60 Transducer-Horn Assembly for Producing CPI-Honeycomb Composites

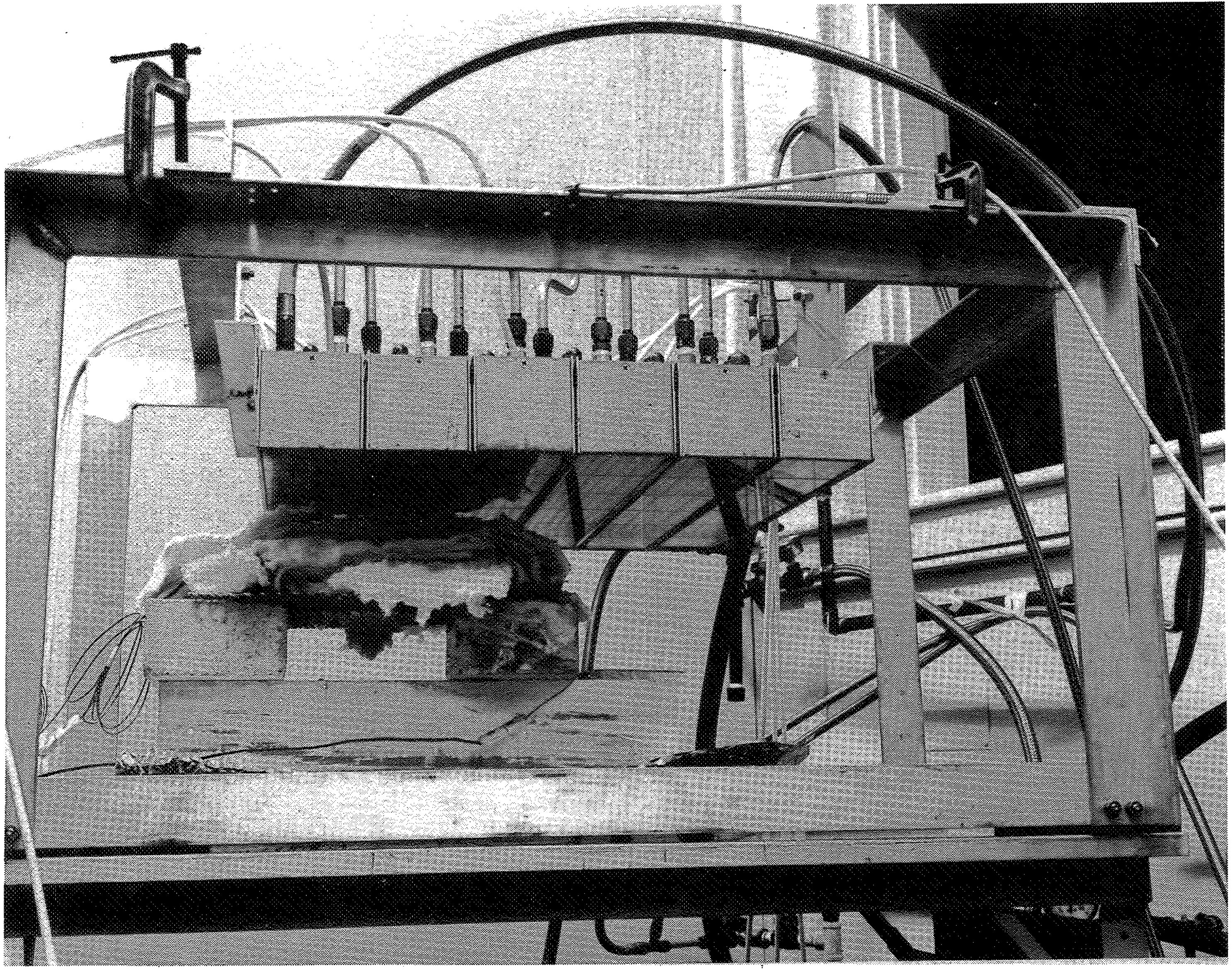

Fig. 61 Experimental Radiant Heat Lamp Facility (Underside View)

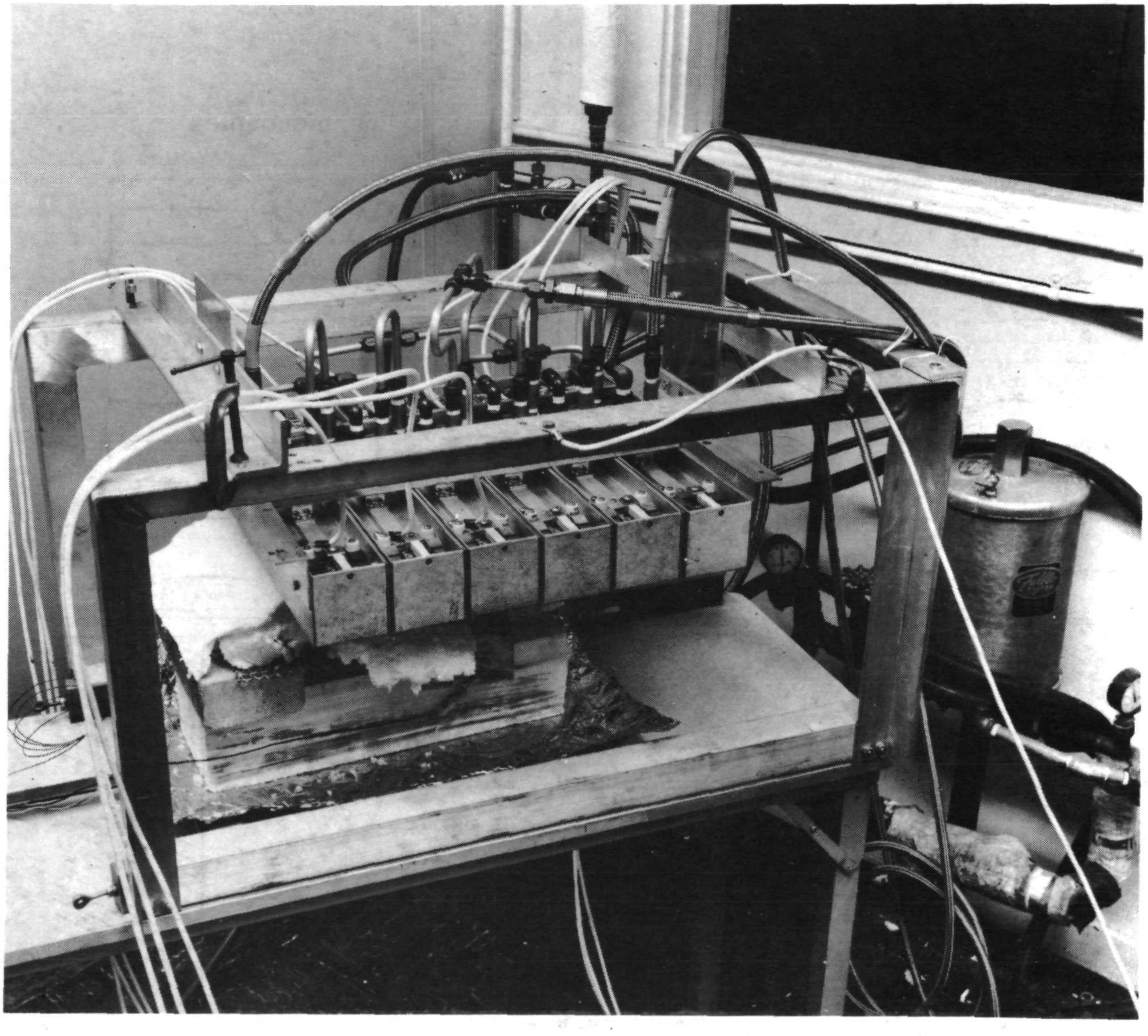

Fig. 62 Radiant Heat Lamp Facility (Top View)

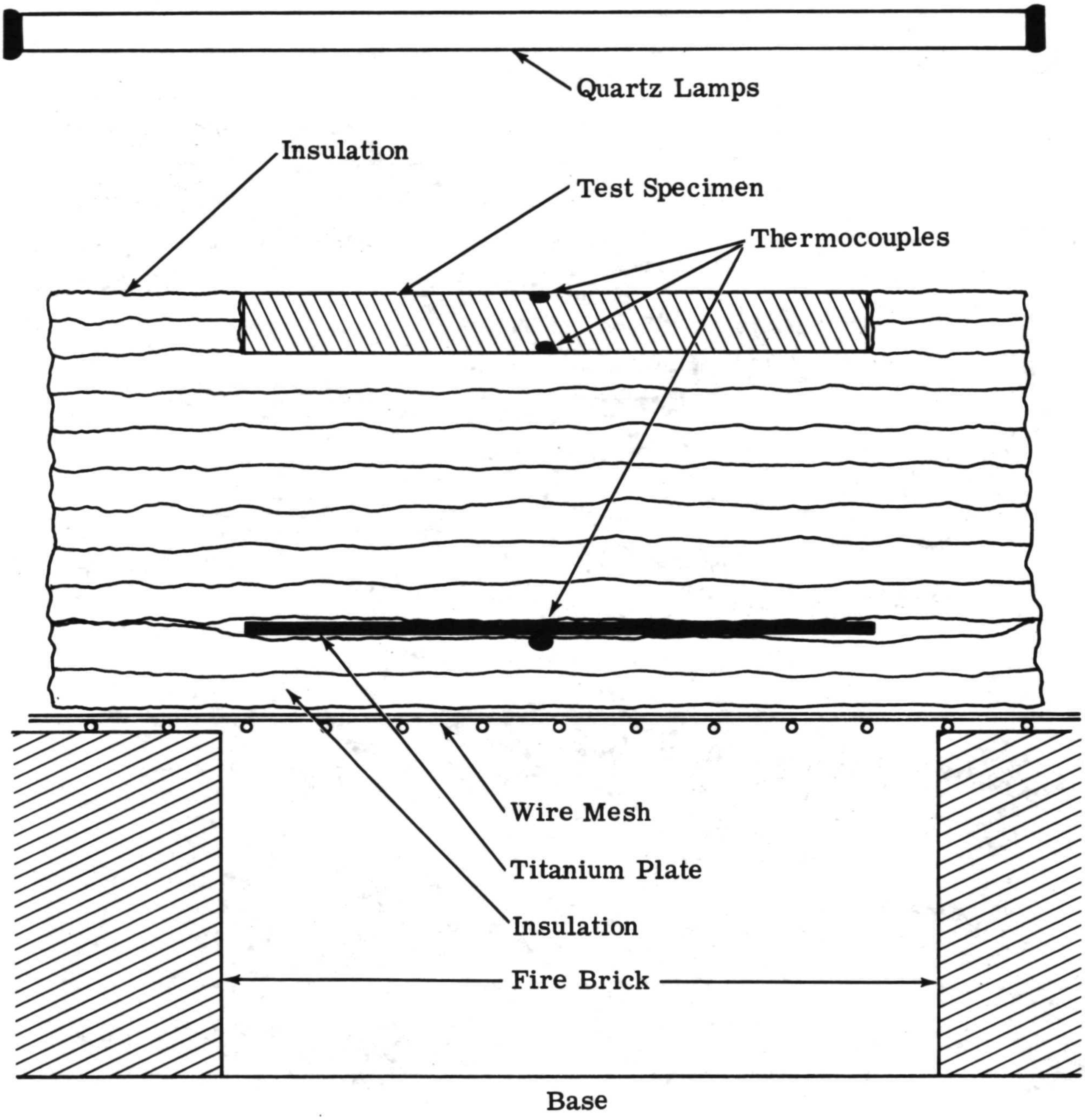

Fig. 63 Test Specimen Installation

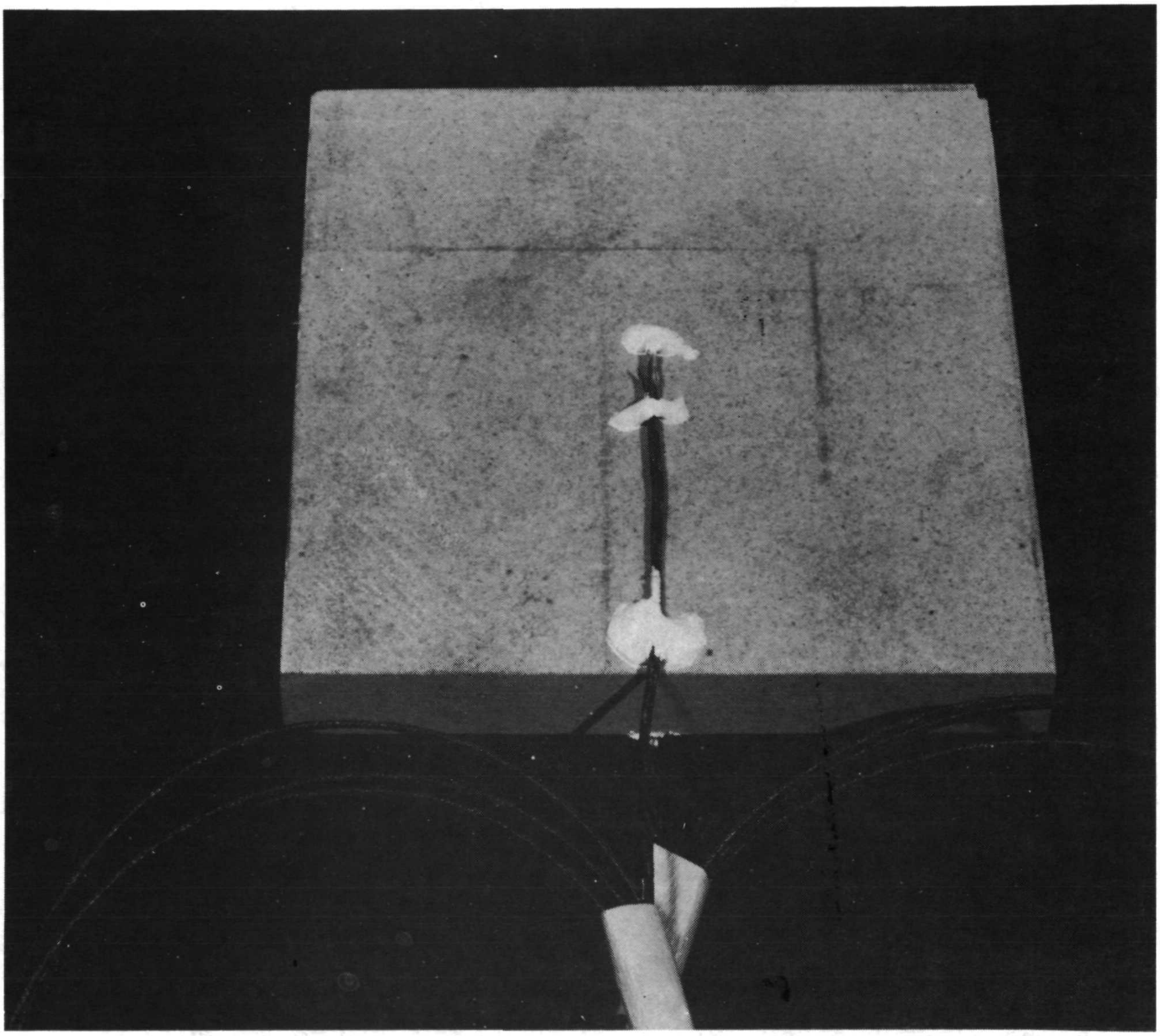

Fig. 64 Instrumented CPI Specimen (Square Cross Section)

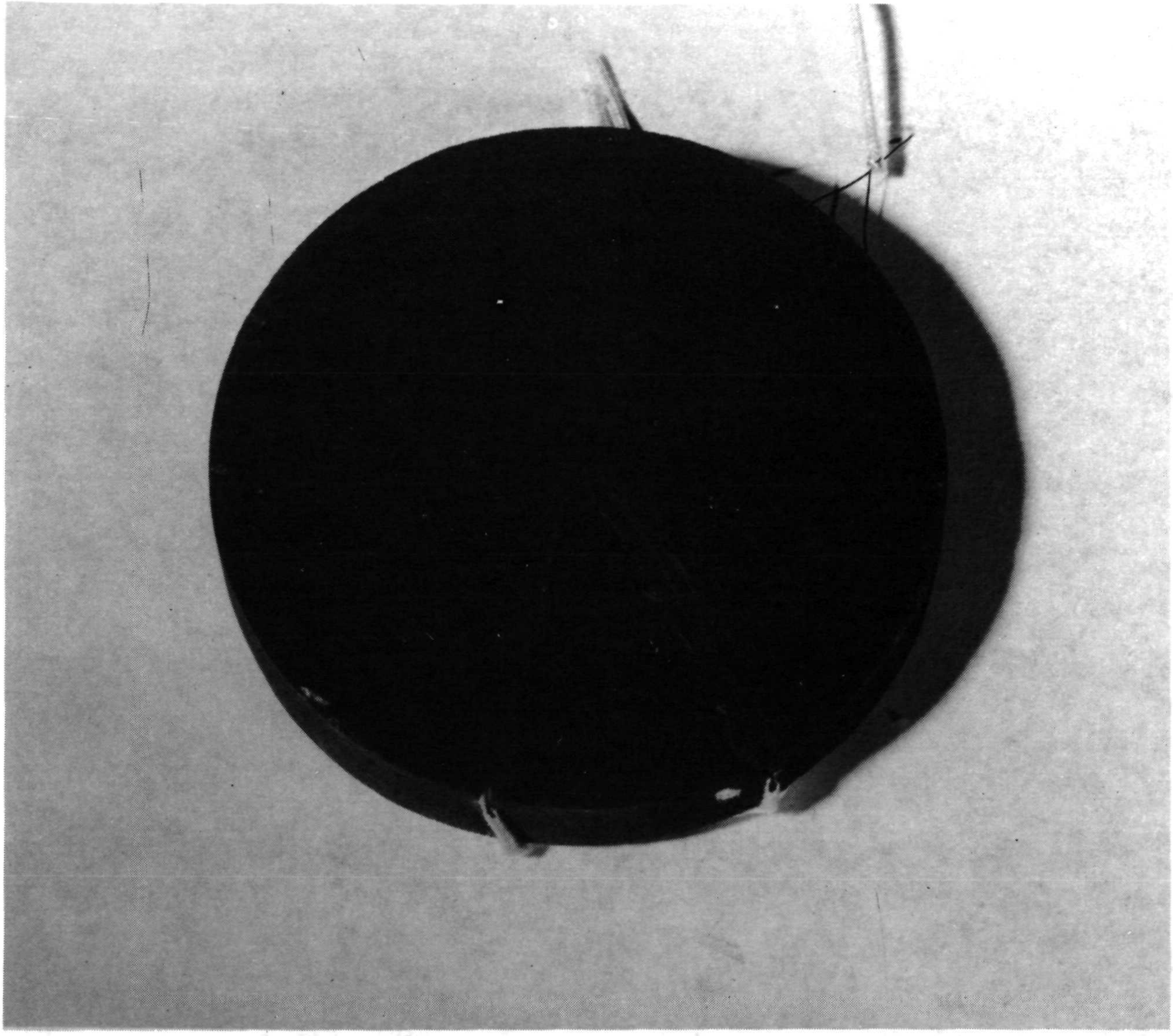

Fig. 65 Instrumented CPI Specimen (Circular Cross Section)

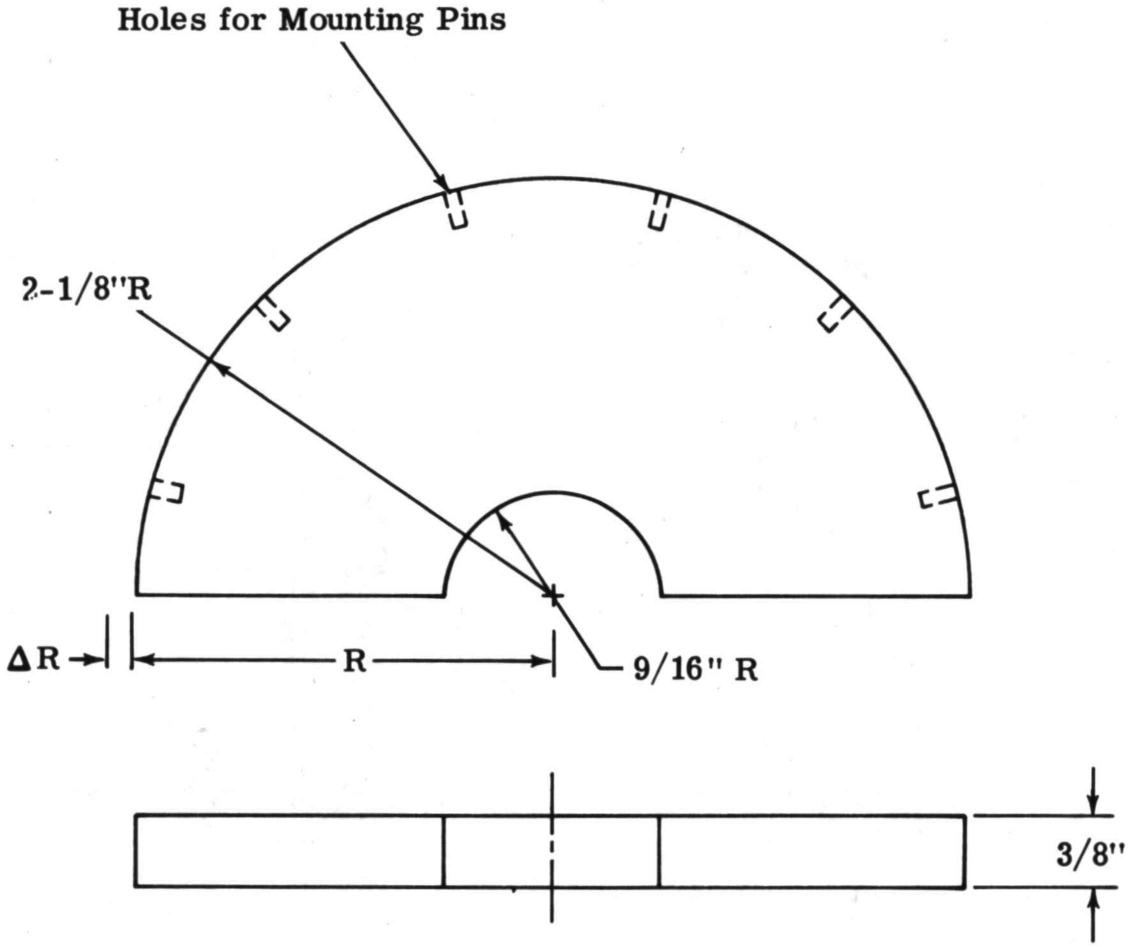

Fig. 66 Machined CPI Arc Jet Specimen

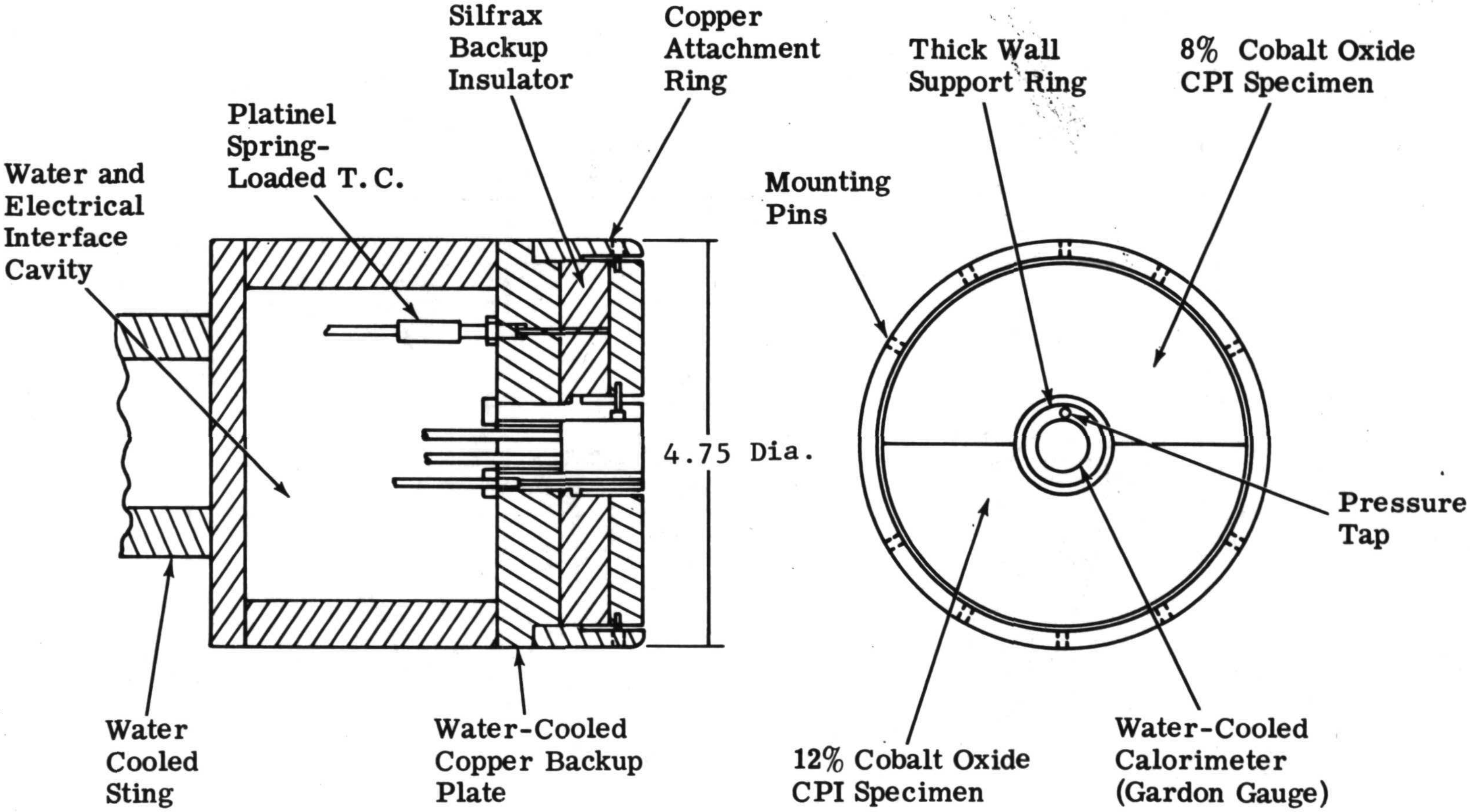

Fig. 67 Model Configuration for Arc Jet Test

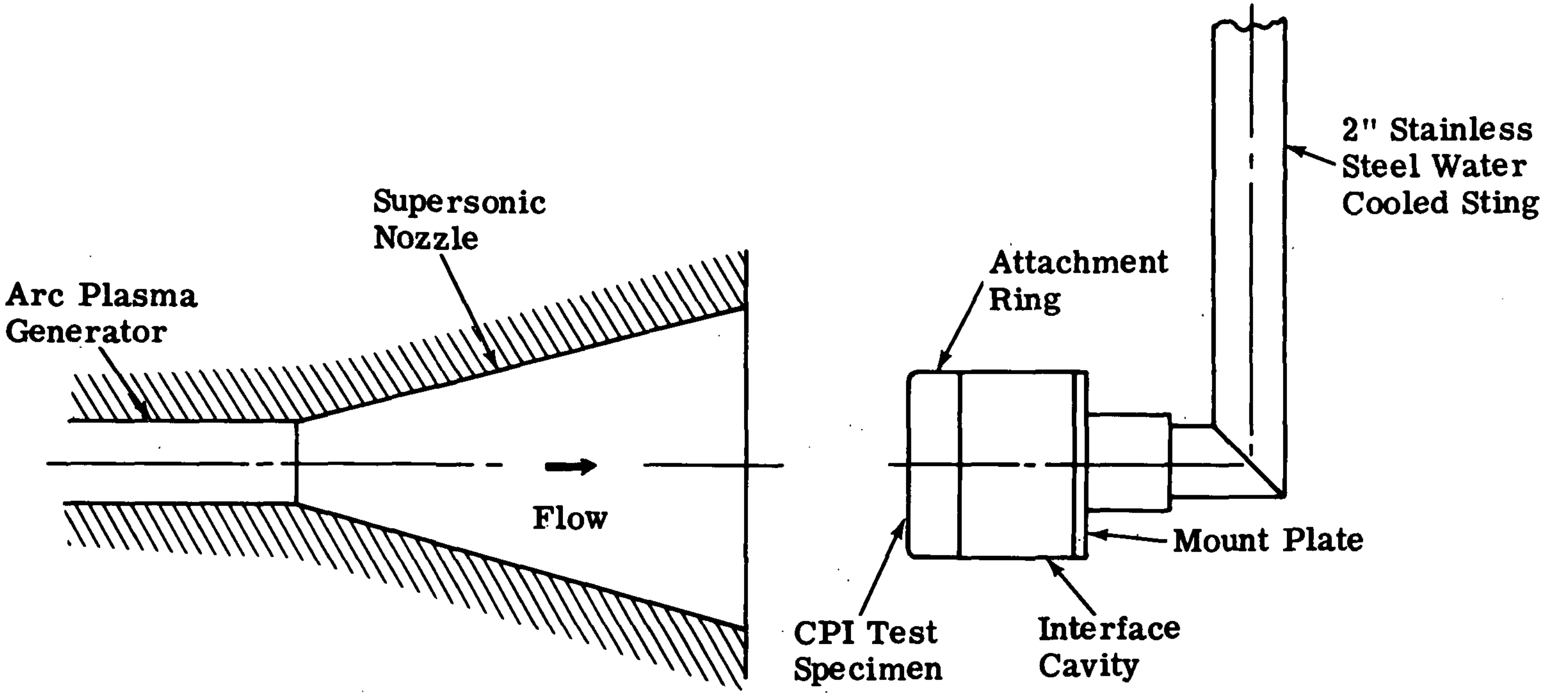

Fig. 68 Test Configuration for Arc Jet Test

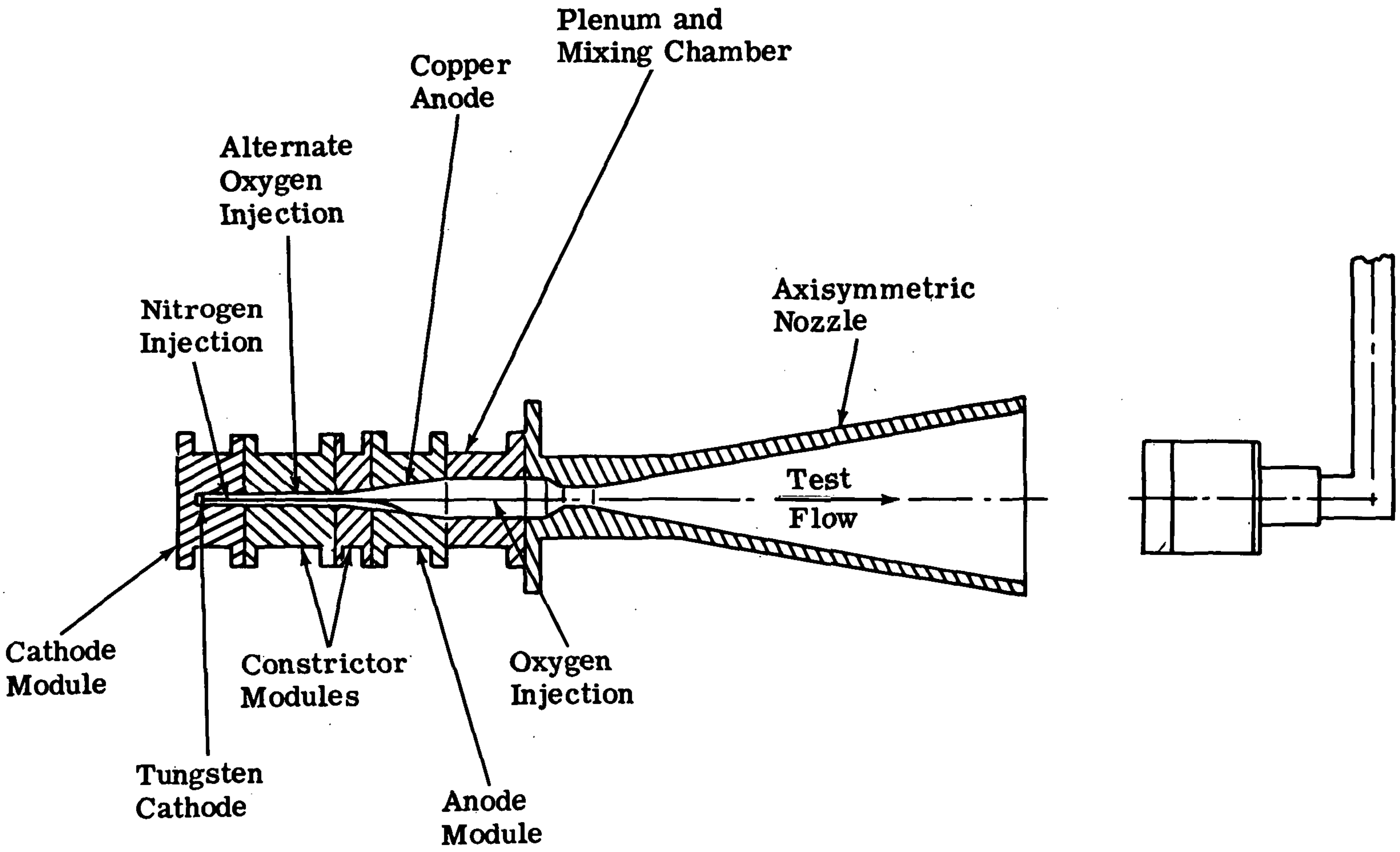

Fig. 69 Aerotherm 1 MW Constrictor Arc Jet Heater-Low Flow Rate Modification

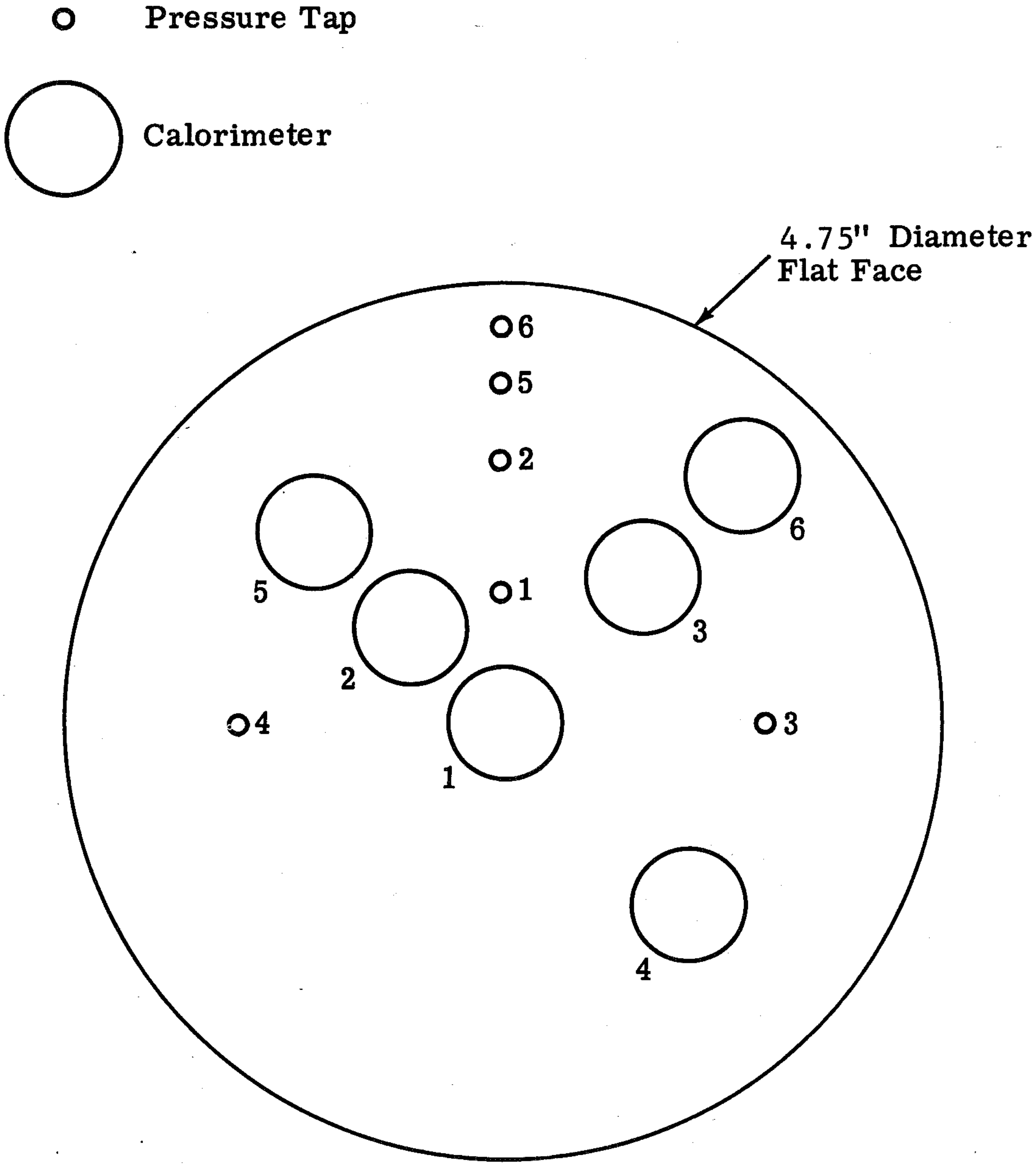

Fig. 70 Calibration Model for Arc Jet Test

☆U.S. GOVERNMENT PRINTING OFFICE: 1973-739-029/59

NATIONAL AERONAUTICS AND SPACE ADMINISTRATION
WASHINGTON, D.C. 20546

OFFICIAL BUSINESS
PENALTY FOR PRIVATE USE $300

SPECIAL FOURTH-CLASS RATE
BOOK

POSTAGE AND FEES PAID
NATIONAL AERONAUTICS AND
SPACE ADMINISTRATION
451

U.S.MAIL

POSTMASTER: If Undeliverable (Section 158
Postal Manual) Do Not Return

> *"The aeronautical and space activities of the United States shall be conducted so as to contribute . . . to the expansion of human knowledge of phenomena in the atmosphere and space. The Administration shall provide for the widest practicable and appropriate dissemination of information concerning its activities and the results thereof."*
>
> —NATIONAL AERONAUTICS AND SPACE ACT OF 1958

NASA SCIENTIFIC AND TECHNICAL PUBLICATIONS

TECHNICAL REPORTS: Scientific and technical information considered important, complete, and a lasting contribution to existing knowledge.

TECHNICAL NOTES: Information less broad in scope but nevertheless of importance as a contribution to existing knowledge.

TECHNICAL MEMORANDUMS: Information receiving limited distribution because of preliminary data, security classification, or other reasons. Also includes conference proceedings with either limited or unlimited distribution.

CONTRACTOR REPORTS: Scientific and technical information generated under a NASA contract or grant and considered an important contribution to existing knowledge.

TECHNICAL TRANSLATIONS: Information published in a foreign language considered to merit NASA distribution in English.

SPECIAL PUBLICATIONS: Information derived from or of value to NASA activities. Publications include final reports of major projects, monographs, data compilations, handbooks, sourcebooks, and special bibliographies.

TECHNOLOGY UTILIZATION PUBLICATIONS: Information on technology used by NASA that may be of particular interest in commercial and other non-aerospace applications. Publications include Tech Briefs, Technology Utilization Reports and Technology Surveys.

Details on the availability of these publications may be obtained from:

SCIENTIFIC AND TECHNICAL INFORMATION OFFICE

NATIONAL AERONAUTICS AND SPACE ADMINISTRATION

Washington, D.C. 20546